8-3-2007

Electrical and Optical Characterization of Group III-V Heterostructures with Emphasis on Terahertz Devices

Aruna Bandara Weerasekara

ELECTRICAL AND OPTICAL CHARACTERIZATION OF GROUP III-V HETEROSTRUCTURES WITH EMPHASIS ON TERAHERTZ DEVICES

by

Aruna B. Weerasekara

Under the direction of Unil Perera

ABSTRACT

Electrical and optical characterizations of heterostructures and thin films based on group III-V compound semiconductors are presented. Optical properties of GaMnN thin films grown by Metalorganic Chemical Vapor Deposition (MOCVD) on GaN/Sapphire templates were investigated using IR reflection spectroscopy. Experimental reflection spectra were fitted using a non - linear fitting algorithm, and the high frequency dielectric constant (ε_∞), optical phonon frequencies of $E1_{TO}$ and $E1_{LO}$, and their oscillator strengths (S) and broadening constants (Γ) were obtained for GaMnN thin films with different Mn fraction. The high frequency dielectric constant (ε_∞) of InN thin films grown by the high pressure chemical vapor deposition (HPCVD) method was also investigated by IR reflection spectroscopy and the average was found to vary between 7.0 - 8.6. The mobility of free carriers in InN thin films was calculated using the damping constant of the plasma oscillator.

The terahertz detection capability of n-type GaAs/AlGaAs Heterojunction Interfacial Workfunction Internal Photoemission (HEIWIP) structures was demonstrated. A threshold frequency (f_c) of 3.2 THz (93 μm) with a peak responsivity of 6.5 A/W at 7.1 THz was obtained using a 0.7 μm thick 1×10^{18} cm^{-3} n - type doped GaAs emitter layer

and a 1 μm thick undoped $Al_{0.04}Ga_{0.96}As$ barrier layer. Using n - type doped GaAs emitter layers, the possibility of obtaining small workfunctions (Δ) required for terahertz detectors has been successfully demonstrated. In addition, the possibility of using GaN (GaMnN) and InN materials for terahertz detection was investigated and a possible GaN base terahertz detector design is presented.

The non - linear behavior of the Inter Pulse Time Intervals (IPTI) of neuron - like electric pulses triggered externally in a GaAs/InGaAs Multi Quantum Well (MQW) structure at low temperature ($\sim$ 10 K) was investigated. It was found that a grouping behavior of IPTIs exists at slow triggering pulse rates. Furthermore, the calculated correlation dimension reveals that the dimensionality of the system is higher than the average dimension found in most of the natural systems. Finally, an investigation of terahertz radiation effect on biological system is reported.

INDEX WORDS: Infrared, Detectors, Terahertz, Optical Phonon, Plasmon, Heterojunction, Homojunction, Free carrier absorption, Quantum efficiency, Responsivity, Dark current, Arrhenius, Absorption coefficient, Dielectric function, High frequency dielectric constant, Plasma frequency, Neuron-like pulses, Negative differential resistance, Correlation dimension, Embedding dimension, Return maps, Bifurcation, and Power spectrum.

ELECTRICAL AND OPTICAL CHARACTERIZATION OF GROUP III-V HETEROSTRUCTURES WITH EMPHASIS ON TERAHERTZ DEVICES

by

Aruna B. Weerasekara

A Dissertation Submitted in Partial Fulfillment of the Requirements for the Degree of

Doctor of Philosophy

in the College of Arts and Sciences

Georgia State University

2007

ELECTRICAL AND OPTICAL CHARACTERIZATION OF GROUP III-V HETEROSTRUCTURES WITH EMPHASIS ON TERAHERTZ DEVICES

by

Aruna B. Weerasekara

Major Professor: Dr. Unil Perera

Committee: Dr. Gennady Cymbalyuk

Dr. Nikolaus Dietz

Dr. Donald Edwards

Dr. Douglas Gies

Dr. Mark Stockman

Electronic Version Approved:

Office of Graduate Studies

College of Arts and Sciences

Georgia State University

August 2007

To my parents

Acknowledgments

First, I would like to express my sincere gratitude to my advisor for his guidance, support, patience, and constant encouragement throughout my graduate studies. This work would not have been possible without his time and energy. I have learnt innumerable lessons while working with him during past years. My sincere thanks also go to the members of my thesis committee, Nikolaus Dietz for providing research materials and having very fruitful discussions on research related work, and Gennady Cymbaluyk for providing many valuable comments, Donald Edwards, Mark Stockman, and Douglas Gies for their suggestions and comments on my research work. I would like to thank Ian Ferguson from Georgia Institute of Technology for providing research materials and facilities and H. C. Liu, NRC Canada and S. Krishna, University of New Mexico for the technical services provided during my research work and very helpful point of views. Vincent Rehder, Amanda L. Jacob, and J. Senawiratne should receive my sincere gratitude for the research materials and the support given to me during the *Terahertz irradiation on biological cells* project.

I was really lucky to have good-spirited discussions related to the research with research scientists Steven Matsik, Hu Zhigao, Dmitriy Esaev, and J. Satyabrata. My sincere gratitude goes to my colleagues, Rinzan, Gamini, Viraj, Ranga, Mustafa, and other friends for their support.

Last, but not least, my parents receive my deepest gratitude and love all the time for their invaluable dedication and sacrifice in every part of my life.

Table of Contents

List of Tables

List of Figures

Chapter 1

Introduction

Group III-V compound semiconductor materials such as Gallium Arsenide (GaAs), Indium Arsenide (InAs), Aluminum Arsenide (AlAs), Gallium Nitride (GaN), and Indium Nitride (InN) are popular semiconductors in today's semiconductor research field. These semiconductors possess a range of properties that will be suitable for the most demanding new technologies. A number of cutting - edge technologies and a vast area of applications can be realized with group III-V compound semiconductors and their alloys. Photodetectors ranging from Ultraviolet (UV) to Far Infrared (FIR) range, light emitting diodes (LEDs) with different colors, lasers, bipolar transistors, high speed switches, and electro - optic modulators are few applications to name. Therefore, the characterization of these materials is important. In this dissertation, the work based on electrical and optical characterization of group III-V heterostructures such as GaAs/AlGaAs, GaN/GaMnN, InN/GaN, and GaAs/InGaAs is presented.

Novel semiconductor materials should be explored and investigated in order to improve the opto - electronic devices including terahertz detectors. Growth and fabricat-

ing novel semiconductor structures is possible with the new growth technologies such as Molecular Beam Epitaxy (MBE) and MOCVD. Therefore, this enables scientists to study new semiconductor materials to improve and optimize existing applications and to design future applications. In Chapter 2, optical characterizations of a relatively new group III-V compound semiconductors such as Gallium Manganese Nitride (GaMnN) and InN are presented. IR reflectance spectroscopy is used as an optical tool to investigate the IR dielectric function of these materials. The IR dielectric function is an important parameter for designing opto-electronic devices such as UV, IR, and terahertz photodetectors, lasers, optical switches, etc. Furthermore, semiconductors doped with magnetic materials such as Mn, Co, and Fe will lead to Dilute Magnetic Semiconductor (DMS) materials. These DMS materials open up a new technology called "Spintronics" where the electron spin is utilized for new types of devices namely spin transistors, spin diodes, and spin storage [6]. The spintronics or spin transport electronics has emerged as a new field of interest among the science and technology community in recent years. Therefore, optical characterization of GaMnN as a DMS material is very important because it possesses room temperature ferromagnetism.

Terahertz detection using n-type doped GaAs/AlGaAs heterostructures is discussed in Chapter 3. The terahertz region, which is a relatively less explored region in the electromagnetic spectrum, can be roughly defined by frequencies between 300 GHz and 30 THz or wavelengths of 1000 - 10 μm. In recent years, attention has been drawn beyond the IR ($>$ 30 μm or $<$ 10 THz) range into terahertz range. Terahertz technology has an enormous potential in many fields such as medical diagnostics, pharmaceutical, defense, security, wireless communications, and astronomy [7]. Terahertz imaging will be useful for

bio-medical research since it can provide researchers completely new information on biological systems. Identifying tumors and healthy tissues [8] using terahertz imaging and identifying the terahertz characteristics of DNA [9] has already started. Tracking explosives, weapons, and drugs using terahertz imaging can be possible since terahertz radiation can penetrate non-metalic and non-polar materials [10]. However, the main challenge in this field is the lack of suitable terahertz sources and detectors. Detectors that are used in this region are bolometers, pyroelectric detectors, Golay cells, and heterodyne detectors. Common drawbacks of these detectors include slow response and the difficulty of integrating these detectors into focal plane arrays for imaging. Most of photon detectors based on semiconductors work in the near infrared region to the long wavelength infrared region (0.8 - 30 μm). Homojunction Interfacial Workfunction Internal Photoemission (HIWIP) and HEIWIP detectors are capable of working in the terahertz region [5, 11, 12]. During the past few years, p-type GaAs HEIWIP detectors [5, 11, 12, 13, 14] have been studied and are well understood. So far, little work has been done on n-type GaAs/AlGaAs HEIWIP detectors, so our knowledge of n-type GaAs/AlGaAs is minimal. Results on n-type GaAs/AlGaAs is presented demonstrating its terahertz detection capability. Furthermore, the possibilities of using GaN material in terahertz detection is investigated in Chapter 3. Next, terahertz emission using GaN thin films and terahertz effects on the dorsal root ganglion (DRG) are investigated in Chapter 4.

Artificial neurons have attracted scientists' attention several decades ago because of the simple structure of a single biological neuron and its powerful information processing and communication capability. Mahowald proposed the first artificial Si-neuron [15] in 1991.

Artificial neurons have a great potential in information and image processing, computation, communication, and networking. The other important area is the artificial intelligence, where systems are capable of self - learning and are self - adaptive. At present, transistors, integrated circuits, and processors with digital computing methods are used in information processing and computation. It is believed that artificial neural networks with asynchronous parallel processing capability [16, 17] can process information much faster than the present technology. Furthermore, an artificial retina based on artificial neurons that can detect IR light would be interesting. The limitation of Si-neurons is the physical size and the power requirements which are not favorable for massive neural networks. The alternatives are single element pulsing devices such as the Si $p-i-n$ junction diode [17, 18, 19]. The advantages of this type of a fundamental device are low power dissipation and the micro scale physical size. Therefore, thousands of these devices can be integrated to make arrays for powerful applications. In Chapter 5, a nonlinear analysis of neuron - like electrical pulses in GaAs/InGaAs MQW, which is another group III-V heterostructure, is presented. The Inter Pulse Time Intervals (IPTI) of electrical pulses were recorded and analyzed using nonlinear techniques. Discussions on first return maps, and the correlation dimensions are presented.

Chapter 2

Material Characterization by Infrared Reflectance Spectroscopy

2.1 Introduction

Semiconductor material characterization is important for the applications of semiconductor materials. Optical techniques are useful and popular tools among the semiconductor material characterization techniques as they are non-destructive. Commonly used optical characterization methods include reflectance, absorption, and transmission spectroscopies of IR and UV, Raman spectroscopy, and Photoluminescence (PL) spectroscopy. These techniques probe important electric and optical properties of semiconductor materials without damaging the materials. IR reflectance spectroscopy is mainly used to investigate band gaps, the IR Dielectric function, the phonon and plasmon properties, carrier concentrations, carrier mobility, layer thicknesses, and interface behavior. The IR reflectance spectroscopy is useful to investigate the dielectric functions of materials in the IR region,where

optical phonon frequencies of semiconductors are located.

2.1.1 IR dielectric function in semiconductors

Light propagation in a medium was first described by Henrik Antoon Lorentz in 1878 treating atoms and molecules as dipoles [20]. The same treatment can be applied to describe the interaction between electromagnetic radiation and the atoms in a semiconductor lattice. A semiconductor crystal consists of a three dimensional array of atoms, which are connected. The lattice vibrational frequencies can be found from solutions to the equations of motion for atoms.

For an example, a linear crystal which consists of two atoms per site can be considered [21] as shown in Fig. 2.1 (a). The equation of motions for atoms M_1 and M_2

$$M_1 \frac{d^2 x_s}{dt^2} = C(y_s + y_{s-1} - 2x_s) \tag{2.1}$$

$$M_2 \frac{d^2 y_s}{dt^2} = C(x_s + x_{s-1} - 2y_s), \tag{2.2}$$

where M_1 and M_2 are the masses of atoms, C is the force constant and is assumed to be identical between nearest neighbors. x and y are the displacements of M_1 and M_2. The solutions for Eq. 2.1 and Eq. 2.2 will have the following form with different amplitudes

$$x_s = x_0 \cdot Exp(isKa - iwt) \tag{2.3}$$

$$y_s = y_0 \cdot Exp(isKa - iwt), \tag{2.4}$$

where K is the wavevector, ω is frequency, and t is time. By combining Eq. 2.1, Eq. 2.2 Eq. 2.3, and Eq. 2.4 and considering the limits of $Ka << 1$ and $Ka = \pm\pi$, we can obtain

$$\omega^2 \cong 2C(\frac{1}{M_1} + \frac{1}{M_2}) \tag{2.5}$$

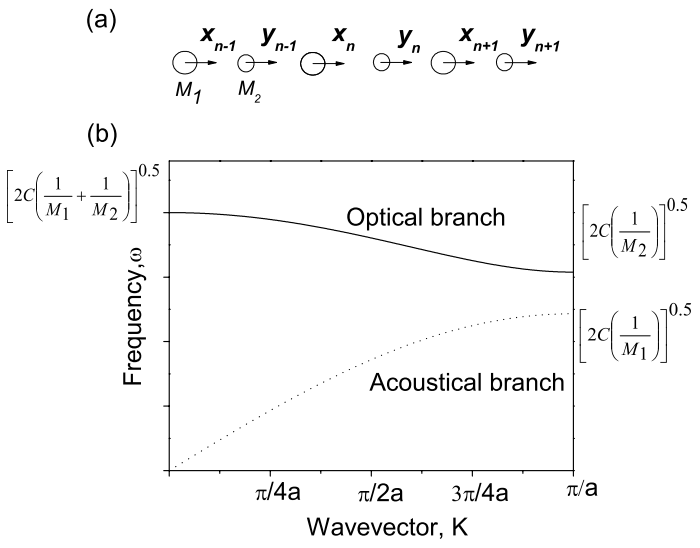

Figure 2.1: (a) shows diatomic linear crystal. Atomic masses are M_1 and M_2 ($M_1 > M_2$). x and y are the displacements of atoms. (b) Behavior of optical and acoustical branches for a diatomic crystal.

$$\omega^2 \cong \frac{CK^2a^2}{2(M_1 + M_2)} \tag{2.6}$$

The roots of Eq. 2.5 are called the optical branch or mode while the roots of Eq. 2.6 are called the acoustical branch or mode. The behavior of the two branches with wavevector, K is shown in Fig. 2.1 (b). In the optical branch, atoms of opposite charge oscillate in opposite directions producing a dipole moment, which can interact with light. In the acoustic mode, all atoms vibrate in the same direction resulting in the center of mass of atoms displacement. At smaller K values, acoustical branch behaves linearly with K.

The displacement vector (D) inside materials can be given as follows,

$$D(\omega) = \varepsilon_0 E + P(\omega), \tag{2.7}$$

where ε_0 is the permittivity in free space, E is applied electric field and P is polarization. Furthermore, the displacement vector can be written as,

$$D(\omega) = \varepsilon(\omega)\varepsilon_0 E, \tag{2.8}$$

where $\varepsilon(\omega)$ is the dielectric function of the material and is a function of the incident light frequency (ω). The polarization P consists of two parts: a non resonant background part, $P_b = \varepsilon_0 \chi E$ and a resonant P_{res} part given by Eq. 2.9, where χ is susceptibility.

In an oppositely charged linear diatomic chain model, the resonant part of polarization (P_{res}) under an electric field of $E = E_0 e^{-i\omega t}$ is given by Eq. 2.9,

$$P_{res}(\omega) \propto \frac{E_0 e^{-i\omega t}}{\omega_{TO}^2 - \omega^2 - i\Gamma\omega}, \tag{2.9}$$

where Γ is called the oscillator broadening constant.

By combining Eq. 2.7 - Eq. 2.9, the lattice dielectric response function, $\varepsilon(\omega)$ is given as follows

$$\varepsilon(\omega) = \varepsilon_\infty + \frac{S\omega_{TO}^2}{\omega_{TO}^2 - \omega^2 - i\Gamma\omega}, \tag{2.10}$$

where $\varepsilon_\infty = 1 + \chi$ is the high frequency dielectric constant, S is the oscillator strength and is proportional to the number of atoms in a cubic centimeter.

Furthermore, Eq. 2.10 can be extended for multi - phonon materials as follows

$$\varepsilon(\omega) = \varepsilon_\infty + \sum_{j=1}^{N} \frac{S_j\omega_{TOj}^2}{\omega_{TOj}^2 - \omega^2 - i\Gamma_j\omega}, \tag{2.11}$$

where N is the total number of optical phonons, ω_{TOj} is the frequency of the j^{th} optical phonon. S_j and Γ_j are the oscillator strength and broadening constant of the j^{th} optical phonon.

2.1.2 Free carrier contribution to the dielectric function

When free carriers are present, the complete IR dielectric function [22] is given by Eq. 2.12

$$\varepsilon(\omega) = \varepsilon_{lat}(\omega) + \frac{i\sigma(\omega)}{\varepsilon_0\omega}, \tag{2.12}$$

where ε_{lat} is the contribution from the lattice. $\sigma(\omega)$ is a.c. conductivity with $\sigma(\omega) = \frac{\omega_p^2\tau}{(1-i\omega\tau)}$, the plasmon frequency is $\omega_p = \frac{ne^2}{\varepsilon_0 m^*}$ and τ is the scattering time. The complete dielectric function can be written as follows

$$\varepsilon(\omega) = \varepsilon_\infty[1 - \frac{\omega_p^2}{\omega(\omega + i\gamma_p)}] + \sum_{j=1}^{N} \frac{S_j\omega_{TOj}^2}{\omega_{TOj}^2 - \omega^2 - i\Gamma_j\omega}, \tag{2.13}$$

where γ_p is the damping constant.

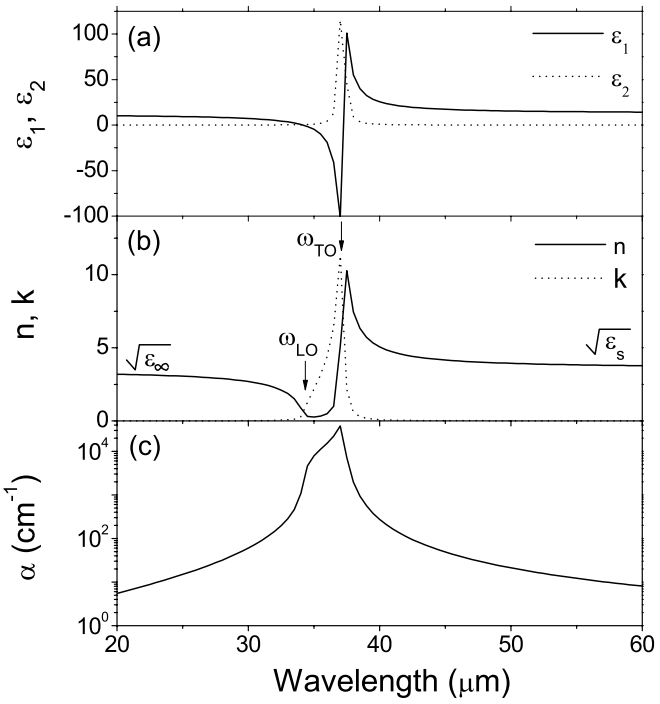

Figure 2.2: (a) shows the real (ε_1) part and the imaginary part (ε_2) of GaAs dielectric function. The real part of the dielectric function becomes negative at the phonon frequency. (b) The ordinary refractive index and the extinction coefficient of GaAs. The ordinary refractive index becomes quite small between ω_{TO} and ω_{LO}. (c) The calculated absorption coefficient (α) is shown and peaks at the phonon frequency.

2.1.3 Refractive index and absorption coefficient

The complex refractive index (n^*) and the absorption coefficient (α) can be calculated once the dielectric function of the material is determined. The refractive index (n^*) consists of a real part (n) and an imaginary part (k). In some cases, n is called the ordinary refractive index and k is called the extinction coefficient (or attenuation index) which determines the light absorption inside the material. The complex refractive index (n^*) is given by $n^* = \sqrt{\varepsilon}$. And, n and k can be calculated as follows,

$$n = [\frac{(\varepsilon_1^2 + \varepsilon_2^2)^{1/2} + \varepsilon_1}{2}]^{1/2}, \tag{2.14}$$

$$k = [\frac{(\varepsilon_1^2 + \varepsilon_2^2)^{1/2} - \varepsilon_1}{2}]^{1/2}, \tag{2.15}$$

where ε_1 and ε_2 are the real part and the imaginary part of the dielectric function. The absorption coefficient (α) is given by Eq. 2.16

$$\alpha = \frac{4\pi k}{\lambda}. \tag{2.16}$$

GaAs is a diatomic material that can be taken as an example to discuss a few important aspects of the IR dielectric function. The calculated real part and the imaginary part of the GaAs IR dielectric function is shown in Fig. 2.2 (a). The ε_∞, ω_{TO}, S, and Γ were taken as 10.9, 268.2 cm^{-1}, 2.0, and 2.5 cm^{-1}. The real part of the dielectric function becomes negative around the ω_{TO} where GaAs shows metal like behavior. Figure 2.2 (b) shows the ordinary refractive index (n) and extinction coefficient (k) behavior in the phonon region. The region between ω_{TO} and ω_{LO} is called restrahlen band where the ordinary refractive index (n) becomes very small while the real part of the dielectric function becomes negative. The absorption coefficient of GaAs (α) is shown in Fig. 2.2 (c).

2.1.4 Modeling IR reflectance in multilayer semiconductor structure

Light propagation in a multilayer thin film structure can be modeled using the Transfer Matrix method[23, 24]. Figure 2.3 (b) shows the normal incident light propagation through an isotropic and homogeneous multilayer structure. In a given layer, light propagates in both $+z$ and $-z$ direction due to the multiple reflections, and E^+ and E^- indicate the electric fields of $+z$ and $-z$ direction traveling light. On the interface between i^{th} and $(i+1)^{th}$ layers [see Fig. 2.3 (a)], the electric fields and magnetic fields satisfy the following conditions

$$E_i^+ + E_i^- = E_{i+1}^+ + E_{i+1}^- \tag{2.17}$$

$$\frac{1}{\mu_i}(H_i^+ - H_i^-) = \frac{1}{\mu_{i+1}}(H_{i+1}^+ - H_{i+1}^-) \tag{2.18}$$

Since $\sqrt{\varepsilon\mu}E = H$ and using Eq. 2.17 and Eq. 2.18, the electric fields of propagating light inside the $(i+1)^{th}$ layer can be expressed in terms of the electric fields in the i^{th} layer. The $+z$ direction electric field in $(i+1)^{th}$ layer is

$$E_{i+1}^+(0) = \frac{1}{2}[(1+\frac{n_i}{n_{i+1}})E_i^+(t_i) + (1-\frac{n_i}{n_{i+1}})E_i^-(t_i)], \tag{2.19}$$

The $-z$ direction electric field in $(i+1)^{th}$ layer is

$$E_{i+1}^-(0) = \frac{1}{2}[(1-\frac{n_i}{n_{i-1}})E_i^+(t_i) + (1+\frac{n_i}{n_{i+1}})E_i^-(t_i)], \tag{2.20}$$

where n_i and t_i are the complex refractive index and the thickness of the i^{th} layer. Now, Eq. 2.19 and Eq. 2.20 can be expressed in a matrix format [Eq. 2.21] and T is the Transfer Matrix for light propagation from the i^{th} layer into the $(i+1)^{th}$ layer,

$$\begin{pmatrix} E_{i+1}^+(0) \\ \\ E_{i+1}^-(0) \end{pmatrix} = T_{i,i+1} \begin{pmatrix} E_i^+(t_i) \\ \\ E_i^-(t_i) \end{pmatrix}, \tag{2.21}$$

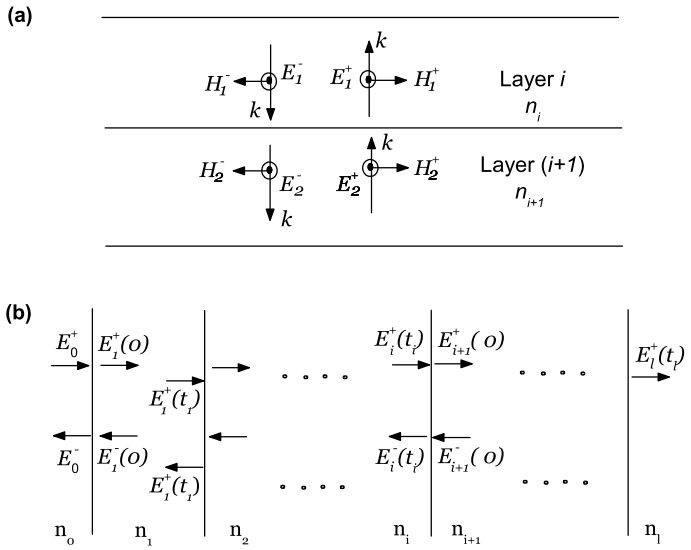

Figure 2.3: (a) Normal incident light propagation from one isotropic medium (i^{th} layer) to another isotropic medium ($(i+1)^{th}$ layer) is illustrated. The directions of the electric fields (E), magnetic fields (H), and wavevector (k) are shown. In a given layer, the forward and backward traveling light components exist due to the multi - reflections. (b) Propagating electric fields inside a multilayer stack with l layers are shown. Arrows show only the light propagation directions. n_1, n_2,... and t_1, t_2,... are the complex refractive indices and the thicknesses of each layer. Electric field of the incident light and reflected light are E_0^+ and E_0^-. The electric field transmitted by the multilayer stack is $E_l^+(t_l)$.

$$\text{where, } T_{i,i+1} = \begin{pmatrix} 1+\frac{n_i}{n_{i+1}} & 1-\frac{n_i}{n_{i+1}} \\ 1-\frac{n_i}{n_{i+1}} & 1+\frac{n_i}{n_{i+1}} \end{pmatrix}$$

The electric fields propagating inside the i^{th} layer are given by Eq. 2.22

$$\begin{pmatrix} E_i^+(x_i) \\ E_i^-(x_i) \end{pmatrix} = D_i \begin{pmatrix} E_i^+(0) \\ E_i^-(0) \end{pmatrix}, \tag{2.22}$$

where, $D_i = \begin{pmatrix} e^{ikn_ix_i} & 0 \\ 0 & e^{-ikn_ix_i} \end{pmatrix}$ and is the Propagation matrix. Light transmission from one layer to another layer and light propagation inside each layer can be expressed by separate Transfer matrices and separate Propagation matrices defined for each layer. Therefore, the electric fields in the j^{th} layer can be written in terms of the initial electric fields E_0^+ and E_0^- as

$$\begin{pmatrix} E_j^+(0) \\ E_j^-(0) \end{pmatrix} = \begin{pmatrix} a & b \\ c & d \end{pmatrix} \begin{pmatrix} E_0^+ \\ E_0^- \end{pmatrix}, \tag{2.23}$$

$$\text{where } \begin{pmatrix} a & b \\ c & d \end{pmatrix} = \begin{pmatrix} 1+\frac{n_{j-1}}{n_j} & 1-\frac{n_{j-1}}{n_j} \\ 1-\frac{n_{j-1}}{n_j} & 1+\frac{n_{j-1}}{n_j} \end{pmatrix} \begin{pmatrix} e^{\phi_{j-1}} & 0 \\ 0 & e^{-\phi_{j-1}} \end{pmatrix} ...$$

$$... \begin{pmatrix} e^{\phi_1} & 0 \\ 0 & e^{-\phi_1} \end{pmatrix} \begin{pmatrix} 1+\frac{n_0}{n_1} & 1-\frac{n_0}{n_1} \\ 1-\frac{n_0}{n_1} & 1+\frac{n_0}{n_1} \end{pmatrix}$$

and $\phi_i = ikn_it_i$ is the phase angle.

Finally, the incident ($E_i = E_0^+$), reflected ($E_r = E_0^-$), and transmitted (E_t) electric

field components for the whole multilayer structure can be formulated as given in Eq.2.24.

$$\begin{pmatrix} E_t \\ 0 \end{pmatrix} = M \begin{pmatrix} E_i \\ E_r \end{pmatrix}, \tag{2.24}$$

where M is the product of all Transfer and Propagation matrix multiplication from the 1^{st} layer through the last layer l^{th} and is given by $M = \begin{pmatrix} A & B \\ C & D \end{pmatrix} = T_l \cdot D_{l-1} ... D_i \cdot T_i ... D_1 \cdot T_1$

Now, reflectance (r) and transmitance (t) can be written as in Eq. 2.25 and Eq. 2.26,

$$r = \frac{E_r}{E_i} = \frac{-C}{D} \tag{2.25}$$

$$t = \frac{E_r}{E_i} = A + \frac{BC}{D} \tag{2.26}$$

Therefore, reflection (R) and transmission (T) can be calculated as follows,

$$R = r^* r, \tag{2.27}$$

$$T = t^* t \frac{n_l \mu_0}{n_0 \mu_l}, \tag{2.28}$$

where n_0, n_l, μ_0, and μ_l are the complex refractive indices and the permeabilities of the media that incident light starts in and the transmitted light exits into. If the starting and the final media are the same, then $T = t^* t$. Finally, the total light absorption (A) inside the whole multilayer stack can be obtained as

$$A = 1 - (R + T) \tag{2.29}$$

2.1.5 IR reflection measurements and model fitting

Infrared reflection measurements were carried out using the Perkin Elmer System 2000 Fourier transform infrared spectrometer along with a Graseby reflection accessories

setup. A Mercury Cadmium Telluride (MCT) detector was used for the short wavelength (5-20 μm) range and a Triglycine Sulfate (TGS) based pyroelectric detector was used for the long wavelength (> 50 μm) range. A Gold or an Aluminum mirror was used to collect background spectra. Thereafter, raw reflection spectra of thin film structures were divided by the background spectrum to obtain the reflection spectra. A nonlinear fitting algorithm, Levenberg-Marquardt [25] (see Appendix A), was used to obtain the best fit parameters from the experimental IR reflection spectra.

2.2 IR dielectric function of $Ga_{1-x}Mn_xN$

Spintronics or spin transport electronics has emerged as a new field of interest among the science and technology community in recent years. The idea of utilizing the spin of electrons may open up a new era of technology based on spintronics devices [26] such as spin diodes, spin transistors, spin based data storage, etc. Therefore, efforts in fabricating and investigating appropriate new semiconductor materials have been made in recent years [27, 28]. Diluted magnetic semiconductors (DMS) based on III-V group semiconductors such as GaMnN, GaMnAs, and CdMnTe have attracted considerable interest as the materials that can support the transport and storage of spin, and that can be integrated into existing electronic and optoelectronic devices. Among these DMS materials, manganese (Mn)-doped GaN ($Ga_{1-x}Mn_xN$) attracted strong attention due to the theoretical prediction of room-temperature ferromagnetism in the nitride using the Zener model [29, 30]. Experimental studies on the fundamental optical properties of GaMnN are still rare, however, there have been numerous reports of successful preparation of $Ga_{1-x}Mn_xN$ films and their magnetic

properties [3, 31, 32]. The behavior of E_1 phonon modes (perpendicular to the c-axis) of GaMnN, which are subject to local lattice vibrations [33, 34], is particularly interesting because of the important effects from the Mn incorporation with the GaN matrix. The lattice vibrations and dielectric functions of the $Ga_{1-x}Mn_xN$ films are important when designing spintronic and opto-electronic devices based on $Ga_{1-x}Mn_xN$ material. Descriptions of the infrared optical properties of $Ga_{1-x}Mn_xN$ are still rare in the literature. In this section, the lattice vibrational properties of $Ga_{1-x}Mn_xN$ epitaxial films deposited on sapphire substrates are investigated using IR reflectance spectra. Effects of Mn composition on the E_1 phonon modes and the dielectric functions are discussed in detail.

2.2.1 Introduction to the host GaN matrix

GaN is the host lattice matrix for Mn atoms in $Ga_{1-x}Mn_xN$. The lattice properties of $Ga_{1-x}Mn_xN$ are closely related to GaN lattice properties. Therefore, a brief introduction to GaN will be appropriate. GaN can be found in two form of lattice structures: (i) Wurtzite (Hexagonal) and (ii) Zinc-Blend (Cubic). The wurtzite GaN is widely available because it is more stable. The wurtzite structure shown in Fig. 2.4 (a) has two Ga-N pairs in the primitive cell and the stacking order is ABAB...ABAB. The GaN band gap energy (E_g), high frequency dielectric constant (ε_∞), the static dielectric constant (ε_0) are 3.39 eV, 5.35, and 8.9 - 9.5, respectively [2]. Eight phonon modes at the Γ point exist in the wurtzite structure according to group theory [1, 2] and those are $2A_1+2E_1+2B_1+2E_2$. One of A_1 modes and one of B_1 modes are acoustic phonons while others are optical phonons namely A_1, E_1, B_1-high, B_1-low, E_2-high,and E_2-low. Atomic vibration in E_1 and E_2 modes are perpendicular to c-axis while A_1 and B_1 modes are along the c-axis as shown in Fig. 2.4

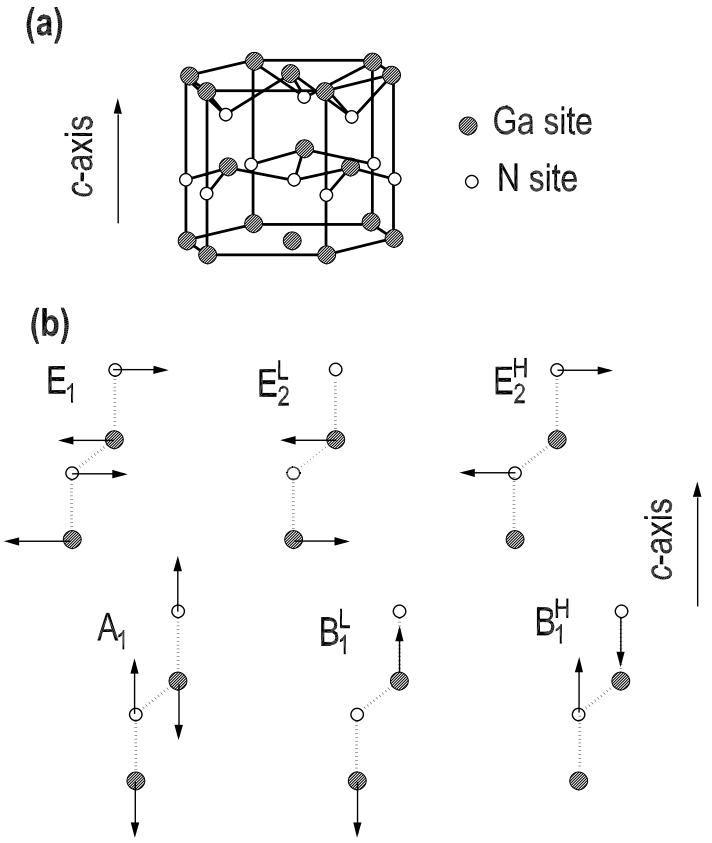

Figure 2.4: (a) GaN wurtzite structure. Dashed circles are Ga sites and open circle are N sites. (b) Optical phonon vibration directions. The vibration directions of E_1 and E_2 are perpendicular to c-axis while A_1 and B_1 are parallel to c-axis. Indices H and L are high and low, respectively (adapted from Ref. [2]).

Table 2.1: GaN optical modes and their calculated and experimental frequencies and those that are active and inactive in Raman and IR [1, 2].

Mode	Active in	Phonon frequency (cm^{-1})	
		Experiment	Theory
$E_2 - low$	$Raman$	144	146
$A_1(TO)$	$Raman, IR$	533	534
$E_1(TO)$	$Raman, IR$	561	556
$E_2 - high$	$Raman$	569	560
$A_1(LO)$	$Raman, IR$	735	
$E_1(LO)$	$Raman, IR$	743	
$B_1 - low$	$Silent$		335
$B_1 - high$	$Silent$		697

(b). However, at the Γ point, each phonon A_1 and E_1 splits into transverse and longitudinal modes giving $A_1(TO)$, $A_1(LO)$, $E_1(TO)$, and $E_1(LO)$. $B_1 - high$ and $B_1 - low$ are not active (silent) in modes in IR and Raman. The properties of all eight optical phonons are listed in Table 2.1. In GaMnN, the Mn^{2+} ion replaces the Ga atom and acts as an acceptor.

2.2.2 $Ga_{1-x}Mn_xN$ samples and experimental technique

Hexagonal $Ga_{1-x}Mn_xN$ expitaxial films in a composition range (x) from 0.0% to 1.5% were grown on *c*-plane MOCVD [3]. Initially, *p*- doped (2×10^{16} cm^{-3} GaN epilayers (sample A) were used as templates in order to obtain the mirror-like surfaces. Then $Ga_{1-x}Mn_xN$ epitaxial films were deposited on the GaN templates. The epilayers were deposited using a customized MOCVD reactor with a vertical injection system. Ammonia, tri-methyl gallium, and bis-cyclopenadienyl manganese (Cp_2Mn) were used as the nitrogen, gallium, and manganese sources, respectively, for the growth of $Ga_{1-x}Mn_xN$ films. Different concentrations of the incorporated Mn were achieved through the molar flow of Mn going into the reactor. The growth temperature was maintained in a range from 900 to 1050 ^{0}C. More details of the growth process can be found in Ref. [3]. X-ray diffraction (XRD) spectroscopy revealed single phase structure suggesting that the $Ga_{1-x}Mn_xN$ films were of good quality. The XRD spectrum for $x = 0.3\%$ Mn sample is shown in Fig. 2.5. Near-normal IR reflectance spectra ($\sim 8^\circ$) were measured at room temperature (RT) over the frequency range of $200 - 2000$ cm^{-1} ($5 - 50$ μm) using a FTIR spectrometer as described before in Section 2.1.5. The *s*-polarized incident light was used in order to predominantly identify the E_1 phonon behavior in this work. The isotropic treatments are reasonable for the phonon modes, which are perpendicular to the *c*-axis under near-normal incident con-

figurations using the *s*-polarized light [33]. Only the E_1 phonons are IR-active in the present measurements based on the selection rule. For polar semiconductor materials, IR dielectric functions of the $Ga_{1-x}Mn_xN$ films can be written as follows

$$\varepsilon(\omega) = \varepsilon_\infty(1 + \frac{\omega_{LO}^2 - \omega_{TO}^2}{\omega_{TO}^2 - \omega^2 - i\omega\Gamma}). \tag{2.30}$$

It should be noted that the free carrier effects are neglected since the $Ga_{1-x}Mn_xN$ epilayers are nominally undoped. High free carrier concentration was ruled out by Raman studies, providing an upper limit of 10^{16} cm^{-3} for doping, which was the detection limit of the applied Hall-effect measurements [35].

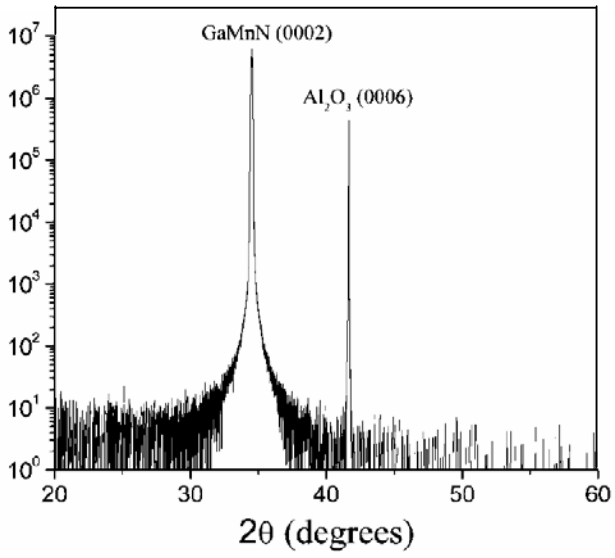

Figure 2.5: $2\theta - \omega$ XRD difraction spectrum for $Ga_{0.988}Mn_{0.012}N$. There is no second phase formation suggesting good crystal quality of GaMnN epilayers (taken from ref.[3]).

Table 2.2: The Sapphire optical phonon parameters used in the Factorized dielectric model. The high frequency dielectric constant (ε_∞) of sapphire was kept at 3.09 . The thickness of the substrate is 500 μm. Errors are given within brackets.

Optical Phonon	ω_{LO}	γ_{LO}	ω_{TO}	γ_{TO}
	cm^{-1}	cm^{-1}	cm^{-1}	cm^{-1}
E_1	387.6(0.1)	3.4(0.9)	384.6(0.06)	4.3(0.4)
E_2	482.0(0.8)	2.9(0.3)	439.4(1.5)	0.9(0.5)
E_3	629.3(1.7)	6.9(0.4)	567.0(2.5)	8.6(1.8)
E_4	912.5(2.8)	18.1(2.8)	633.2(1.8)	6.7(0.4)

Due to the reststrahlen regions of sapphire overlapping with those of $Ga_{1-x}Mn_xN$, and the interference effects in the transparent region, the experimental reflection spectra were fitted using the model to extract the phonon modes and the high frequency dielectric constant of the $Ga_{1-x}Mn_xN$ epilayers. First of all, the reflection spectrum of the 500 μm thick bulk sapphire was fitted using a two phase model (Air/Sapphire) as described in section 2.1.5. The dielectric function in the factorized form [36] was used to model the sapphire substrate dielectric function, and the fitted parameters for the sapphire substrate are given in Table 2.2. The listed parameters in Table 2.2 agree well with published data [37]. Thereafter, the sample A reflection spectrum was fitted using a three phase model (Air/GaN/Sapphire) described in section 2.1.5, and the best fit parameters were obtained for the GaN epilayer. Thereafter, the fitting parameters obtained were kept constant in all subsequent four-phase model (air/$Ga_{1-x}Mn_xN$/GaN/sapphire) calculations for other $Ga_{1-x}Mn_xN$ films.

2.2.3 Results and Discussion

The experimental reflectance spectra for the $Ga_{1-x}Mn_xN$ epilayers with the composition x varying from 0.0% to 1.5% are shown in Fig. 2.6 (dotted lines) and the best fit parameters obtained for $Ga_{1-x}Mn_xN$ epilayers are given in Table 2.3. The broadening edge at 910 cm^{-1} is assigned to the reststrahlen band of the sapphire, which is close to the E_4(LO) phonon frequency of 909 cm^{-1}. The reflectance strength is weak (about 20%) for the epilayers below the frequency of 300 cm^{-1}, indicating further that the contributions from the free carriers need not be considered. An interference effect beyond 1000 cm^{-1} (< 10 μm) is clearly observed for all films indicating that the epilayers are transparent in this region. For samples A and B, a sapphire peak [37] is seen around 450 cm^{-1}. This

Table 2.3: The best fit parameter values obtained from the experimental IR reflection spectra of $Ga_{1-x}Mn_xN$ samples. The 90% confidence limits of the fitting parameters are given in brackets.

Samples	x (%)	thickness (nm)	ε_∞	ω_{LO} (cm^{-1})	ω_{TO} (cm^{-1})	Γ (cm^{-1})
A	0.0	2102 (8.2)	5.08 (0.03)	746 (1.7)	558.4 (0.6)	5.0 (0.2)
B	0.3	366 (5.9)	5.18 (0.06)	747 (3.4)	560.0 (0.6)	7.0 (0.6)
C	0.8	1116 (6.5)	5.16 (0.04)	746 (1.8)	562.2 (0.8)	6.9 (0.3)
D	1.2	1051 (7.5)	5.25 (0.05)	741 (2.2)	562.5 (0.9)	7.0 (0.4)
E	1.5	1718 (8.8)	5.22 (0.04)	745 (1.3)	563.7 (0.8)	9.6 (0.3)

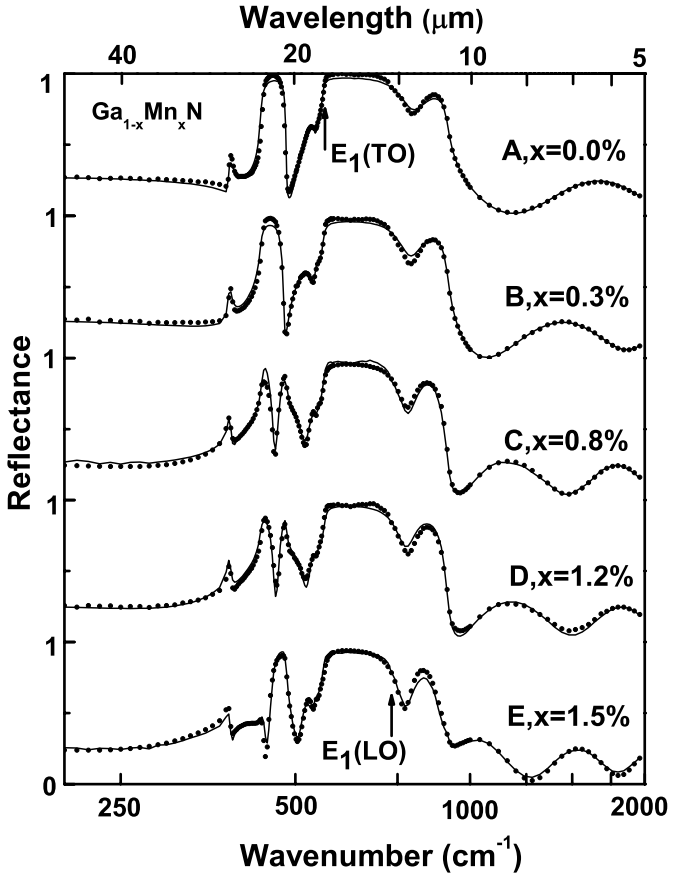

Figure 2.6: Experimental infrared reflectance spectra (dotted lines) of the $Ga_{1-x}Mn_xN$ films on sapphire and their best fit results (solid lines). Each spectrum is successively shifted by 1.0 in the vertical direction. The horizontal coordinate is in logarithmic units to enlarge the reststrahlen region.

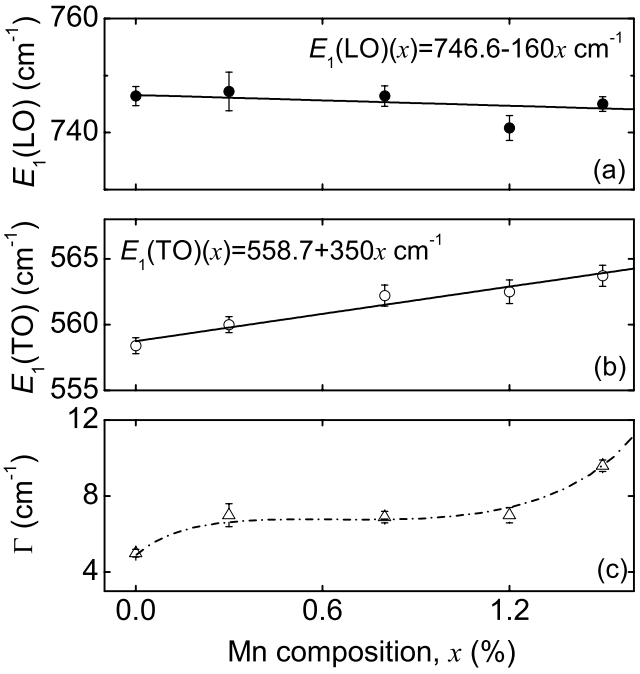

Figure 2.7: Mn composition dependence of (a) the E_1(LO) phonon frequency, (b) the E_1(TO) phonon frequency and (c) the broadening value of the E_1(TO) phonon for the $Ga_{1-x}Mn_xN$ films. The solid lines in (a) and (b) represent the linear fitting results. The dashed line in (c) is only used to guide the eye.

peak splits into two peaks for the epilayers with higher Mn compositions. For sample E, the second peak is much stronger, which maybe due to the local vibrations from Mn alloy. There is also a dip at about 785 cm^{-1} in the reflectance spectra of the epilayers. This is due to an interference within the sub-wavelength thickness of the $Ga_{1-x}Mn_xN$ epilayers on the highly reflecting sapphire, and the exact position varies with the different thicknesses [33]. The following simulations confirm this for the $Ga_{1-x}Mn_xN$ epilayers, and give their respective thickness values. The calculated reflectance spectra are also shown in Fig. 2.6 (solid lines). A good agreement between the calculated and experimental data is obtained in the entire frequency region. However, small deviations can be observed that are due to the local vibrations from incorporated Mn atoms, which are not considered in Eq. 2.30. A more rigorous dielectric function model based on the Random Phase Approximation (RPA) has been recently presented by Aguado *et al.* [38]. However, the single oscillator model used in the present work still provides good insight on the E_1 phonon modes observed. The best-fit parameters of the Lorentz oscillator model together with the fitting errors are listed in Table 2.3. The thickness of the sample B with $x = 0.3\%$ (366.5 ± 5.9 nm) is the smallest compared to the other epilayers with thickness between ~ 1 and ~ 2 μm. The high-frequency dielectric constants ε_∞ of the $Ga_{1-x}Mn_xN$ films vary from 5.08 ± 0.03 to 5.25 ± 0.05, which are slightly below the reported value of 5.35 for GaN [34]. A composition dependency of the E_1(LO) phonon frequency which may be expressed in the form $(746.6 - 160x)$ cm^{-1} with the Mn composition x is shown in Fig. 2.7(a). It shows that the E_1(LO) phonon slightly decreases with increasing Mn composition. However, the E_1(TO) phonon frequency increases with Mn composition as shown in Fig. 2.7 (b).

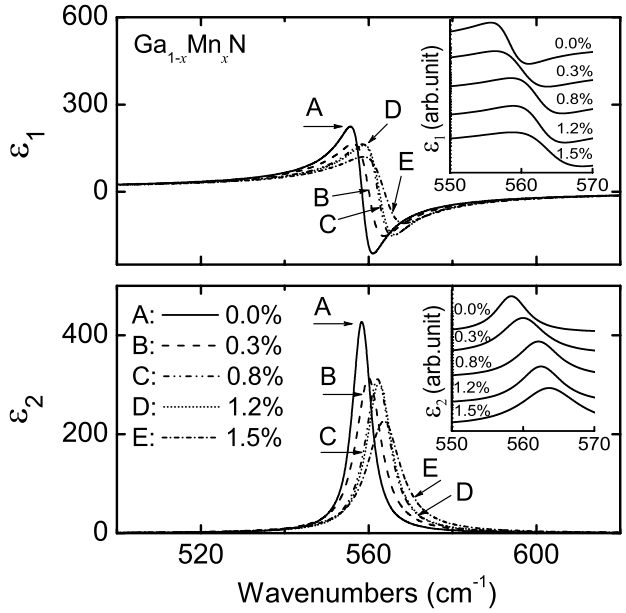

Figure 2.8: The infrared dielectric functions of the $Ga_{1-x}Mn_xN$ films with different Mn compositions. ε_1 and ε_2 are the real and imaginary parts of the dielectric functions, respectively. The inset is an enlargement of the E_1(TO) phonon mode region.

The results show a linear dependency of the E_1(TO) phonon frequency on the Mn composition range from 0.0% to 1.5%: $(558.7 + 350x)$ cm^{-1}. Limmer *et al.* [28] reported a similar linear dependency (a minute decreasing trend) for $Ga_{1-x}Mn_xAs$ films with Mn compositions from 0.0% to 2.8%. The linear dependency maybe due to the local variation of the lattice constants for the $Ga_{1-x}Mn_xN$ films with different Mn compositions. Thaler *et al.* [30] observed a linear decrease in the lattice constant as the Mn composition increases from 0.0% to 3.0%. A similar structural change might be induced in the $Ga_{1-x}Mn_xN$ layers. IR reflectometry is better than Raman spectrometry for the study of the E_1 phonon modes because of the close proximity of the E_2 (high) phonon mode at 569 cm^{-1} and its strong intensity [39] limits the resolution in Raman studies. The broadening values of the E_1(TO) phonon show a slightly increasing trend (from 5.0 to 9.6 cm^{-1}) with the composition (Fig. 2.7 (c)). Note that the values are nearly the same for the films with $x = 0.3$, 0.8 and 1.2. It indicates that the crystalline quality does not significantly change with the Mn concentrations studied so far. The Mn alloy reduces the bonding forces in the material and weakens the translational symmetry of the crystal lattice, which leads to a slight broadening of the E_1(TO) phonon line [28].

IR dielectric functions for the E_1 phonon modes of the $Ga_{1-x}Mn_xN$ epitaxial films with the Mn composition x in the frequency region of $500-620$ cm^{-1} $(16-20\ \mu$m) is shown in Fig. 2.8. In the transparent region (below 500 cm^{-1}), the real part ε_1 of the dielectric function is 4.8 indicating the refractive index is about 2.2, which is close to the reported values $(2.2-2.3)$ obtained from the transmission spectra of GaN [40]. The peak position of the imaginary part (correspondingly to the E_1(TO) phonon) shows a blue-shift trend with

increasing Mn composition. Moreover, the line shapes of the $Ga_{1-x}Mn_xN$ films are obviously different from that of the GaN film in the reststrahlen region (see the inset of Fig. 2.8) and become more broadened. As discussed above, the peak value of the GaN film is larger due to a smaller broadening value (5.0 cm^{-1}). From this viewpoint, it can be also found that the effects from Mn alloy are significant for the properties of the E_1 phonon modes. In addition, the dielectric functions are the basic parameters for FIR detector designs. The total absorption of detectors based on the $Ga_{1-x}Mn_xN$ materials can be calculated using the obtained dielectric functions. At the wavelength of 20 μm, the absorption coefficient of undoped $Ga_{1-x}Mn_xN$ films is about 10^3 cm^{-1}, which is much larger than the value (500 cm^{-1}) of the GaN film as shown in Fig. 2.9. It indicates that the introduction of Mn increases the absorption coefficient for the $Ga_{1-x}Mn_xN$ films in the FIR region. The results keep the promise for the designs of novel GaMnN/GaN FIR detectors.

In conclusion, the infrared optical properties of hexagonal $Ga_{1-x}Mn_xN$ ($0.0\% \leq x \leq 1.5\%$) films deposited on sapphire substrates have been investigated using IR reflectance spectroscopy. The E_1(LO) phonon frequency decreases and the E_1(TO) phonon frequency linearly increases with the Mn composition. The dielectric functions of the $Ga_{1-x}Mn_xN$ films are slightly below those in GaN film in the reststrahlen region indicating a weakening of the local structural bonding in the wurtzite lattice due to the introduction of Mn .

2.3 Optical properties of Si-doped $Ga_{1-x}Mn_xN$

In this study, the optical properties of Si-doped (n-type) $Ga_{1-x}Mn_xN$ are investigated by using IR reflection spectroscopy. The focus here is on the behavior of high

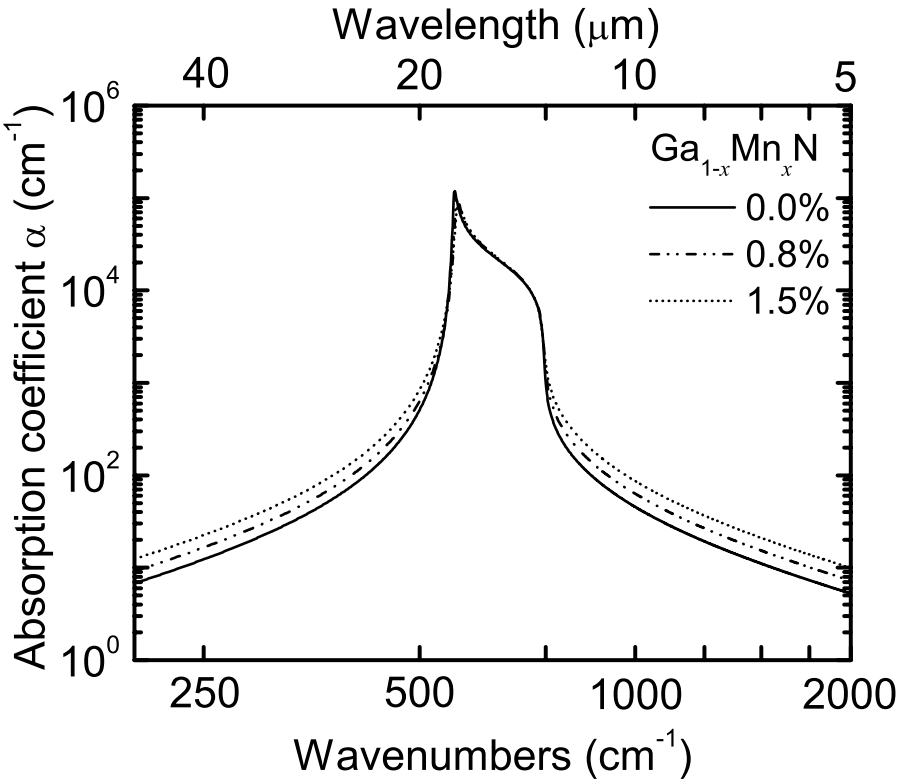

Figure 2.9: The infrared absorption coefficients of the $Ga_{1-x}Mn_xN$ films with Mn composition 0.0 (solid line), 0.8% (dash-dotted line) and 1.5% (dotted line) from the dielectric functions.

frequency dielectric constant ϵ_∞, optical phonon modes (E_1(TO), E_1(LO)) in n-type doped $Ga_{1-x}Mn_xN$ epitaxial films deposited on sapphire substrate and a comparison of optical properties of doped and undoped $Ga_{1-x}Mn_xN$ epitaxial films and GaN films in the IR range of $200 - 2000$ cm^{-1} (5 - 50 μm). In addition, the IR absorption coefficient, which is an important parameter for IR device development, is also discussed in the range of 200 - 2000 cm^{-1} (5 - 50 μm).

2.3.1 Sample preparation and reflection measurements

Three n-doped (Si) hexagonal $Ga_{1-x}Mn_xN$ expitaxial films, denoted as 1216m, 1218m, and 1221m and one undoped hexagonal $Ga_{1-x}Mn_xN$ film, 1215m ($<1\times10^{16}$ cm^{-3}) were used in this study. The manganese composition, x, was kept at 0.015 for all four samples. The $Ga_{1-x}Mn_xN$ films, 1216m and 1218m, were deposited on n-GaN/GaN/sapphire templates while the $Ga_{1-x}Mn_xN$ films in 1221m and 1215m were deposited on GaN/sapphire templates. The thickness of the GaN epilayer was about 1.8 μm, and the thickness of the n-doped GaN epilayer was about 300 nm. *C*-plane sapphire was used as the substrate. The epilayers were deposited using a customized MOCVD reactor with a vertical injection system. Ammonia, tri-methyl gallium, bis-cyclopenadienyl manganese(Cp_2Mn), and silane (SiH_4) were used as the nitrogen, gallium, manganese, and n-dopant sources respectively for the growth of $Ga_{1-x}Mn_xN$ films. The concentration of the incorporated Mn was controlled through the molar flow of Mn going into the reactor. A detailed description of the growth process is reported elsewhere [3]. Room temperature and near normal ($\sim 8^0$) incidence IR reflection measurements were performed over the frequency range of 200 - 2000 cm^{-1} (50-5 μm) by using Perkin-Elmer System 2000 FTIR as discussed in Section 2.1.5.

The IR reflection spectra were taken under s-polarized and near normal ($\sim 8^0$) incident light arrangement to minimize the effect of the anisotropy of hexagonal $Ga_{1-x}Mn_xN$ film.

The dielectric function of doped $Ga_{1-x}Mn_xN$ films in the IR region is predominantly determined by the phonon and free carrier contributions. The phonon contribution can be modeled using a Lorentz harmonic oscillator as shown in Section 2.1.1. The free carrier plasma contribution is due to the interaction of free carrier with the electric field of the incident light. It can be modeled by using a classical Drude model approximation as discussed in Section 2.1.2. Hence, a complete but simple model for the dielectric function for doped $Ga_{1-x}Mn_xN$ films can be presented as in Eq. 2.31 for the IR region[36, 41],

$$\varepsilon(\omega, n) = \varepsilon_\infty[1 + \frac{\omega_{LO}^2 - \omega_{TO}^2}{\omega_{TO}^2 - \omega^2 - i\omega\Gamma} - \frac{\omega_p^2(n)}{\omega^2 + i\omega\gamma_p}]. \tag{2.31}$$

This model addresses the phonon-plasmon coupling. The fitting process was carried out as in Section 2.1.5 to get the best fit parameters for Si-doped $Ga_{1-x}Mn_xN$ (x=1.5%) epilayers.

2.3.2 Results and Discussion

Optical constants ε_∞, ω_{LO}, ω_{TO}, Γ, ω_p, and γ_p for $Ga_{1-x}Mn_xN$ films were extracted by fitting the experimental IR reflectance spectra. The experimental and modeled IR reflection spectra from 200 to 2000 cm^{-1} (50 - 5 μm) are shown in Fig. 2.10. Parameters for doped $Ga_{1-x}Mn_xN$ films are listed in Table 2.4 along with an undoped $Ga_{1-x}Mn_xN$ film parameters for comparison. The $Ga_{1-x}Mn_xN$ film thicknesses in samples 1215m, 1216m, 1218m, and 1221m were found to be 1765, 1252, 424, and 1335 nm respectively. The high frequency dielectric constant, ε_∞ for n-doped and undoped $Ga_{1-x}Mn_xN$ films did not vary

Table 2.4: Parameters obtained from the best fits of IR spectra and sample information. Sample numbers, high frequency dielectric constant (ε_∞), $E_1(LO)$ and $E_1(TO)$ mode frequencies, damping constant of E_1 phonon (Γ), and frequency and damping constant of the plasma oscillator (ω_p, γ_p). The free carrier concentration, n, was derived from the plasma frequency. The Mn composition, x is 1.5% for all four films. Fitting errors are given in parentheses.

Samples	ε_∞	ω_{LO} (cm^{-1})	ω_{TO} (cm^{-1})	Γ (cm^{-1})	ω_p (cm^{-1})	γ_p (cm^{-1})	n (10^{18} cm^{-3})
1215m	5.22(0.04)	745(1)	564(1)	9.6(0.3)	N/A	N/A	< 0.01
1216m	5.17(0.04)	745(2)	561(1)	6.5(1.1)	130(20)	150(90)	0.2
1218m	5.20(0.10)	747(5)	563(1)	8.0(1.9)	366(24)	130(57)	1.8
1221m	5.16(0.05)	754(2)	562(1)	8.1(1.3)	407(10)	387(32)	2.1

much and stayed around 5.2. The free carrier concentration, n, was calculated by using Eq. 2.32.

$$\omega_p = [\frac{ne^2}{m_* \varepsilon_\infty \varepsilon_0}]^{1/2}, \tag{2.32}$$

where ω_p is plasma frequency obtained from the fitting, e is the electron charge, m_* is the electron effective mass, and ε_0 is the permittivity in free space. m_* was taken as $0.2m_0$ where m_0 is the free electron mass. The plasma frequencies for the three n-doped films, 1216m, 1218m, and 1221m are 130, 380, and 422 cm^{-1}, respectively. From these plasma frequencies, the calculated free carrier concentrations for 1216m, 1218m, and 1221m are $\sim$ 0.20, $\sim$ 1.8, and $\sim$ 2.1 $\times 10^{18}$ cm^{-3}, respectively. It has been shown in Section 2.2.3 that the frequency of $E_1(TO)$ of undoped $Ga_{1-x}Mn_xN$ shifts linearly with Mn composition [42] and was found to be at 564 cm^{-1} for 1.5% Mn concentration. However, the frequency of $E_1(TO)$ of Si doped $Ga_{1-x}Mn_xN$ films (0.02 - 2.1 $\times 10^{18}$ cm^{-3}, x = 0.015) is slightly smaller and remains around 562 cm^{-1} [see Table 2.4]. This can be due to the extra strain in the lattice introduced by Si dopants. The $E_1(LO)$ frequencies for both undoped (1215m, $<1\times10^{16}$ cm^{-3}) and low doped (1216m - 0.2×10^{18} cm^{-3}) $Ga_{1-x}Mn_xN$ films are at $\sim$ 745 cm^{-1}, which is slightly higher than the reported values for GaN; 742.1, 738.4, 737.5 cm^{-1} by Kasic and Schubert [36], and 741 cm^{-1} by H. Harima [2]. The $E_1(LO)$ frequencies for samples 1218m and 1221m shifted to higher frequencies. This may be due to the stronger LO-phonon and plasmon coupling (LPP). When the plasma frequency gets closer to the LO-phonon frequency, the coupling gets stronger and therefore LO frequency shifts to higher frequency[41].

The free carrier concentration for sample 1221m by Hall measurement is 1.6 $\times 10^{18}$

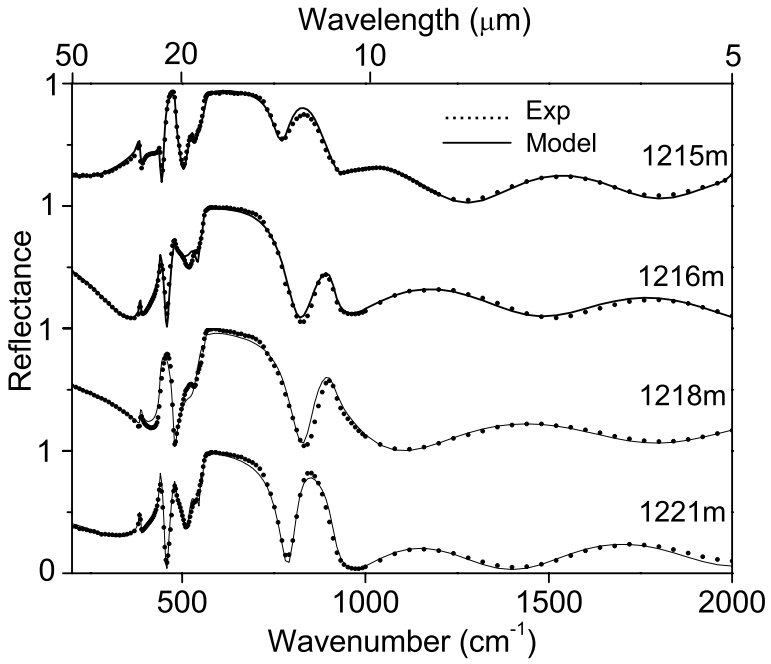

Figure 2.10: Experimental infrared reflectance spectra (dotted lines) of the $Ga_{1-x}Mn_xN$ films on sapphire substrates and the best fit using the Eq. 2.31 (solid lines). For clarity, each spectrum is successively shifted by 1.0 in the vertical direction.

cm^{-3} and roughly matches with the value obtained from fitting, 2.1×10^{18} cm^{-3}. However, the free carrier concentration of 1216m and 1218m films determined by Hall measurements are in rather poor agreement with the results obtained from IR reflection fitting. The average free carrier concentrations of sample 1216m and 1218m from Hall measurements are 3.5 and 4.7 $\times10^{18}$ cm^{-3} whereas, by fitting, are 0.2 and 1.8 $\times10^{18}$ cm^{-3}, respectively. This deviation is assigned to the extra n-doped GaN epilayer under the $Ga_{1-x}Mn_xN$ film in these two samples. The estimated free carrier concentration (from the IR reflection fittings) of this n-doped GaN epilayer is $\sim 6\times10^{18}$ cm^{-3}. The Hall technique measures the average free carrier concentration of the structure under test. Therefore, in this case, the free carrier concentration obtained from the Hall measurements is strongly affected by the n-doped GaN layer. Hence, the free carrier concentration obtained from Hall measurement is an average measurement of the top two doped layers. The IR reflection technique has the advantage in these type of situations.

The coupling of $A_1(LO)$ and plasmons, LPP modes, is expected when free carriers are present in the material and is stronger when the plasmon frequency ω_p is near the frequency of $A_1(LO)$. The LPP mode behaviors for n-doped films 1216m, 1218m, and 1221m are shown in Fig. 2.33 (a), (b), and (c), respectively. Frequencies of LPP^+ are 750, 800, and 810 cm^{-1} while frequencies of LPP^- are 85, 260, and 255 cm^{-1} for sample 1216m, 1218m, and 1221m, respectively. LPP mode frequencies can be theoretically calculated by setting the dielectric function (Eq. 2.31) to zero in the limit of zero damping and given as follows;

$$\omega_{\pm}^2 = \frac{\omega_{LO}^2 + \omega_p^2}{2} \pm [\frac{(\omega_{LO}^2 + \omega_p^2)^2}{2} - \omega_p^2\omega_{TO}^2]^{1/2}. \tag{2.33}$$

Figure 2.11 (d) shows the theoretically predicted LPP mode behavior and experimentally deduced LPP frequencies as the free carrier concentration increases. Generally, the LPP^+ mode reaches ω_{LO} and the LPP^- mode reaches zero as the free carrier concentration reaches zero (see the two solid lines in Fig 2.11 (d)). Therefore, the LPP^+ mode shows ω_{TO} phonon - like behavior at low doping. As the free carrier concentration increases, the LPP^+ mode approaches ω_p while the LPP^- mode approaches ω_{TO} (see the two solid lines). Therefore, the LPP^+ mode shows plasmon like behavior at higher doping.

A knowledge of the IR absorption coefficient of materials, α, is important for designing infrared devices and can be calculated using Eq. 2.34

$$\alpha = \frac{4\pi Im(n)}{\lambda} \tag{2.34}$$

where $Im(n)$ is the imaginary part of the complex refractive index of the film and λ is the wavelength. The calculated absorption coefficients for all four films are shown in Fig. 2.12 in the range of 200 - 2000 cm^{-1} (5 - 50 μm). The absorption coefficient peaks in the GaN restrahlen band and reaches its maximum of 1×10^5 cm^{-1} around the frequency 560 cm^{-1}. The absorption peak gets broader with increasing free carrier concentration. For highly doped $Ga_{1-x}Mn_xN$ films, the line width of the absorption peak has increased by about 35 - 40% with respect to undoped or low doped $Ga_{1-x}Mn_xN$ films. This broadening is due to the LPP^+ mode shifting to higher frequency with increasing doping. At wavenumber 200 cm^{-1} (50 μm), absorption has increased from 12 cm^{-1} to roughly 7500 cm^{-1} as the doping level was increased to 2.1×10^{18} cm^{-3} from undoped ($<1\times10^{16}$ cm^{-3}). The increase in α at wavenumber 200 cm^{-1} is an advantage for far infrared detectors. In addition, in the short wavelength region (1000 - 2000 cm^{-1}), α has increased, at least, by a factor of five in higher

doped $Ga_{1-x}Mn_xN$ film. In general, α increases with increasing free carrier concentration.

In conclusion, the high frequency dielectric constant (ε_∞) and optical phonon modes $E_1(LO)$, $E_1(TO)$ were investigated. The high frequency dielectric constant, ε_∞, in n-doped $Ga_{0.985}Mn_{0.015}N$ films is between 5.2 - 5.3. $E_1(TO)$ of doped $Ga_{0.985}Mn_{0.015}N$ films is slightly smaller than that of the undoped ones. It is clearly seen that $E_1(LO)$ frequency increases with increasing free carrier concentrations in the range investigated (2×10^{17} - 3×10^{18} cm^{-3}).

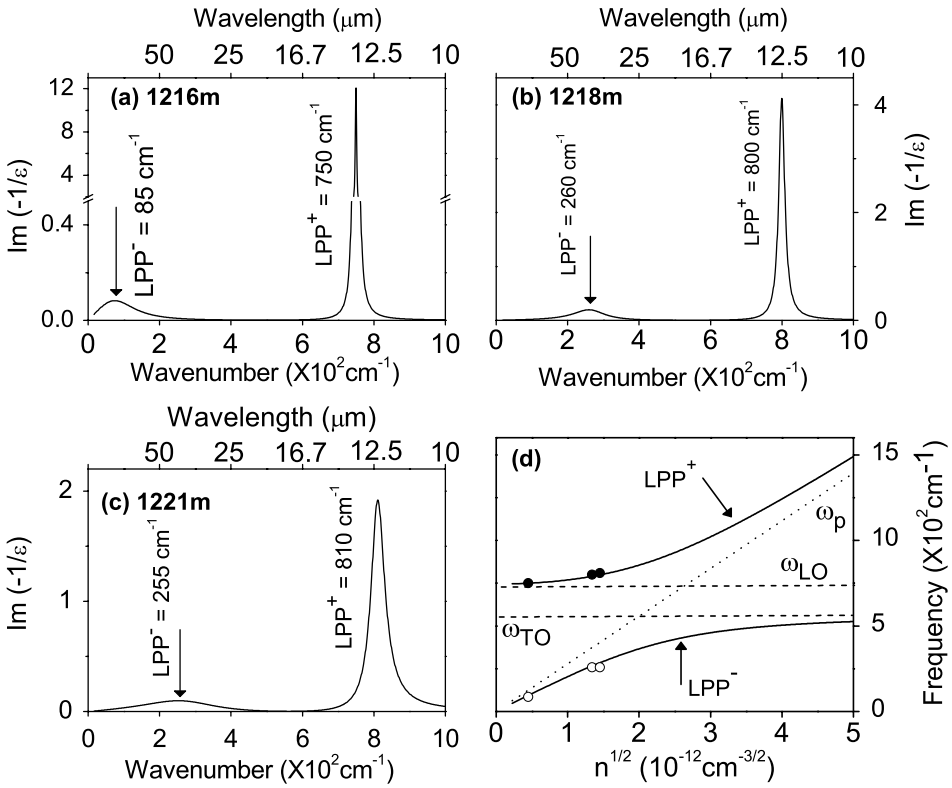

Figure 2.11: $Im(-1/\varepsilon)$ as a function of frequency is shown for three doped $Ga_xMn_{1-x}N$ samples; (a) 1216m, (b) 1218m, and (c) 1221m. Plasmon and phonon coupling modes LPP^+ and LPP^- are clearly visible. A comparison of experimentally derived and theoretically predicted LPP mode behavior with square root of free carrier concentration is shown in (d). Solid lines: theoretically predicted behavior of LPP^+ and LPP^-; solid dots and white circles: experimentally obtained LPP mode values; dashed lines: ω_{TO} and ω_{LO}; and dotted line: ω_p variation.

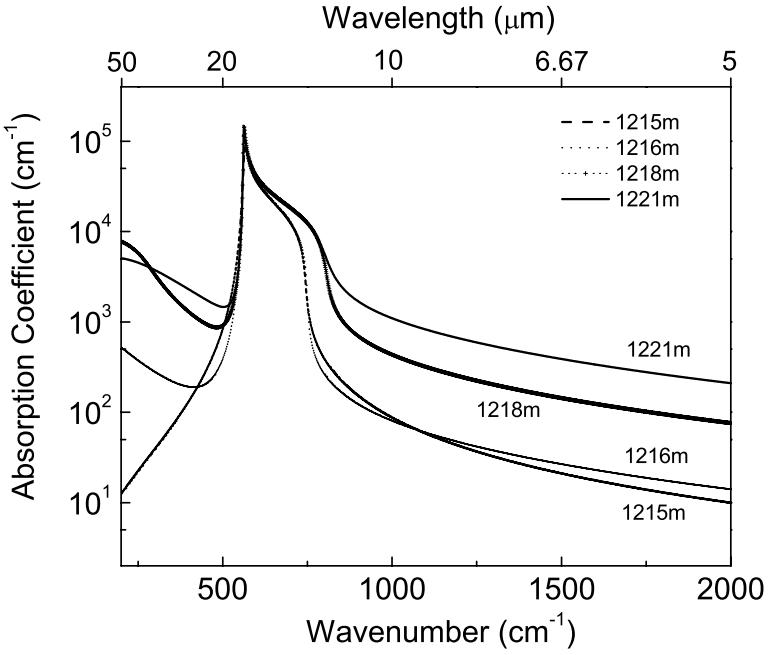

Figure 2.12: The derived absorption coefficients α for all four $Ga_{1-x}Mn_xN$ films with $x =$ 1.5% in the 200 - 2000 range cm^{-1} (50 - 10 μm). The absorption coefficient reaches its maximum at 550 cm^{-1}. The width of the absorption peak has increased by 35 - 40 % in higher doped films ($> 1\times10^{18}$ cm^{-3}).

2.4 Investigating optical properties of Indium Nitride (InN) grown by High-Pressure CVD

InN is one of the materials that is being investigated by scientists around the world for growth techniques and methods to realize quality InN. However, it may take a few more years for InN to be considered for commercial applications. At present, several discussions are taking place over the much controversial fundamental band gap energy which has been reported to be $0.8 - 2.1$ eV [43, 44, 45]. This variation in the bandgap energy may be related to the variations in the InN crystal quality. There is a large potential for InGaN alloy since GaN band gap is as high as 3.4 eV and InN band gap is as low as ~ 0.7 eV. Therefore, the InGaN band gap energy can be literally tuned from 3.4 eV to as low as ~ 0.7 eV enabling numerous optoelectronic applications ranging from ultraviolet through visible to infrared, leading to a great enthusiasm among scientists. Realizing high quality InN crystal is still a challenge. There are several reports of reasonable good quality InN grown by molecular beam epitaxy (MBE) [46, 47, 48] and chemical vapor deposition (CVD) [49, 50]. The main drawback of those two growth methods is the difficulty of achieving a large thermal decomposition pressure [51], which is essential for InN growth. The high pressure CVD method [52, 53] may overcome this problem and may lead to good quality InN films [51, 54].

A good knowledge of optical properties of materials is required when designing opto - electronic devices. Since InN is a new material, experimental studies on InN optical properties are rare. The optical properties of InN have been theoretically predicted, but have not been experimentally verified. Even among the reported experimental results,

there are discrepancies, which are believed to be related to the material quality and the different growth techniques employed. Therefore, studying optical properties of InN grown by HPCVD is crucial in order to improve the material quality.

2.4.1 InN sample growth and IR reflection measurements

The InN films were grown at HPCVD facilities in the Department of Physics and Astronomy at Georgia State University. Details of the growth method and technique can be found elsewhere [51, 54]. In this study, a series of InN films grown on GaN/Sapphire templates and Sapphire substrates were investigated using normal incidence IR reflection spectroscopy at room temperature. Normal incidence IR reflection measurements at room temperature were carried out in the 1000 - 8000 cm^{-1} frequency range ($\sim$ 1.25 - 10 μm) as discussed in Section 2.1.5. The sample numbers and sample growth conditions such as reactor pressure, growth temperature, flow ratios, time duration, and type of template/substrate are given in Table 2.5. IR reflection spectra of samples 136U(D), 136L(A), 142U(A), 146L(A), 146L(B), and 146U(B), which were grown on Sapphire as shown in Fig. 2.13 (a), were modeled using a three phase model (air/InN/Sapphire) while the spectra of samples 76U(A), 102U(A), 110U(G), 139U(A), and 139U(D), which were grown on GaN/Sapphire templates as shown in Fig. 2.13 (b), were modeled using a four phase model (air/InN/-GaN/Sapphire).

2.4.2 Results and discussion

The best fit parameter values obtained for thickness, high frequency dielectric constant (ε_∞), plasma frequency (ω_P), and damping constant of plasma oscillator (Γ) of the

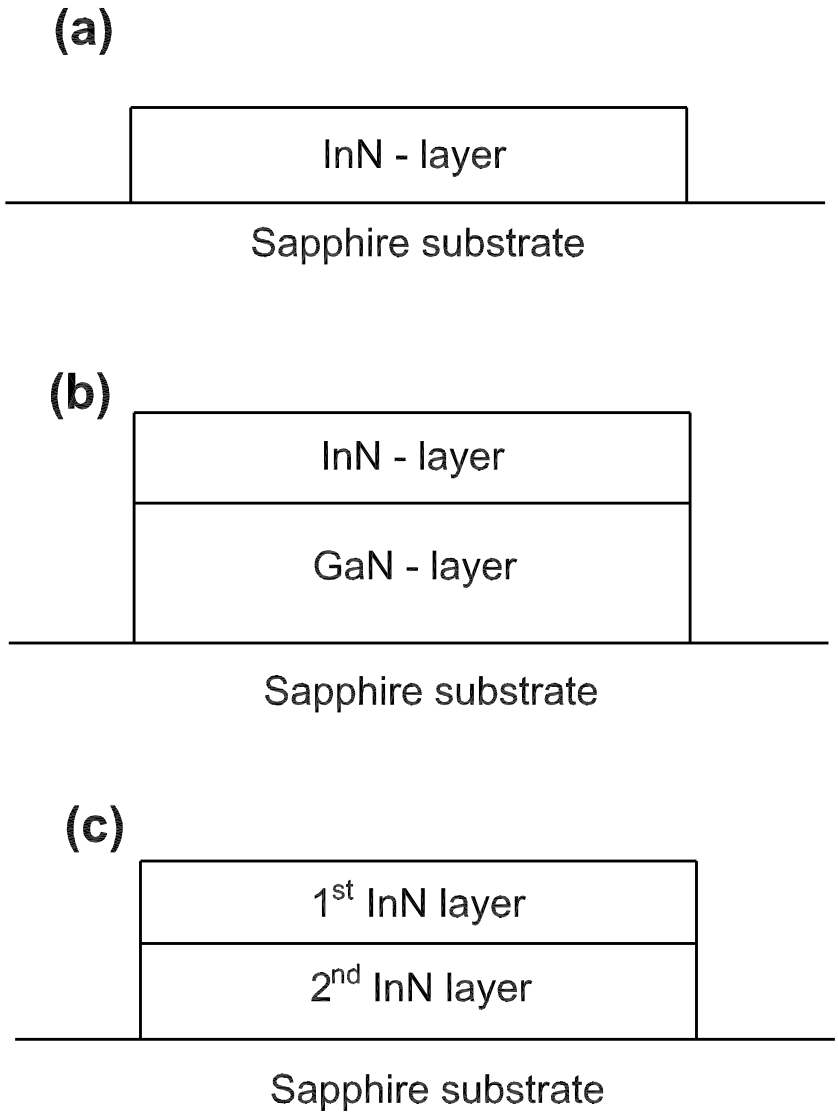

Figure 2.13: (a) A InN layer grown on Sapphire substrate (b) A InN layer grown on ~ 1 μm thick GaN layer and sapphire. (c) Two layer InN formation seen in samples 139U(B), 139U(D), 142U(A), and 146U(B).

InN layers are given in Table 2.6 for samples 76U(A), 102U(A), 110U(G), 136U(D), 136L(A), 146L(A), and 146L(B). Dielectric function of InN films were modeled using Eq.2.31, which takes longitudinal phonon and plasmon coupling into account. The InN optical phonon frequencies of $E_1(TO)$ and $E_1(LO)$ were kept fixed at 479 and 590 cm^{-1}, respectively. It was found from the best fitting that reflection spectra of these structures are dominated by the plasma frequency, which is much higher than the optical phonon frequencies. Therefore, it is reasonable to keep the optical phonon frequencies fixed. The experimental spectra and the best fitted spectra of these samples are shown in Fig. 2.14. Due to the higher reflection below 1000 cm^{-1}, the experimental spectra has no significant features such as strong phonon lines. According to the fitting analysis, the high frequency dielectric constant, ε_∞ varies from 5.6 to 8.4 with an average value of 7.0. Other reported values for the high frequency dielectric constant, ε_∞ are so far controversial; 9.3 Ref. [55], 8.4 Ref. [56], 7.5 and 6.7 Ref. [57], and 5.8 Ref. [58]. The oxide formation and voids in the InN layer may be reasons for these variations in ε_∞. From the plasma frequency, the bulk free carrier concentration of these samples can be estimated by using Eq. 2.32. The electron effective mass m^* was taken as $0.09m_0$ and the corresponding ε_∞s of InN layers were used. The obtained free carrier concentrations from IR reflection spectra fitting of these samples are listed in Table 2.6 and are in the upper 10^{19} or lower 10^{20} cm^{-3} range. The carrier mobility can be estimated using the broadening constant, (Γ) as given in Eq. 2.35.

$$\mu = \frac{e}{m_e^* \Gamma}, \tag{2.35}$$

The electron effective mass, m_e^* was taken as $0.09m_0$ [48]. The estimated mobility is below 500 m/V.s which is reasonable for high free carrier densities.

Table 2.5: The growth parameters of the InN/GaN/Sapphire and InN/Sapphire structures. Reactor pressure was at 15 bar and the total gas flow rate was at 12 slm (standard litters per minute).

Sample tag	III/V ratio during		Temp (K) during		Substrate	Growth duration (min)
	Nucleation	Growth	Nucleation	Growth		
76U(A)	400	800	1100	1090	p-GaN/Sapp	90
102U(A)	400	800	1100	1090	p-GaN/Sapp	90
110U(G)	400	800	1100	1085/90	p-GaN/Sapp	180
136U(D)	400	800	1100	1090	Sapp	180
136L(A)	400	800	1100	1078	Sapp	180
139U(B)	400	800	1100	1090	p-GaN/Sapp	90
139U(D)	400	800	1100	1090	p-GaN/Sapp	90
142U(A)	400	800	1100	1090	Sapp	180
146L(A)	400	800	1100	1090	Sapp	180
146L(B)	400	800	1100	1090	Sapp	180
146U(B)	400	800	1100	1090	Sapp	180

Two InN layers as shown in Fig. 2.13 (c) with different doping concentrations were found to be required to model the IR reflection spectra of sample 139U(B), 139U(D), 142U(A), and 146U(B) (see Fig. 2.15). The best fit parameters of those two layers are listed in Table 2.7 with the estimated free carrier concentration. In Table 2.7, the top most layer of the structure, which is open to air, is labeled as the 1^{st} layer and the 2^{nd} layer is under the 1^{st} layer (see Fig. 2.13 (c)). The plasma frequency of the 1^{st} layer is much higher and so is the free carrier concentration. The free carrier concentrations of the 1^{st} layer of samples 142U(A) and 146U(B) are not given since ε_∞ is quite small, which suggests that these layers could be contaminated with O_2 giving a mixture of indium oxide and InN. The 2^{nd} layer was found to be low in free carrier concentration but only a few tens of nanometers in thickness. It reveals that an InN layer with a low free carrier concentration has been formed during the growth of the first few tens of nanometers. After that, the free carrier concentration in the InN layer rapidly increased so that it had to be considered as a separate layer for modeling purposes. The average ε_∞ value of these low doped InN layers is around 8, which is close to 8.4, the theoretically predicted value [59] . It should be noted that ω_p and Γ were found to be below 200 and 100 cm^{-1}, respectively, but a precise values could not be found from the fits. The reason for this is that ω_p of the top most layer is much higher than that of the 2^{nd} layer and it has overshadowed the plasma oscillator of the 2^{nd} layer. Therefore, the fitting algorithm could not find a reasonable minimum. In conclusion, the average ε_∞ value of InN grown by HPCVD was found to be between 7.0 and 8.4. In some samples, it revealed that InN layer with low free carrier concentration started to grow, but after few decades of nanometers, the free carrier concentration dramatically increased.

Table 2.6: The IR reflection spectroscopy fitting parameters of 76U(A), 102U(A), 110U(G), 136U(D), 136L(A), 146L(A), and 146L(B). InN layer thickness (t), high frequency dielectric constant (ε_∞), plasma frequency (ω_P), damping constant (Γ), and calculated carrier mobility (μ) are given. Statistical errors from the fitting algorithm are given within the brackets.

Sample	t (nm) ($< \pm 5\%$)	ε_∞ ($< \pm 5\%$)	ω_p (cm^{-1}) ($< \pm 10\%$)	$n \times 10^{19}$ (cm^{-3}) ($< \pm 10\%$)	Γ (cm^{-1}) ($< \pm 5\%$)	μ ($cm^2/V{\cdot}s$) ($< \pm 5\%$)
76U(A)	256	5.6	3612	7	228	455
102U(A)	242	6.2	4050	10	300	345
110U(G)	550	7.0	3990	11	630	164
136U(D)	370	7.2	4777	16	1427	72
136L(A)	535	8.4	4796	19	949	109
146L(A)	343	7.6	4688	16	895	115
146L(B)	281	7.6	4686	16	651	159

Table 2.7: The IR reflection spectra fitting parameters of 139U(B), 139U(D), 142U(A), and 146U(B). Evidence for the existence of two separate InN layers was found by the IR spectra fittings for these structures (see Fig. 2.13 (c)). Layer thickness (t), high frequency dielectric constant (ε_∞), plasma frequency (ω_P), damping constant (Γ), and estimated free concentration (n) are given for each layer. The layer next to p-GaN or Sapphire is the 2^{nd} layer and the layer above is the 1^{st} layer. All the statistical errors from the fitting algorithm are less than 6 % of the original values.

	139U(B)	139U(D)	142U(A)	146U(B)
1^{st} layer				
t (nm)	373	352	276	554
ε_∞	8.4	8.8	4.7	3.3
ω_p (cm^{-1})	3110	3236	3688	3740
Γ (cm^{-1})	423	336	551	387
n ($\times 10^{19} cm^{-3}$)	$\sim$8	$\sim$9		
2^{nd} layer				
t(nm)	64	128	70	33
ε_∞	8.4	7.0	8.1	8.1
ω_p (cm^{-1})	$<$200	$<$200	$<$200	$<$200
Γ (cm^{-1})	$<$100	$<$100	$<$100	$<$100
n ($\times 10^{17} cm^{-3}$)	$<$5	$<$5	$<$5	$<$5

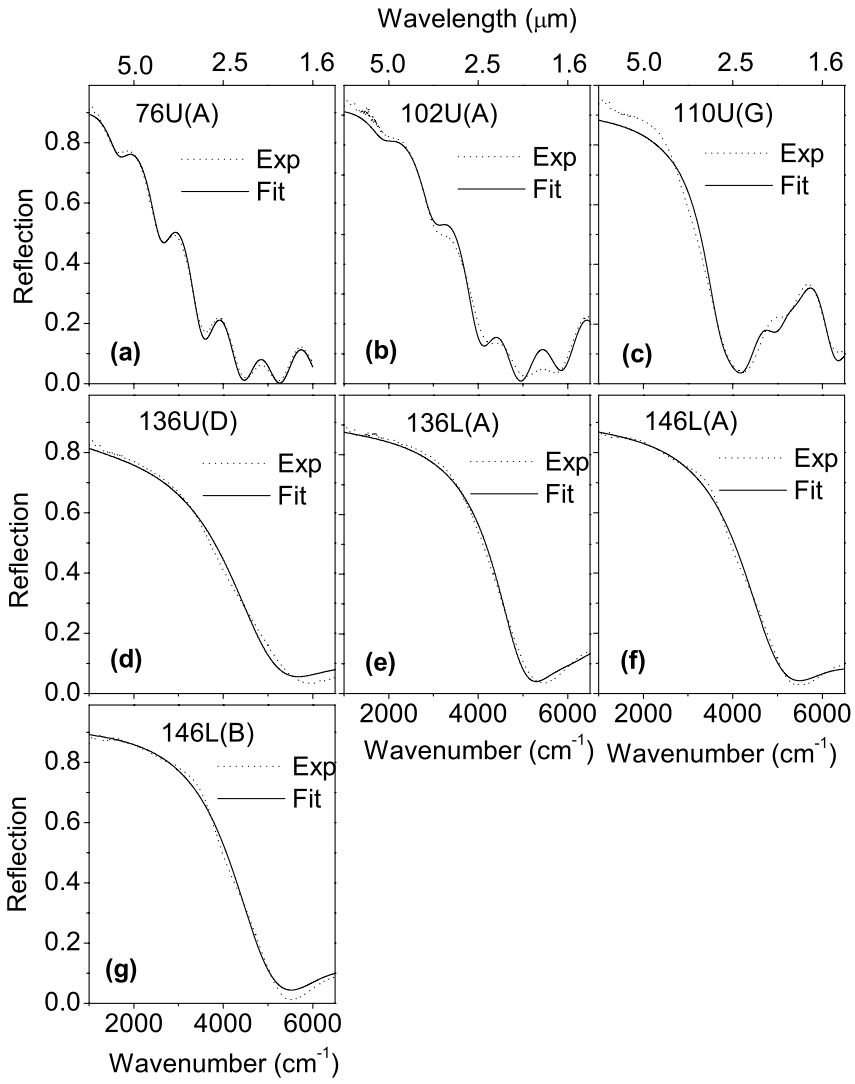

Figure 2.14: The experimental IR spectra and their best fit curves of samples 76U(A), 102U(A), 110U(G), 136U(D), 136L(A), 146L(A), and 146L(B) are shown. The fitting parameters are given in Table 2.6.

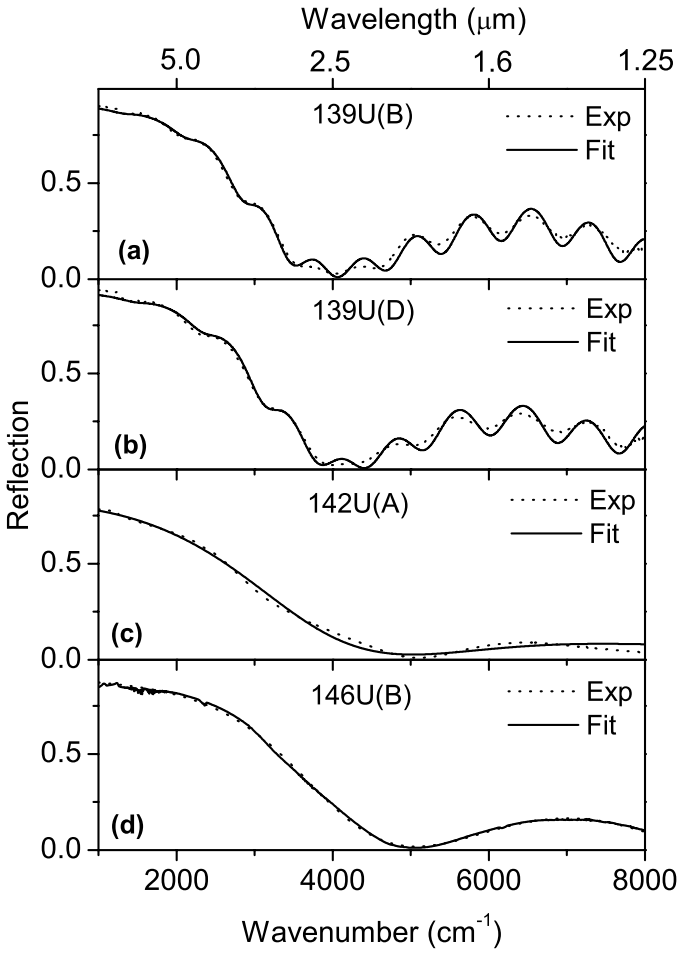

Figure 2.15: The experimental IR spectra and their best fit curves of samples 139U(B), 139U(D), 142U(A), and 146U(B) are shown. These sample structures shows two InN layers with one low free carrier concentration and the other with higher free carrier concentration. The fitting parameters are given in Table 2.7.

Chapter 3

Terahertz Detection Using n-type GaAs/AlGaAs Heterostructures

3.1 Introduction

Interest in IR detection started in early 19^{th} century and Herschel [60] noticed that a thermometer showed a higher temperature rise when it was exposed to the red region of the visible light spectrum. Langley invented [60] the first bolometer in 1880. However, IR detector technology grew rapidly after the mid 20^{th} century mainly due to the development of the semiconductor technology. IR detectors can be categorized mainly into two groups; (a) thermal detectors which utilize a certain material property change due to the temperature variation in materials upon IR radiation absorption and (b) photon detectors which utilize the electric conductivity change in the material due to the electron and hole distribution change upon photon absorption. Photon detectors are faster, have a better signal-to-noise ratio, and can be employed in $2D$ array systems for imaging easily while

thermal detectors are slow in response and are difficult to use in $2D$ array systems for imaging. In general, thermal detectors have specific applications because of the slow response time. Generally, most of the thermal detectors can be operated at room temperature and response is independent of the incident wavelength.

Photon detectors based on intrinsic Si, Ge, and InSb can only be operated in 1 - 8 μm IR range, whereas detectors based on extrinsic semiconductors can operate up to $\sim$ 20 μm. In general, MCT can be operated in $2 - 20$ μm. Most of Quantum Well Infrared photodetectors (QWIPs) can operate around 10 μm. However, QWIPs have been reported to work even at longer wavelengths; 28 and 35 μm cutoff wavelengths [61, 62] and more recently up to 70 μm cutoff wavelength [63]. Bolometers and Phyroelectric detectors, which are thermal detectors, are the FIR detectors available in the market for wavelengths beyond 20 μm although HIWIP and HEIWIP detectors and terahertz QWIPs have shown FIR/terahertz detection capability at research level. HIWIP detectors with p-type emitters have been reported to have threshold wavelengths longer than 70 μm [64, 65], and the longest wavelength reported for a HIWIP detector is 105 μm [64]. HEIWIP detectors with p-type emitters have been extensively reported [5, 11, 12, 66] and the longest threshold wavelength of a p-type HEIWIP is 128 μm (2.34 THz). It is clear that HIWIP and HEIWIP detectors can operate in FIR/terahertz range.

A HIWIP detector consists of an undoped layer and a doped layer of the same material, and a potential barrier due to the doping arises at the interface of the two layers and is called the internal workfunction (Δ). IR absorption occurs in the doped layer and photoexcited carriers are emitted over the internal workfunction. In HEIWIP detectors,

the two layers are different materials, which give an internal workfunction (Δ) due to the material composition and doping at the heterojunction interface.

3.2 General theory of HEIWIP detectors

The HEIWIP detector mechanism mainly consists of photon absorption by free carriers in the doped emitter and the photoexcited carrier emission over the heterojunction potential barrier. Photoabsorption occurs in the heavily doped emitter and then the internal photoemission occurs over the heterojunction barrier, and the photoexcited carriers are swept away by the external field and can be collected via electrical contacts. Detectors based on free carrier absorption are good candidates for far infrared/terahertz detection. In HEIWIP structures, an undoped semiconductor alloy layer is used as the barrier and a doped semiconductor layer is used as the emitter. The internal workfunction or the interface barrier, Δ, is defined from the top of the Fermi energy level in the emitter layer to the bottom of the conduction band (C.B.) of the barrier layer as shown in Fig. 3.1 for n-type detectors. In p-type detectors, Δ is defined from the Fermi level to the bottom of the valence band (V.B.) of the barrier. The Internal workfunction is given by $\triangle = \triangle_x + \triangle_{narr} - E_F$, where $\triangle_x$ is the conduction band offset between the emitter and the barrier due to alloy composition (x), $\triangle_{narr}$ is the band gap narrowing in the emitter layer due to doping, and E_F is the Fermi energy with respect to the bottom of the emitter conduction band (see Fig. 3.1). Photoabsorption occurs in the doped emitter layer and photoexited carriers can be swept out and can be collected at the collector (contact) with an external electric field as shown in Fig. 3.2. The threshold frequency, f_0, is given by $f_0 = \triangle/4.133$ in terahertz.

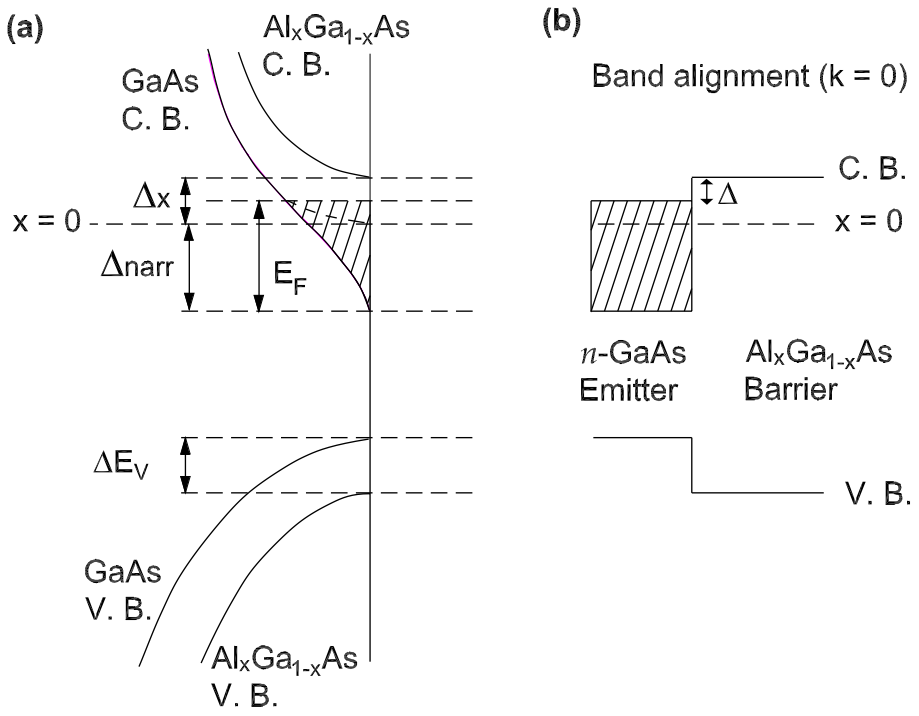

Figure 3.1: (a) The band diagram ($E-k$) of an n-type GaAs/$Al_xGa_{1-x}As$ HEIWIP device showing the conduction band (C.B.) offset (Δ_x) due to the Al fraction, and the band gap narrowing (Δ_{narr}) due to doping, Fermi energy (E_F), and the workfunction (Δ). The C.B. shift occurs due to the doping. The dashed line at $x = 0.0$ shows the C.B. of intrinsic GaAs. The workfunction (Δ) is measured from the Fermi energy to the C. B. bottom of $Al_xGa_{1-x}As$. (b) The band diagram for the same n-type GaAs/$Al_xGa_{1-x}As$ HEIWIP structure at $k = 0$.

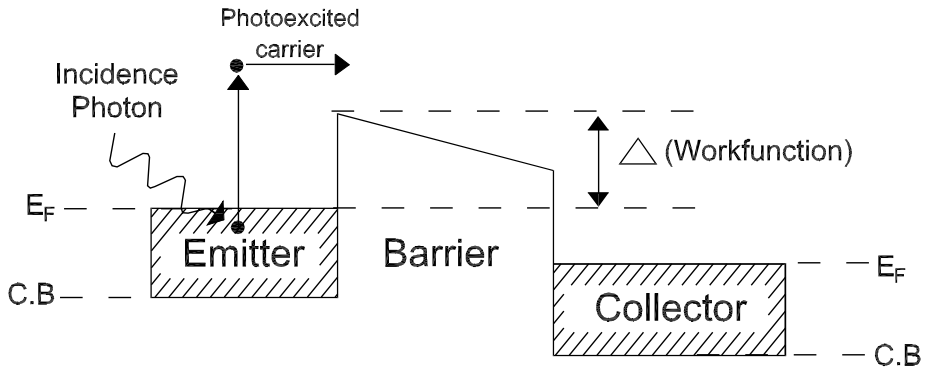

Figure 3.2: The light detection process in an n -type HEIWIP under an external bias field. Free carrier photoabsorption occurs inside the emitter and photoexcited carriers with sufficient energy are emitted over the workfunction (Δ) and can be collected by applying an external electric field. The threshold wavelength (or frequency) is determined by Δ which is measured from the Fermi level to the bottom of the conduction band (C.B) of the barrier.

Here $\triangle$ is in units of meV. The threshold frequency of the detector, f_0, can be tailored by changing [12, 14] the alloy fraction x because Δ changes with x. In general, detectors based on the free carrier mechanism show a broader spectral response when compared to the other types of photon detectors since the free carrier absorption is naturally broad. IR detector performance is characterized by several parameters such as photoresponsivity (R_p), specific detectivity (D^*), dark current (I_d), and Background Limited Infrared Performance (BLIP) temperature. These parameters can be determined for any IR detector by experiment and tested against theoretical estimations. Responsivity (R_p) is defined as the detector photocurrent per unit power of incident radiation and is given as follows

$$R_p(\lambda) = \eta g_p \frac{q}{hc}\lambda, \tag{3.1}$$

Here, η is detector total quantum efficiency and is defined as the number of the photoexcited carriers that contribute to the photocurrent per incident photon, g_p is the photocurrent gain, q is the electron charge, h is Planck's constant, c is the speed of light, and λ is the wavelength of the incident light. Quantum efficiency of HEIWIP detectors depends basically on the photoabsorption efficiency (η_a), which is the free carrier absorption probability, the total internal photoemission efficiency (η_e), and the collection efficiency (η_c) which is usually close to unity because the maximum potential barrier is at the interface. The total quantum efficiency is given by $\eta = \eta_a \eta_e \eta_c$. In detector development, increasing the quantum efficiency is an important issue in order to increase the responsivity and the detectivity. This involves investigating and developing new material structures with higher η_a and higher η_e.

The free carrier absorption in a $3D$ electron (or hole) gas, which is appropriate for

HIWIP and HEIWIP detectors, is given by Eq. 3.2

$$\eta_a = 2\frac{\omega}{c} Im[\varepsilon(\omega)] \frac{1}{|E_0|^2} \int_0^w |E(z)|^2 dz, \tag{3.2}$$

where $Im[\varepsilon(\omega)]$ is the imaginary part of the emitter dielectric function and only the free carrier contribution to the dielectric function should be considered since only the photoexcited carriers contribute to the photocurrent. The photoabsorption part due to the interaction with the lattice can be ignored since it does not excite carriers and therefore, there is no contribution to the detector photocurrent.

The photoemission efficiency (η_e) can be calculated using the escape cone model [67, 68] as explained in the following section. The ideal internal quantum efficiency η_{nidl} for a HEIWIP or HIWIP detector is defined as the number of photoexcited carriers (N) emitted over the interfacial barrier to the number of photoexcited electrons (N_T).

$$\eta_{nidl} = \frac{N}{N_T}, \tag{3.3}$$

If the photoexcited carrier's momentum component normal to the barrier wall is higher than p_0, the photoexcited carriers can escape the barrier, where $p_0 = \sqrt{2m^*(E_F + \Delta)}$ and E_F is the Fermi energy level, m^* is the carrier effective mass, and Δ is the internal workfunction. The distribution of the photoexcited carriers with maximum momentum p is a sphere of radius p. Only a fraction of those excited electrons will have a normal component greater than p_0 and are confined to a cone inside the sphere. Therefore, P_0 defines a cone shaped distribution for photoexcited carriers that can overcome the internal workfunction (Δ). The escape model [67] can calculate the probability of a photoexcited carrier emission over the barrier. The photoexcited carriers outside the cone will not be able to cross the barrier.

Out of the total number of photoexcited carriers with momentum of p, the fraction $f(p)$ that falls inside the escape cone is given by

$$f(p) = \frac{1}{2}(1 - \frac{p_0}{p}), \tag{3.4}$$

Equation 3.4 can be written in terms of energy as follows,

$$f(E) = \frac{1}{2}(1 - \frac{\sqrt{E_F + \Delta}}{E}), \tag{3.5}$$

N_T and N can be written as follows assuming very low temperature ($\ll T\ K$)

$$N_T = \int_{max(E_F,\nu)}^{E_F+\nu} \frac{dN}{dE} dE, \tag{3.6}$$

$$N = \int_{max(E_F+\Delta,\nu)}^{E_F+\nu} \frac{dN}{dE} f(E) dE, \tag{3.7}$$

where ν is the incident photon energy and dN/dE is the density of energy states, which can be approximated to be proportional to $E^{1/2}$. The ratio of the number of photoexcited carriers with kinetic energy higher than the internal workfunction (Δ) to the total number of photoexcited carriers is called the fraction of potentially capturable photoexcited carriers, η_M, and given by,

$$\eta_M = \frac{N_M}{N_T}, \tag{3.8}$$

where,

$$N_M = \int_{max(E_F+\Delta,\nu)}^{E_F+\nu} \frac{dN}{dE} dE, \tag{3.9}$$

The photoexcited carriers in the emitter can undergo various scattering processes and lose energy before reaching the barrier interface. The main scattering processes are inelastic scattering with cold carriers (electron-electron or hole-hole) defined by the scattering length L_e and the elastic scattering with phonons (electron-phonon or hole-phonon) defined by the

scattering length L_p. By taking bulk scattering into account, the total internal quantum efficiency [67, 68], η_e, is given by

$$\eta_e = \frac{\eta_0}{1 - \gamma + + \frac{\gamma\eta_0}{\eta_M}}, \tag{3.10}$$

where, $\gamma = \frac{L_e}{L_e + L_p}$. The fraction of electrons that reaches the barrier before undergoing a bulk scattering and loosing energy is η_0 and is given by

$$\eta_0 = \frac{L^*}{W_d} U(W_d/L^*)\eta_{nidl}, \tag{3.11}$$

where L^* is a measure of scattering length and is equal to $\frac{L_e L_p}{L_e + L_p}$. Furthermore, photoexcited carriers can undergo reflections off the front and back wall of the emitter. This effect [67] is taken into account by including $U(W_d/L^*) \approx [1 - exp(-W_d/L^*)]^{1/2}$ term in Eq.3.11.

Generally, the total quantum efficiency of HEIWIP detector [13] can be as high as 40 % whereas it is under 20 % for QWIPs.

The detector Noise Equivalent Power (NEP), which is another important parameter, is defined as the minimum radiation power incident on the detector that can produce a photocurrent equivalent to the average detector noise current and can be related to the following equation [69]

$$\frac{NEP}{V_n} = \frac{P}{V_s}, \tag{3.12}$$

where P is the total absorbed radiation power, V_s is the voltage signal generated by P and V_n is the noise voltage signal generated by the background radiation. The smaller the NEP, the better the detector performance. The NEP of a detector is an important figure of merit, however, the most important figure of merit for a detector is the specific detectivity (D^*),

which is related to the NEP and is given by

$$D^* = \frac{\sqrt{A\Delta f}}{NEP}, \tag{3.13}$$

where A is the detector optical area and Δf is the signal bandwith. D^* can be related to R_p and detector noise current I_{noise} as follows.

$$D^* = \frac{R_p\sqrt{A}}{I_{noise}}, \tag{3.14}$$

and $I^2_{noise} = 4q\bar{I}g_n\Delta f$, where $\bar{I}$ is the mean current through the detector, g_n is the noise gain, and Δf is the spectral bandwith. The factor g_n is given [66, 70] by

$$g_n = \frac{1}{p_c N}, \tag{3.15}$$

where p_c is defined as the capture probability of carriers inside the emitter and is given by $p_c = \frac{\tau_s}{\tau_s+\tau_{rec}}$ and N is the number of emitters. Here, τ_s is the sweep time that photoexcited carriers take to cross the emitter and τ_{rec} is the recombination time of photoexcited carriers. If $\tau_s \ll \tau_{rec}$, g_n can be further reduced to,

$$g_n = \frac{\tau_{rec}}{\tau_s N} = \frac{\tau_{rec}}{\tau_{tran}} = \frac{\mu\tau_{rec}F}{d}, \tag{3.16}$$

where, τ_{tran} is the total transit time of carriers, μ is carrier mobility, and d is the device thickness.

In Background Limited Infrared Performance (BLIP), the detector dark current can be approximated by $I_{dark} = \bar{I}$, and in the HEIWIP detectors, the dark current due to thermionic emission [14] is given by

$$I_{dark} = qA\frac{\mu F}{[1+(\mu F/\upsilon_{sat})^2]^{1/2}} 2(m^* kT/2\pi\hbar^2)^{3/2} exp[-(\Delta - \alpha F)/kT)], \tag{3.17}$$

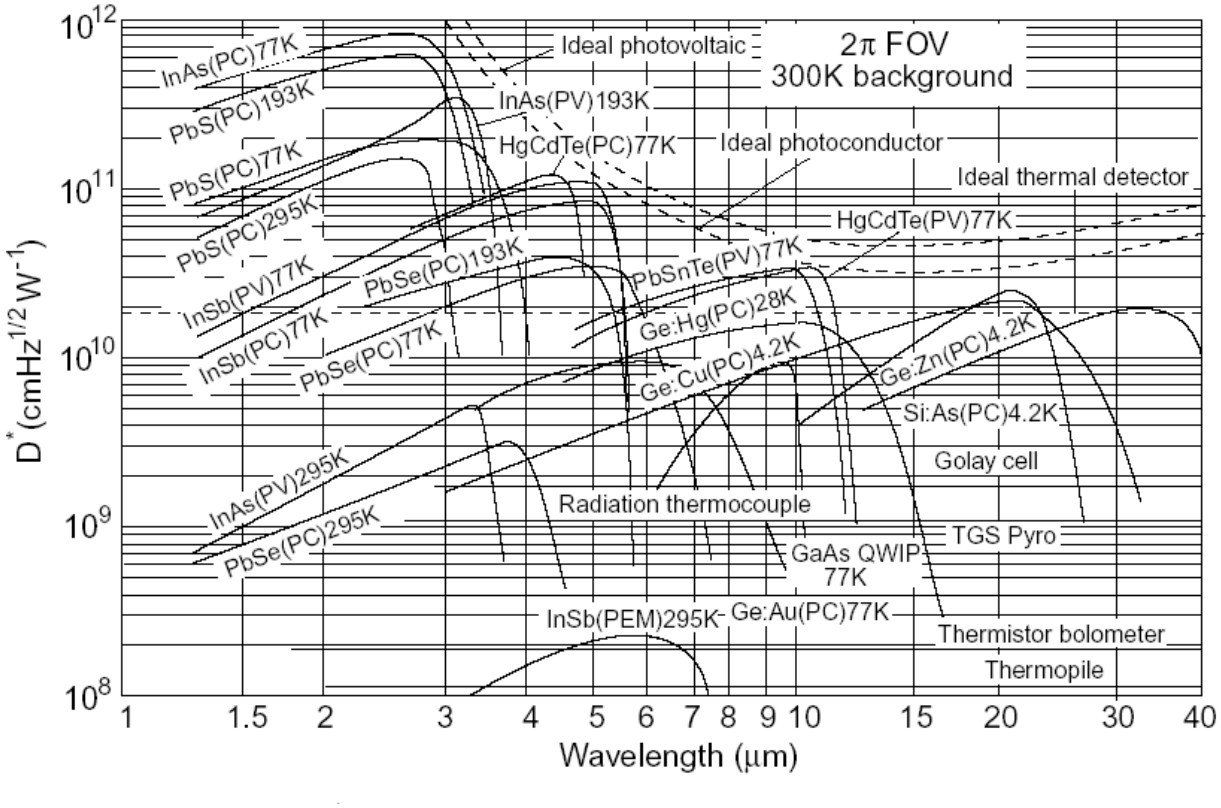

Figure 3.3: Detectivity (D^*) for various available IR detectors under 300 K background. The ideal dectectivity for photovoltaic (PV), photoconductor (PC), thermal, and photoelectromagnetic (PEM) detectors are also given. In general, the highest detectivity can be found in the shorter wavelength region (adapted from Ref. [4])

where F is the electric field, ν_{sat} is the saturation drift velocity of carriers and Δ is the internal workfunction. The parameter α is a fitting parameter that depends on the effective barrier lowering. The specific detectivity D^* is measured in $Jones$ or $cmHz^{1/2}W^{-1}$. The detctivity for widely used detectors are shown in Fig 3.3.

When the detector photocurrent (I_{photo}) is equal to the detector dark current (I_{dark}) at a certain operating temperature which is called the BLIP temperature. The BLIP temperature is another useful parameter in detector characterization, which defines the detector maximum operating temperature (T_{BLIP}). The photo current is given by Eq. 3.18

$$I_{photo} = sin^2(\theta)A \int^{\lambda_0} R(\lambda)\rho(\lambda, T_{BG})d\lambda, \tag{3.18}$$

where 2θ is equal to the field of view (FOV) of the device, ρ is the blackbody radiation intensity at wavelength λ, and the background temperature is T_{BG}, which is normally considered to be 300 K.

3.3 GaAs/AlGaAs n-type HEIWIP detectors

In general, photon detectors based on indium antimonide (InSb) and MCT, QWIP, and block impurity band (BIB) detectors cannot be operated beyond 30 μm [60]. HIWIP and HEIWIP detectors have shown a photoresponse beyond 30 μm, and designing p-type HEIWIP detectors is easier because of the smaller Fermi level shift due to p-doping when compared with n-doping. Therefore, the reported results on HEIWIP detectors are limited to p-type structures[5, 71]. In n-type, the Fermi level changes drastically even for smaller changes in n-doping due to the smaller effective mass of electron. For example, Fermi en-

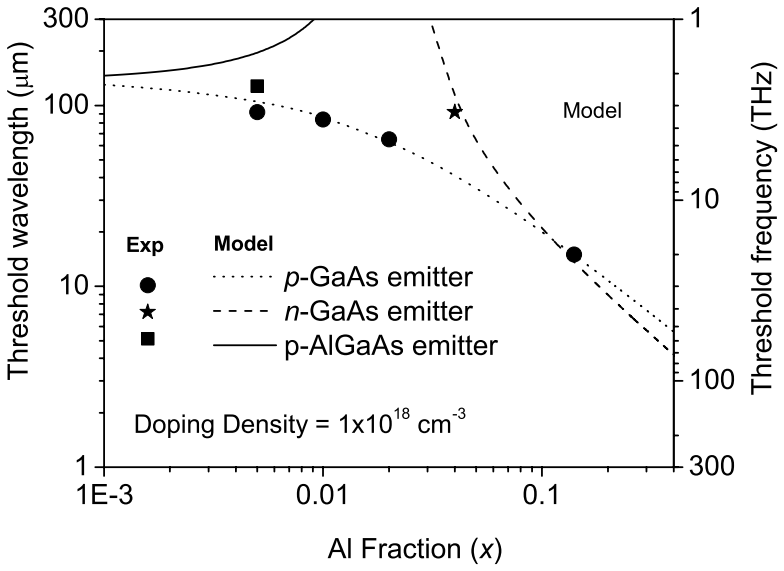

Figure 3.4: Threshold frequency variation for GaAs/$Al_xGa_{1-x}As$ HEIWIP terahertz detectors with Al fraction. The solid line represents p-type inverted structure ($Al_xGa_{1-x}As$ emitter). The dotted and the dashed lines represent usual p-type and n-type (GaAs emitters) structures respectively. Emitter doping in both n- and p- types is kept at 1×10^{18} cm^{-3}. A smaller threshold frequency can be achieved by decreasing the Al fraction in both types of detectors, but, the threshold frequency tends to saturate with decreasing Al fraction in p-type detectors. Solid dots are reported results for p-GaAs emitters, The solid star represents the result of this work, and the solid square is p-AlGaAs emitter previously reported [5].

ergies are 54.5, 86.6, and 159.5 meV in n-type GaAs while Fermi energies are 4.8, 7.8. and 14.3 meV in p-type GaAs for doping concentrations of 1×10^{18}, 2×10^{18}, and 3×10^{18} cm^{-3}, respectively. Because of this, when designing smaller workfunctions for terahertz detectors, the accuracy of doping should be precise in order to get results consistent with designs. HEIWIP detectors with p-type emitters have shown the ability to push the threshold limit beyond 5 THz (>60 μm). Tailoring of threshold frequency f_0 can be achieved by changing the Al fractions, and this has been demonstrated for p-type HEIWIP terahertz detectors with different Al fractions resulting in f_0 = 4.6, 3.6, and 3.2 THz threshold frequencies[12]. The Al fraction used for the 3.2 THz threshold detector is 0.005 and is close to the practical lower limit for MBE growth. It is not possible to lower the workfunction by increasing the emitter doping in p-type HEIWIP since the Fermi level will not reach the required level before GaAs becomes metalic as p-doping increases. Therefore, lowering the workfunction further may not be possible in p-type HEIWIP devices. The theoretical threshold wavelength limit for a device with a 1×10^{18} cm^{-3} p-doped GaAs emitter with a different Al fraction in the barrier is shown in Fig. 3.4 (dotted line). The threshold wavelength of p-doped GaAs emitter devices tends to saturate with decreasing Al fraction. One alternative to this is to use an inverted HEIWIP structure [5]. In inverted HEIWIP structures, p-doped $Al_xGa_{1-x}As$ is used as the emitter and undoped GaAs is used as the barrier. With an inverted structure, it is possible to design a smaller workfunction by increasing the Al fraction and, thereby, a lower threshold frequency can be achieved (see Fig. 3.4). However, the reported lowest threshold [5] obtained with inverted structure is 2.3 THz (128 μm). The other alternative is to use an n-type emitters in HEIWIP detectors. For the same Al com-

position and the same emitter doping concentration, the workfunction in n-type HEIWIP is smaller than the that of p-type HEIWIP due to the higher Fermi energy in n-type compared to that of p-type. According to initial theoretical calculations, it is possible to achieve a threshold frequency below 3 THz in an n-type HEIWIP with a relatively larger Al fraction as seen in Fig. 3.4 (dashed line). For an example, a 1 THz threshold frequency can be achieved in n-type HEIWIP with an Al fraction of 0.03 (3.0%) which is possible in thin film growth techniques. The capability of extending the zero response threshold to the low terahertz limit by using n-type emitters in HEIWIP is experimentally demonstrated and photoemission modeling is carried out for single emitter HEIWIP detector.

Two HEIWIP (a single emitter and a multi emitter) detector structures were designed to test the performance of n-doped GaAs HEIWIP detectors. The single emitter device structure consists of an undoped 1 μm thick $Al_xGa_{1-x}As$ (x=0.04) barrier layer sandwiched between two n-doped (Si) 1×10^{18} cm^{-3} GaAs contact layers with the top contact being 100 nm and the bottom contact being 700 nm in thickness. GaAs n-doped to 5×10^{18} cm^{-3} with Si was used as the substrate to enhance the light reflection from the substrate. The top and the bottom contact layers work as emitters for the reverse and the forward bias operations. The Si doping concentration and the Al fraction were verified by Secondary Ion Mass Spectrometry (SIMS) as shown in Fig. 3.5 (a). The thickness of the top contact layer was kept to 100 nm to allow a substantial amount of light to pass through to the bottom contact layer. NiGeAu was deposited on the bottom and the top contact layers as ring ohmic contacts. Note that the highly doped substrate is electrically isolated from the active layers.

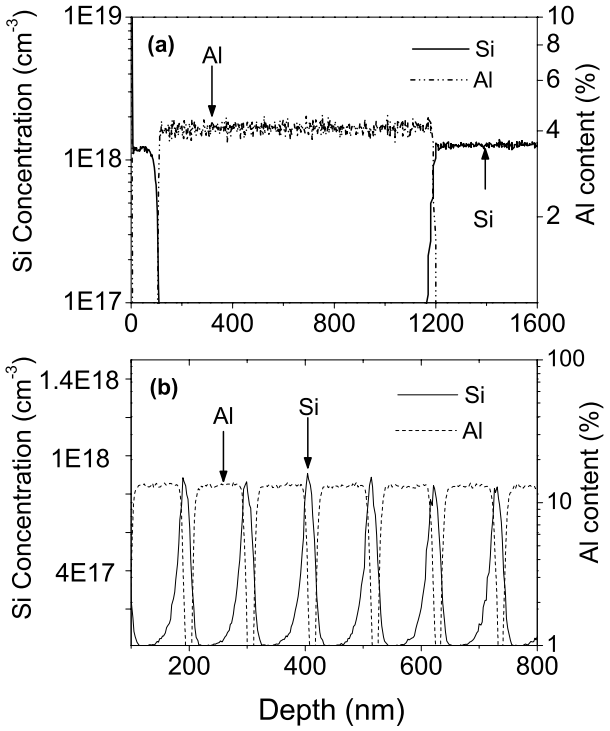

Figure 3.5: (a) SIMS data of single barrier n-type HEIWIP structure. Top and bottom contact layers (emitters) are n-doped to 1×10^{18} cm^{-3}. The aluminum fraction in the barrier is 1 %. (b) SIMS data of the multi emitter structure. Only six periods are shown for clarity. The aluminum fraction is about 13 %. A certain amount of Si migration into the barrier region in the growth direction can also be seen.

The multi emitter device consists of twelve periods of 1×10^{18} cm^{-3} n-doped 20 nm thick GaAs emitters and undoped 80 nm thick $Al_{0.1}Ga_{0.9}As$ barriers. The top and bottom contact layers were 1×10^{18} cm^{-3} n-doped with 100 and 700 nm thicknesses, respectively, and 5×10^{18} cm^{-3} n-doped GaAs was used as the substrate. The device processing was carried out as described for the single emitter structure. SIMS measurements of the Al fraction and the Si concentration of the multiemitter device are given in Fig. 3.5 (b) and the Al fraction was found to be 13 % instead of the nominal value of 10 %. In addition, there is a considerable amount of doping migration into the barrier, which is evident from the SIMS results.

3.3.1 Device characterization

The electron gas in the single emitter structure should be treated as a $3D$ distribution. Therefore, the calculated Fermi energy in the emitter layers of the single barrier device, E_F is 55 meV. The GaAs/$Al_xGa_{1-x}As$ conduction band discontinuity, which is given by Δ_x=790×x (in meV) for x<0.41, is 32 meV for x = 0.04. Considering band gap narrowing [72, 73] of 35 - 45 meV in the GaAs emitter layer due to 1×10^{18} cm^{-3} n doping, the calculated workfunction of the single barrier device is between 11 - 21 meV, which corresponds to a 2.4 - 5.0 THz (125 -60 μm) threshold frequency. This large threshold frequency variation in the estimated values is due to the large uncertainty in the reported [72] band gap narrowing in n-type GaAs materials. Dark current-voltage measurements were performed on the devices from 4.2 to 120 K to obtain the internal workfunction (Δ) using Arrhenius plots as shown in Fig. 3.6. According to Fig. 3.6 (a), the estimated workfunction is 13 - 14 meV (88 - 95 μm) for the single emitter device. Spectral measurements were performed us-

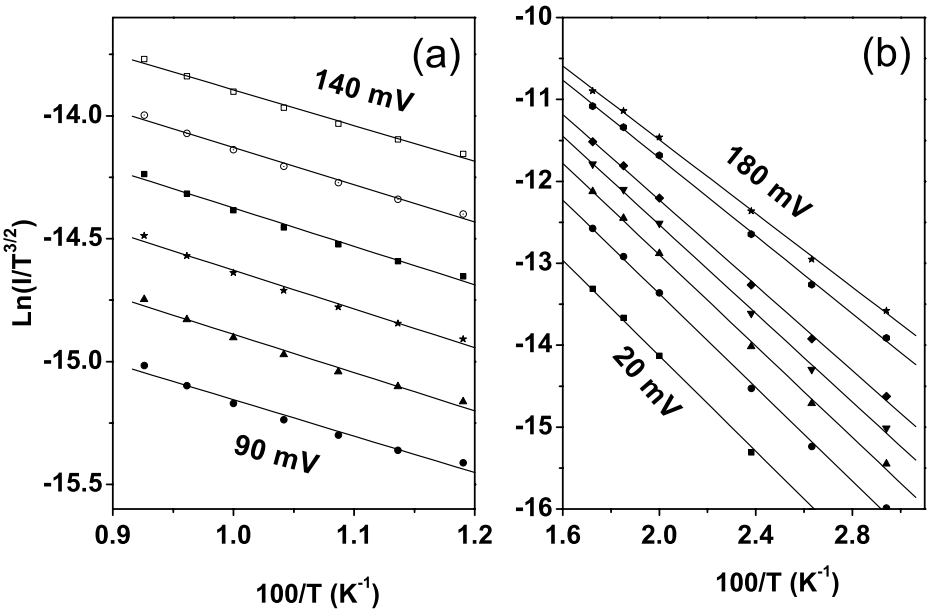

Figure 3.6: (a) Arrhenius plot for the single barrier device under different applied fields. The workfunction is estimated to be 13 ± 1 meV and does not change with the applied bias field. (b) Arrhenius plot for the multi emitter device under different applied fields. The workfunction changes from 25 ± 1 to 18 ± 1 meV as the bias field changes from 0.2 to 1.8 kV/cm, and therefore a threshold variation in spectral response can be expected.

ing the Perkin Elmer System 2000 fast Fourier transform infrared spectrometer (FTIR) and a silicon composite bolometer was used to calibrate the raw photoresponse spectra obtained with the device. Responsivity was calculated by using R = $\frac{R_{raw}}{R_{bol}}\frac{SG}{R_{//}}$. Here R_{raw} and R_{bol} are the detector raw spectral response and the bolometer spectral response, respectively, S is the voltage sensitivity of the bolometer, G is the geometrical area correction factor, and $R_{//}$ is the parallel resistance of the device and the load resistor. The schematic diagram of the experimental setup and detector bias circuit are shown in Fig. 3.7. The Kaiser-Bessel function was selected as the apodization function in the FTIR setup in order to reduce the effects arising from a finite time series. All the spectra presented in this work are an average of at least 200 raw spectra and were taken at the optical path difference (OPD) velocity of 1 cm/s with resolution of 4 cm^{-1}. Responsivity curves for different bias fields are shown in Fig. 3.8 (a) at 6 K. The zero response threshold frequency, which was found to be 3.2 THz (93 μm), was estimated by considering instrument noise level as shown in the inset to Fig. 3.8 (a).

The maximum peak response of 6.5 A/W at 7.1 THz (42 μm) was obtained at 0.7 kV/cm bias field. A strong light reflection occurs around 11 THz (27 μm) and 8.3 THz (36 μm) due to the AlAs-*like* and GaAs optical phonons, giving two minima around 11 THz (27 μm) and 8.3 THz (36 μm) in the responsivity spectra [see Fig. 3.8 (a)]. Up to now, the lowest threshold frequency reported for HEIWIP detectors is 2.3 THz (128 μm)[5]. It is noteworthy that the response of the single emitter detector matches the 10 emitter layer p-type detector reported previously [5]. The peak values of responsivity (R_{peak}), quantum efficiency (η_{peak}), and detectivity (D^*_{peak}) at 7.1 and 10.4 THz for different bias fields are given in Table 3.1.

The detectivity was calculated using the shot noise. The device response decreases with temperature and vanishes after 25 K. The variation of R_{peak} values at 7.1 and 10.4 THz with temperature under 0.7 kV/cm bias is shown in Fig. 3.8 (b) while the peak response variation with applied field at 6 K is shown in Fig. 3.8 (c). The device can be operated under reverse bias also and R_{peak} values of 1.7, 1.1, and 0.7 A/W at 10 THz (30 μm) were observed at -0.25, -0.5, and -0.75 kV/cm bias, respectively. The spectral response obtained experimentally for the multi emitter is shown in Fig. 3.9 and the threshold frequency of $\sim$ 5 THz (60 μm) was obtained under electric fields of 1 - 3 kV/cm. A slight variation from 4.8 - 5.3 THz (20 - 22 meV) in the threshold frequency can be seen with the applied fields and can be a result of different barrier lowering values under different applied fields. Arrhenius analysis (see Fig. 3.6 (b)) gives a workfunction varying from 18 - 25 meV (68 - 50 μm) with different applied bias fields, where the threshold frequencies obtained experimentally are within this range.

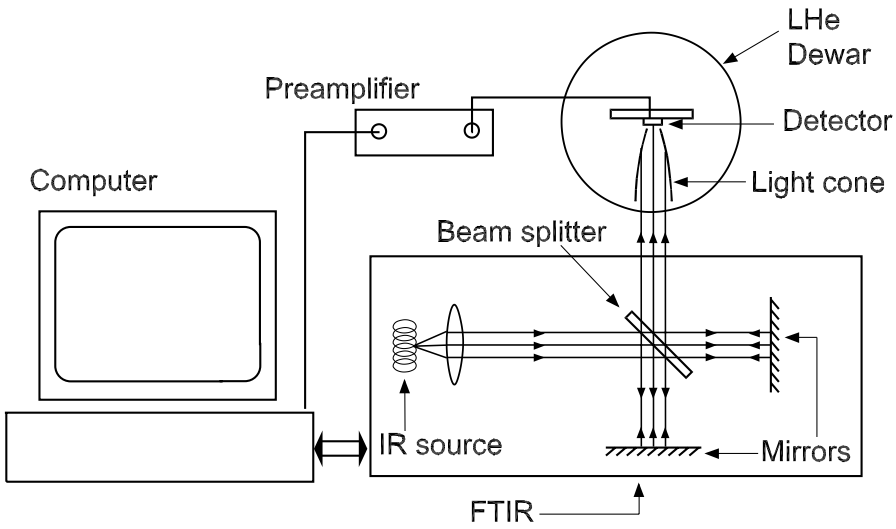

Figure 3.7: The experimental setup used to measure the photoresponsivity. A Perkin Elmer System 2000 FTIR spectrometer is primarily used to measure the spectral response of the detector. The detector is mounted on the liquid He cooled dewar, and the detector output signal is fed to the computer through the preamplifier.

In the multi emitter detector, the calculated workfunction (Δ) would be $\sim$ 83 meV (20 THz or $\sim$ 15 μm) after considering bandgap narrowing [73], Δ_{narr} = 35 meV, Δ_x = 103 meV, and the E_F = 55 meV. It is clear the calculated workfunction (Δ) does not agree with the workfunction (Δ) obtained experimentally. According to the SIMS data (see Fig. 3.5 (b)), there is a dopant (Si) migration into the AlGaAs barrier layers in the growth directions leaving a small part (20 - 30 nm) of the AlGaAs barrier unintentionally n - type doped. However, these free carriers in AlGaAs barrier will spill into the adjacent GaAs well since the conduction band of AlGaAs is higher than the conduction band of the GaAs well, creating a dipole on the interface [74]. This interface dipole can reduce the effective barrier height by $e\Delta\phi$. Here, e is the electron charge, $\Delta\phi$ is the electric potential due to the surface dipole and is given by $\Delta\phi = (\sigma/\varepsilon)d$, where σ is the surface charge density on the interface and is given by $\sigma = eNt$, where N is the migrated dopant concentration and t is thickness of the diffusion layer. ε is the static dielectric constant of the material, and d is the thickness of the depleted layer. Because of this surface dipole, the threshold frequency of the multi emitter device can decrease drastically. If the average migrated doping concentration N is considered to be $\sim 5\times10^{16}$ cm^{-3} over a 25 nm thickness, then $\Delta\phi$ will be $\sim$ 52 meV. Therefore, the modified workfunction (Δ) can be reduced to $\sim$ 31 meV. In addition, the bandgap lowering ($\Delta\phi_b$) under an external applied field (which can be calculated by using $\Delta\phi_b = q\sqrt{qE/4\pi\varepsilon}$), and will be 5 - 7 meV under an electric filed of 3 - 4 kV/cm. Therefore, the modified workfunction (Δ) will be $\sim$ 25 meV which can produce a threshold wavelength of 50 μm (6 THz) which is comparable with the experimentally obtained threshold for the multilayer device. Note that due to the surface dipole, an extra triangular potential barrier

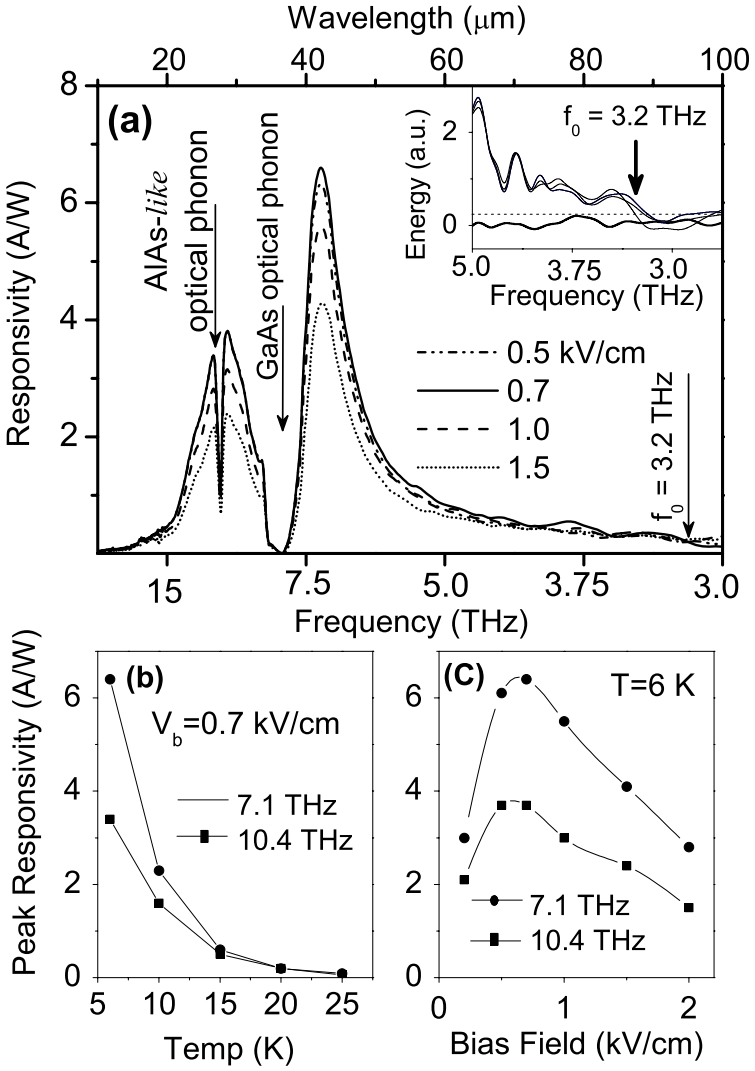

Figure 3.8: (a) Responsivity variation with applied electric field in forward bias (photoemission from bottom contact) is shown. The highest responsivity is 6.5 A/W at 0.7 kV/cm at 6 K. The threshold frequency which is determined by the instrument noise level is 3.2 THz and is shown in the inset. The dotted line represents the maximum noise level. (b) The variations of R_{peak} at 7.1 and 10.4 THz with temperature under the applied electric field of 0.7 kV/cm. The responsivity vanishes above 25 K. (c) Variations of peak responsivity at 7.1 and 10.4 THz under different bias fields.

Table 3.1: The responsivity (R_{peak}), the quantum efficiency (η_{peak}), and the detectivity (D^*_{peak}) at 7.1 and 10.4 THz frequencies for different bias fields. The maximum peak responsivity occurs at 0.7 kV/cm. The uncertainty of R_{peak}, η_{peak}, and D^*_{peak} are less than ± 5 %.

	Peak at 7.1 THz			Peak at 10.4 THz		
Bias Field	R_{peak}	η_{peak}	D^*_{peak}	R_{peak}	η_{peak}	D^*_{peak}
(kV/cm)	(A/W)	(%)	($\times 10^8$ Jones)	(A/W)	(%)	($\times 10^8$ Jones)
0.2	3.0	8.9	5.5	2.1	9.1	3.8
0.5	6.1	18.2	6.4	3.7	16.4	3.8
0.7	6.5	18.9	5.5	3.7	16.4	3.1
1.0	5.5	16.5	3.4	3.1	13.5	2.1
1.5	4.1	12.3	2.1	2.4	10.3	1.2

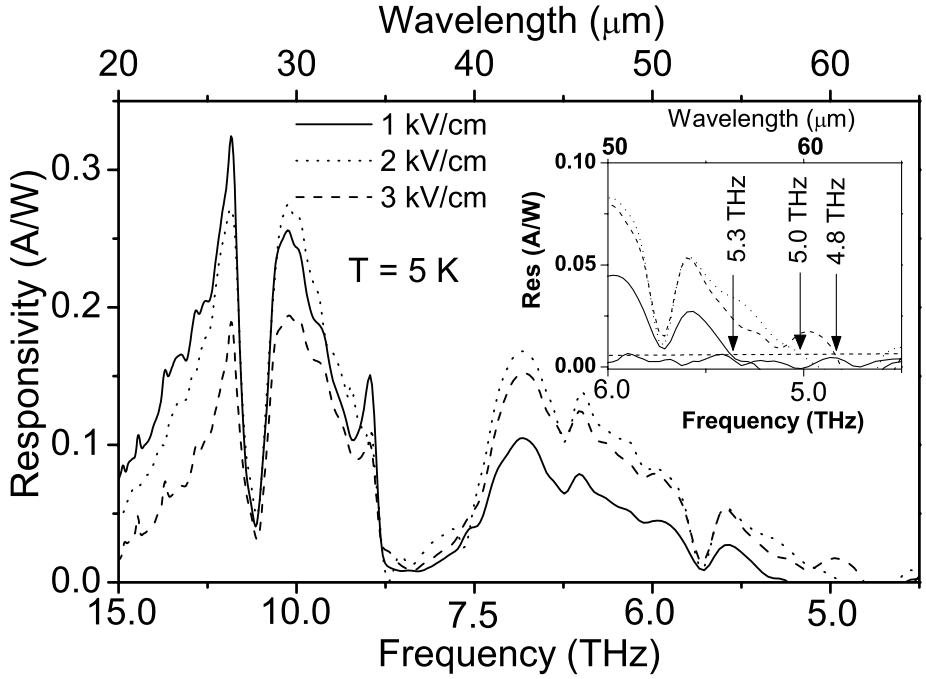

Figure 3.9: The responsivity of a multiemitter device with three different applied bias fields at 5 K . The maximum responsivity is 0.32 A/W at 11 THz for the bias field of 1 kV/cm. Threshold frequencies of 5.3, 5.0, and 4.8 THz were estimated for bias fields of 1.25, 2.5, and 3.75 kV/cm, respectively, using the system noise level as shown in the inset. The horizontal dashed line shows the maximum noise level.

occurs. However, electrons can tunnel through this barrier [74] since the thickness of the extra barrier is only a few atomic layers. In addition, the photoresponsivity can be reduced due to the smaller effective emitter thickness resulting from the dopant migration.

3.3.2 Photoresponse modeling

a. Photoemission efficiency without phonon emission

The photoemission efficiency over the barrier can be calculated as described in Section 3.2. In the photoemission calculations, energy independent scattering lengths were assumed. The phonon emission; i.e., the energy loss from photoexcited electrons due to scattering with a phonon $(e-p)$, was also ignored in the initial calculation. Thereafter, the total quantum efficiency η was calculated as discussed in Section 3.2. The average electric field component (used in Eq. 3.2) of the propagating light inside the emitter was calculated by using the matrix method given in section 2.1.4. The dielectric function, which is needed to calculate η_a is given by

$$\varepsilon(\omega) = \varepsilon_\infty(1 - \frac{\omega_p^2}{\omega^2 + i\omega\gamma}) + \sum_{j=1}^{n} \frac{S_j\omega_j^2}{\omega_j^2 - \omega^2 - i\Gamma_j\omega}, \tag{3.19}$$

where ε_∞, ω_p, and ω_j are the high frequency dielectric constant, the plasma frequency, and the optical phonon frequencies, respectively. S_j, Γ_j, and γ are the optical phonon strengths, the optical phonon broadening constant, and the plasma oscillator damping constant, respectively. n is the number of optical phonons. In this case it is two; GaAs E_1 and AlAs-like E_1 phonons.

b. Responsivity modeling with phonon emission

The photoexcited electrons with energy more than the phonon energy of the emitter mate-

rial can possibly transfer energy to the lattice by electron - phonon $(e-p)$ scattering if the emitter thickness is much larger than the $e-p$ scattering length. This process will reduce the photoemission efficiency. The photoemission efficiency of photoexcited electrons after the first phonon emission [67] can be given by Eq. 3.20. Note that in this model calculation, the second phonon emission is neglected since the required energy for the second phonon emission is $\sim$ 70 meV where the detector spectral response is inherently weak.

$$\eta_{em} = \eta_0 + \eta_1(1 - \frac{\eta_0}{\eta_\infty^{'}})\gamma, \tag{3.20}$$

where η_0 is the fraction of electron emitted over the barrier without undergoing the phonon emission and is given by Eq. 3.11 and $\eta_\infty^{'}$ is the fraction of potentially capturable photoexcited electrons after the the first phonon emission and will be given later. $\gamma = \frac{L_e}{L_e+L_p}$. η_1 is given by Eq. 3.21

$$\eta_1 = \frac{L^*}{W_d}\{1 - exp(\frac{-W_d}{L^*})\}\eta_{idle}^{'}, \tag{3.21}$$

Here, L* depends on the $e-e$ and $e-p$ scattering lengths [67] and is given in $\frac{1}{L^*} = \frac{1}{L_e} + \frac{1}{L_p}$. W_d is the emitter thickness. $\eta_{idle}^{'}$ is the ideal quantum efficiency of the photoexcited electrons that go over the barrier after the first phonon emission and can be calculated as follows,

$$\eta_{idle}^{'} = \frac{N^{'}}{N_T^{'}}, \tag{3.22}$$

where $N^{'}$ is the number of photoexcited electrons that go over the barrier after the first phonon emission and $N_T^{'}$ is the number of photoexcited carriers excited by incident photons with energy > phonon energy. At low temperature,

$$N^{'} = \int_{max(E_F+\Delta+E_{phn},h\nu)}^{E_F+h\nu} \frac{dN}{dE} f(E)dE, \tag{3.23}$$

and,

$$N_T^{'} = \int_{max(E_F,h\nu)}^{E_F+h\nu} \frac{dN}{dE} dE, \tag{3.24}$$

where $h\nu$ is the incident photon energy, E_F is the Fermi energy level in the emitter, Δ is barrier height, E_{phn} is the phonon energy, and dN/dE is the density of states which is approximately proportional to $E^{1/2}$. $f(E)$ is defined by the escape cone velocity (given in eq. 3.5).

$\eta_{\infty}^{'}$ is defined as follows,

$$\eta_{\infty}^{'} = \frac{N_M^{'}}{N_T^{'}}, \tag{3.25}$$

and,

$$N_M^{'} = \int_{max(E_F+\Delta+E_{phn},h\nu)}^{E_F+h\nu} \frac{dN}{dE} dE, \tag{3.26}$$

Finally, the photoemission efficiency η_{em} can be calculated after $\eta_{idle}^{'}$ and $\eta_{\infty}^{'}$, and η_1 are calculated separately for the following three scenarios.

(*a*) $h\nu > \Delta + E_{phn}$ and $h\nu <= E_F + E_{phn}$

(*b*) $h\nu > E_F + E_{phn}$ and $h\nu <= E_F + \Delta + E_{phn}$

(*c*) $h\nu > E_F + \Delta + E_{phn}$

Note that all photons which have energy more than phonon energy do not necessarily excite electrons which have excited energies more than phonon energy because of depending on where the photon is absorbed in the Fermi sea. This probability should also be taken into account in the calculation.

c. Single emitter device response modeling

The single emitter detector photoresponse in the forward and the reverse bias operations is shown in Fig. 3.10 (a). When the detector is in the forward bias, the photoresponse is

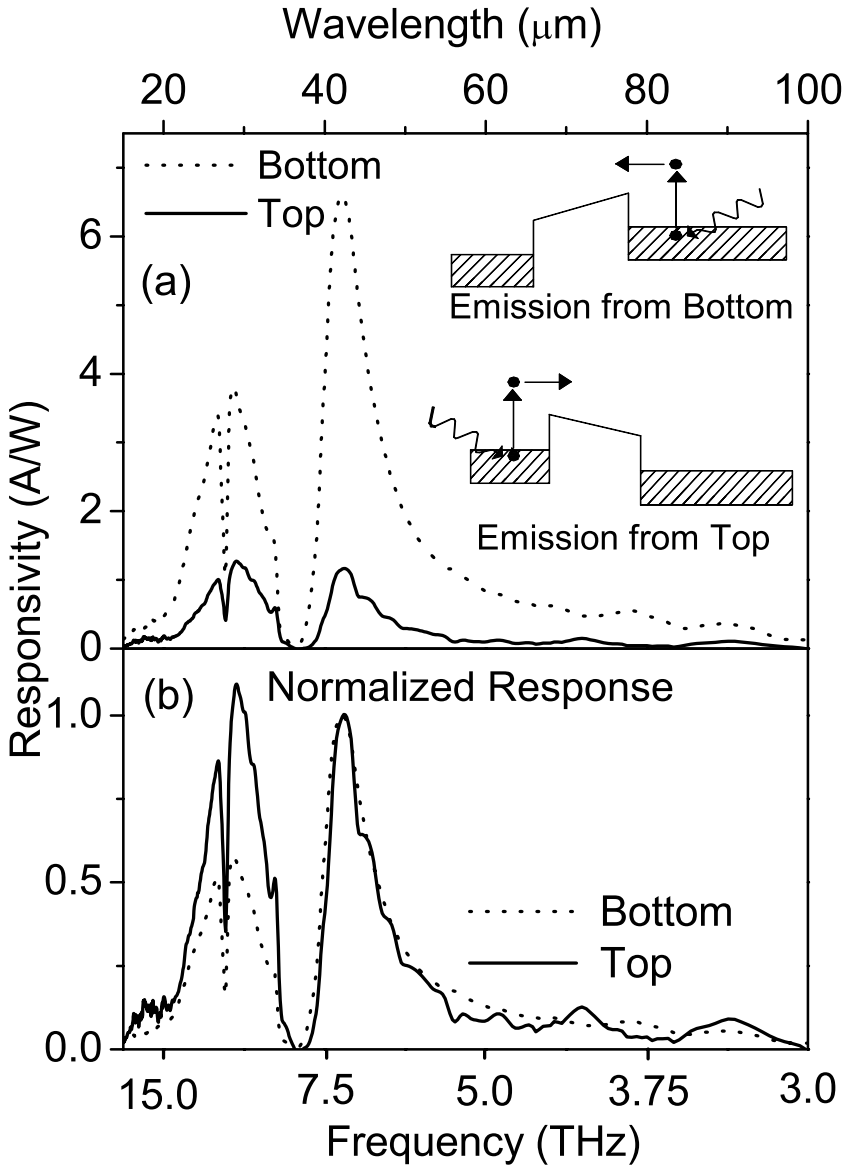

Figure 3.10: (a) Experimental forward and reverse bias responses. The peak responsivity of 6.5 A/W for forward bias is at 7.1 THz (bottom contact layer - dotted line) while 1.2 A/W for reversed bias is at 10 THz (Top contact layer - Solid line). This is due to the higher photoabsorption efficiency in the bottom contact that is thicker. Photoemission is from the bottom contact in the forward bias operation while photoemission is from the top contact in reverse bias operation as shown in the inset. (b) The normalized forward and reverse bias spectra. Although the two spectra match below 8 THz, the amplitudes do not match above 8 THz giving evidence for the low efficiency in the bottom contact.

from the bottom contact layer, whereas, the photoresponse is from the top contact layer when the detector is in the reverse bias. The responsivity from the bottom contact layer is higher than that of the top contact layer. The reason for this large difference is the higher photoabsorption (see Fig. 3.11) in the bottom contact layer since the bottom contact layer is much thicker than the top contact layer. This was confirmed by calculations. The highest photoresponse efficiency in the top contact layer occurs around 30 THz while the highest photoresponse efficiency in the bottom contact layer occurs at 7.1 THz. It is not expected that the characteristics (except the amplitudes) of two responsivity spectra from the bottom and the top contact layer are different as the detector design is almost symmetric. Specifically, the doping concentrations are the same in the top and the bottom contact layers as shown in the SIMS results (Fig. 3.5 (a)). When the two responsivities are normalized (see Fig. 3.10 (b)), a clear difference between the two responsivity spectra can be seen. The photoresponse efficiency from the bottom contact layer is considerably smaller than that of the top contact layer in the spectral range above 8 THz. This may be due to the phonon emission by photoexcited carriers. Therefore, the photoresponsivity modeling was carried out with and without taking phonon emission into account and compared the results with experimental results.

The calculated photoabsorption spectra due to the free carriers are shown in Fig. 3.11 for both the top and the bottom contact layers and both shapes are the same as expected. The highest absorption occurs at 7.6 THz (40 μm) in both the top and the bottom contact layers. The bottom contact layer absorption is higher than that of the top contact layer because the thickness of the bottom contact layer is larger and this explains

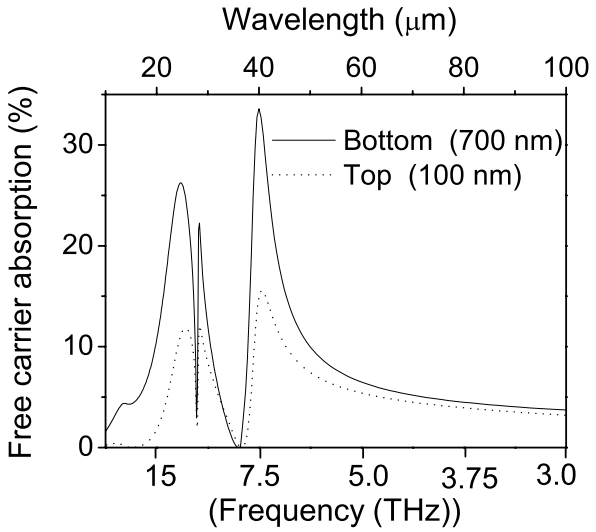

Figure 3.11: The calculated free carrier absorption probabilities in the top and the bottom contact layers for the structure. The highest absorption occurs at 40 μm in both layers.

why the bottom contact photoresponse is higher.

The calculated responsivities without considering phonon emission, for the bottom contact layer and the top contact layers, are shown in Fig. 3.12 (a) and (c). While the model and experimental responsivity agree well for the top contact layer as shown in Fig. 3.12 (c), the experimental responsivity for the bottom contact layer does not agree with the model responsivity as seen in Fig. 3.12 (a) in the region above 10 THz. The experimental responsivity in the higher frequency region (>10 THz) is much smaller than the model responsivity. A better agreement is found only in the frequency region below 10 THz (>30 μm). This low photoresponse efficiency region lies above the GaAs optical phonon, $E_1(TO)$ (33 meV). Therefore, the reason for the lower photoresponse than expected may be due to phonon emission by photoexcited electrons. Since the thickness of the top contact layer is much smaller, the effect of the phonon emission on the top contact responsivity should be minimal. Furthermore, the responsivity from the bottom contact was modeled by taking energy loss due to phonon emission into account as described in Section 3.3.2 (b). The calculated and experimental spectra are shown in Fig. 3.12 (b). Although, the calculated photoresponse above 10 THz is still higher than that for the experimental spectra, the difference has decreased by 30 - 40 % in that region. The electron-phonon ($e-p$) scattering length and electron-electron ($e-e$) scattering length are assumed to be 20 nm and 400 nm, respectively. An additional process, which is not yet understood, can be responsible for this discrepancy. In addition, the energy dependent scattering lengths can also be a reason.

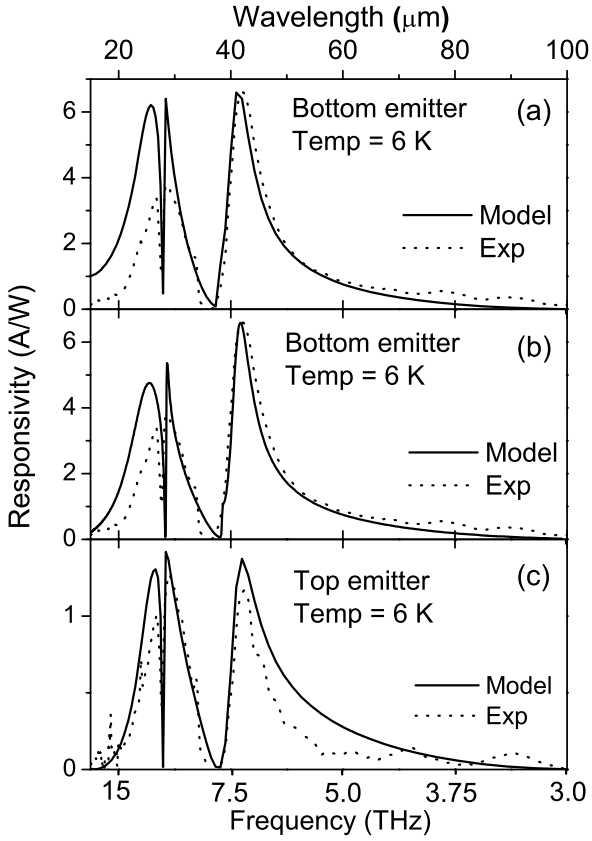

Figure 3.12: The model calculation and the experimental photoresponse spectra of the single emitter device. (a) The bottom contact photoresponse modeling for the single barrier without phonon emission taken into account. Considerable difference can be seen between the calculated and experimental spectra above 8.0 THz. (b) The bottom contact photoresponse modeling for the single barrier with phonon emission taken into account. The difference between experimental and calculated spectra above 8.0 THz has decreased but there is still a discrepancy which can be due to the assumption of energy independent scattering lengths in the calculations (c) Photoresponse modeling of the top contact without phonon emission taken into account. The calculated and experimental spectra match reasonably well. There is a small difference around 5.0 THz but this difference is much smaller compared to the difference in the bottom contact response in (a).

3.4 GaN and InN based material system for terahertz detection

One potential way to improve terahertz detection is to investigate new materials systems for detectors. GaN and InN are relatively new materials as the semiconductor technology is concerned and the later one is the newest one of the two materials. In this part, the possibilities of using GaN (or GaMnN) and InN as terahertz detectors will be discussed. Since optical properties of GaN and GaMnN with low Mn concentration do not differ considerably, only GaN material will be used in the discussion. However, infrared absorption can be enhanced greatly in HEIWIP structures using Mn as magnetically active imbedded nanocomposites (MAINs) in GaN [75]. GaN/AlGaN material systems will be compared to GaAs/AlGaAs material systems which have been thoroughly studied before.

3.4.1 Comparison of terahertz absorption in GaN and GaAs

The free carrier absorption characteristics of materials is an important consideration for terahertz detectors based on HEIWIP mechanism. The absorption coefficient of bulk GaAs is higher than that of bulk GaN in the infrared and terahertz region [see Fig. **??** (a)]. However, the free carrier absorption in GaN thin film grown on sapphire substrate is more interesting when compared with absorption in GaAs thin films grown on GaAs substrates. The GaN/Sapphire structure can be engineered to have a better absorption in terahertz region as evident in Fig. **??** (b) which shows the terahertz absorption in 1×10^{18} cm^{-3} n-doped 1 μm thick GaAs grown on a GaAs substrate and 1×10^{18} cm^{-3} n-doped 1 μm thick GaN grown on a sapphire substrate. In the range below 50 μm, the absorp-

tion is better in GaAs and the maximum absorption occurs around 30 μm, however the restrahlen region of GaAs occurs between 33 - 36 μm affecting the IR absorption in this range. Therefore, one disadvantage of GaAs/AlGaAs material system as an IR detector is that the restrahlen region occurs inside the maximum IR absorption region. Above 50 μm, the light absorption is higher in n-doped GaN when compared to n-doped GaAs. The reason for this higher light absorption in GaN film is due to the GaN/Sapphire interface. Higher terahertz light reflection occurs on the GaN/Sapphire interface leading to higher light absorption in the doped GaN layer. Therefore, the GaN/Sapphire material system can be effectively used for terahertz detection.

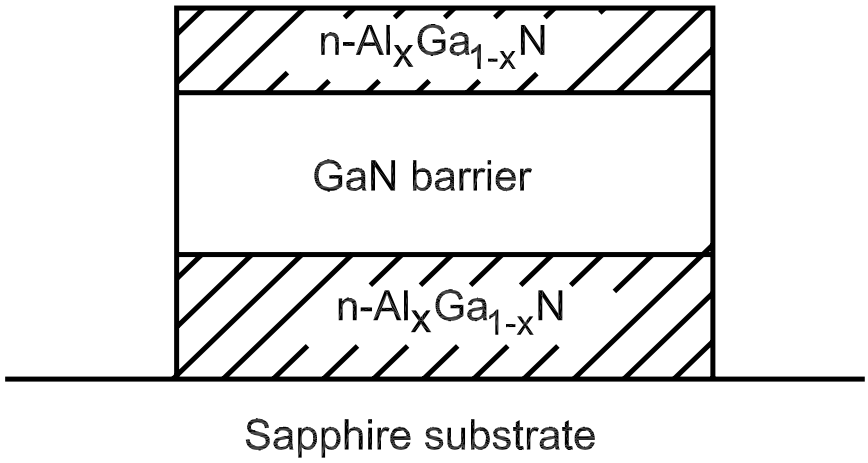

Figure 3.14: The $Al_{0.007}Ga_{0.993}N$/GaN terahertz detector structure. The $1\times\ 10^{18}$ cm^{-3} n - type doped $Al_{0.007}Ga_{0.993}N$ layer is used as the emitter (top and bottom contacts) while 1 μm thick undoped GaN used as the barrier. The top and the bottom contact layer thicknesses are 400 and 700 nm respectively.

3.4.2 A possible GaN/AlGaN HEIWIP terahertz detector

An $Al_xGa_{1-x}N$/GaN/ $Al_xGa_{1-x}N$/Sapphire structure shown in Fig. 3.14 is proposed as a possible terahertz detector with an 1 THz (300 μm) threshold frequency, where a 4.1 meV workfunction is required. Here, the GaN layer acts as the barrier layer while two $Al_xGa_{1-x}N$ layers will act as the top and the bottom emitter layers (see Fig. 3.14). $Al_xGa_{1-x}N$ should be considered for emitters for the following reason. If $Al_xGa_{1-x}N$ is used as the barrier and GaN is as the emitter as in the case of GaAs/AlGaAs HEIWIP, then the smallest workfunction (Δ) that can be obtained is about 18 meV with the emitter doping of $n = 1\times10^{18}$ cm^{-3} as the Al fraction (x) goes to the zero limit. The corresponding threshold frequency is 4.3 THz ($\sim$ 70 μm). This 18 meV band offset arises from the band gap narrowing (Δ_{narr}) in the conduction band due the doping and is 36 meV for 1×10^{18} cm^{-3} n-type doping, which can be calculated using high density theory [73]. The Fermi energy (E_F) in the emitter will be $\sim$ 18 meV due to the 1×10^{18} cm^{-3} n-type doping. Therefore, the workfunction ($\Delta = \Delta_x+\Delta_{narr}-E_F$) as explained in Section 3.2 will be $\sim$ 18 meV. Δ_x is assumed to be negligible as the Al fraction (x) goes to zero. Therefore the smallest possible workfunction is about 18 meV. However, it is not favorable to reduce the emitter doping level since it will reduce the free carrier absorption efficiency. Reducing the workfunction (Δ) further is not possible if $Al_xGa_{1-x}N$ is used as the barrier. However, this obstacle can be overcome using GaN as the barrier and n - type doped $Al_xGa_{1-x}N$ as the emitters. A structure of 1×10^{18} cm^{-3} n-type doped $Al_{0.007}Ga_{0.993}N$ layer as the emitter and undoped GaN as the barrier will have a workfunction of $\sim$ 4 meV giving an $\sim$ 1 THz threshold frequency ($\sim$ 300 μm). The band alignment of $Al_xGa_{1-x}N$/GaN heterostructure

before and after doping is shown in Fig. 3.15. The conduction band offset (Δ_x) due to the Al fraction (x) is calculated by assuming the conduction band offset changes with x as ΔE_c = 2000×x in meV [76]. The Δ_x for x = 0.007 is about 14 meV and Δ_{narr} is 36 meV for 1×10^{18} cm^{-3} n-type doping [73]. Note that the band gap narrowing of $Al_{0.007}Ga_{0.993}N$ is assumed to be same as that of GaN due to the low x value. The Fermi energy E_F is 18 meV for 1×10^{18} cm^{-3} n-type doping. Now, the workfunction is calculated by using $\Delta = \Delta_{narr}$-Δ_x-E_F and is $\sim$ 4 meV which corresponds to $\sim$ 1 THz.

Therefore, the possible terahertz detector will be an undoped 1 μm thick GaN layer sandwiched between 1×10^{18} cm^{-3} n-type doped $Al_{0.006}Ga_{0.994}N$ layers grown on sapphire substrate as shown in Fig. 3.14. The doped $Al_{0.006}Ga_{0.994}N$ layers serve as the top and the bottom contact layers as well. The calculated photoresponse is shown in Fig. 3.16 along with a calculated photoresponse for a similar type GaAs detector. It can be clearly seen that photoresponse of an AlGaAs/GaN detector is about a factor of three higher than the that of GaAs/AlGaAs detector. The reason for the higher photoresponse is due to two factors. The first one is the higher photoabsorption (η_a) in $Al_xGa_{1-x}N$ emitter grown on Sapphire substrate as explained earlier. The second reason is the higher photoexited carrier emission efficiency η_e in the $Al_xGa_{1-x}N$/GaN heterostructure due to the higher effective mass of electrons in GaN ($Al_xGa_{1-x}N$). The effective mass is $0.2m_0$ in GaN while it is $0.067m_0$ in GaAs. Therefore, the photo emission efficiency (η_e) is much higher. Finally it can be concluded that the $Al_xGa_{1-x}N$/GaN heterostructure grown on Sapphire can be used as a potential terahertz detector.

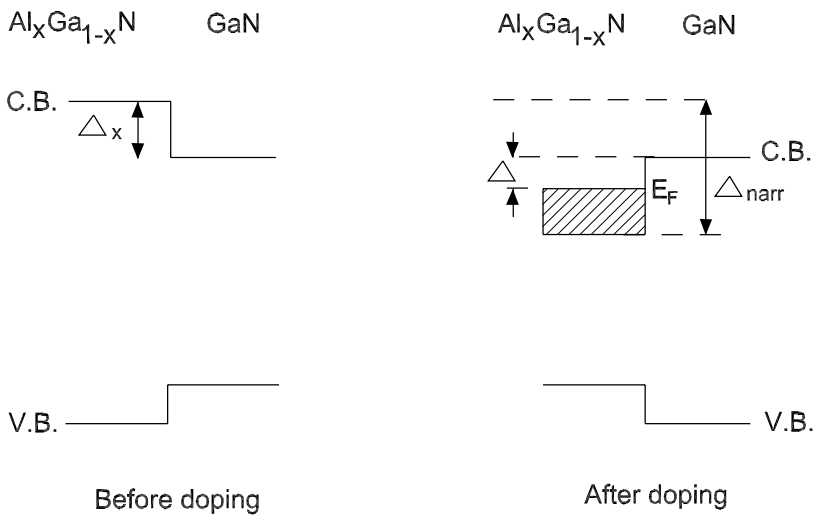

Figure 3.15: The conduction band (C.B.) and the valence band (V.B.) alignments of $Al_xGa_{1-x}N/GaN$ heterostructure before doping and after doping. $Al_xGa_{1-x}N$ is used as the doped emitter. Before doping, the band offset is due to the Al fraction and is Δ_x. After n - type doping, the band gap narrowing is Δ_{narr} in the C.B. and the Fermi energy is E_F. The workfunction (Δ) is given by Δ_{narr}-Δ_x-E_F in this case.

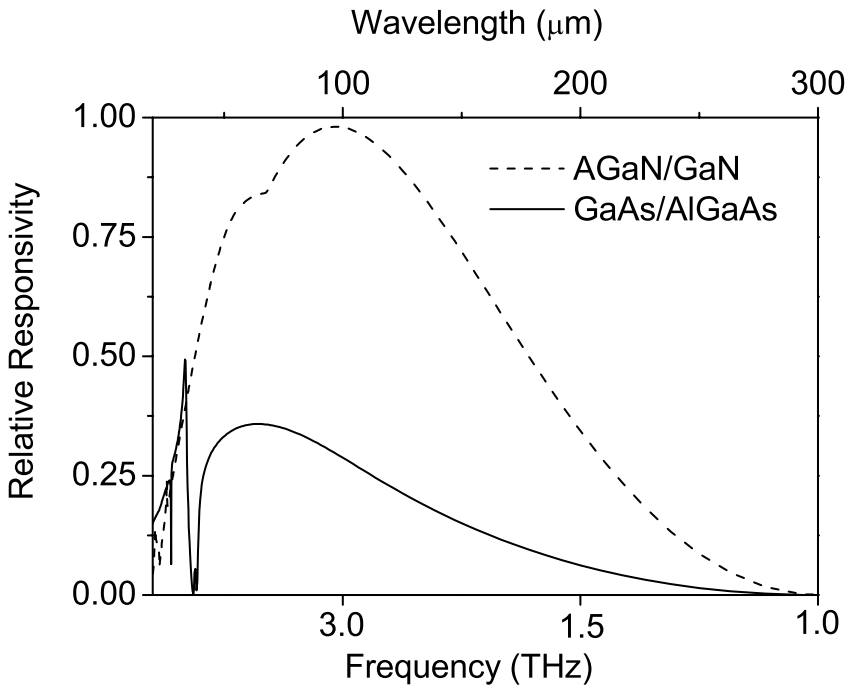

Figure 3.16: A relative photoresponse comparison of AlGaN/GaN and GaAs/AlGaAs terahertz detectors. The photoresponse of AlGaAs/GaN detector is about a factor of three higher than the GaAs/AlGaAs photoresponse. The peak response of AlGaN/GaN detector occurs around 3 THz while the peak response of GaAs/AlGaAs occurs around 6 THz. Therefore, a GaN based HEIWIP is a better option for FIR/terahertz detection.

3.4.3 Possibilities of InN as a new material for terahertz detectors

The free carrier absorption coefficient and light absorption in InN can be studied as a starting point for using InN in a terahertz detector, and Fig. 3.17 shows the absorption variation for 5×10^{17} cm^{-3}, 1×10^{18} cm^{-3}, and 2×10^{18} cm^{-3} n -type dopings in 1 μm thick InN layer grown on a Sapphire substrate. The inset of Fig. 3.17 shows the calculated absorption coefficient, which is comparable with that of GaAs. The optimum free carrier absorption occurs around 1×10^{18} cm^{-3}. As the doping concentration increases, the terahertz absorption decreases due to the higher plasma frequency. At present our knowledge about the band gap narrowing in InN with doping and InN band offsets with other materials such as InGaN and InAlN is not well established, so designing an InN based detector may be premature. As mentioned earlier, the band gap offset of InN/GaN material system can be engineered for spectral response over a large spectral region. This flexibility will favor many future opto-electronic applications.

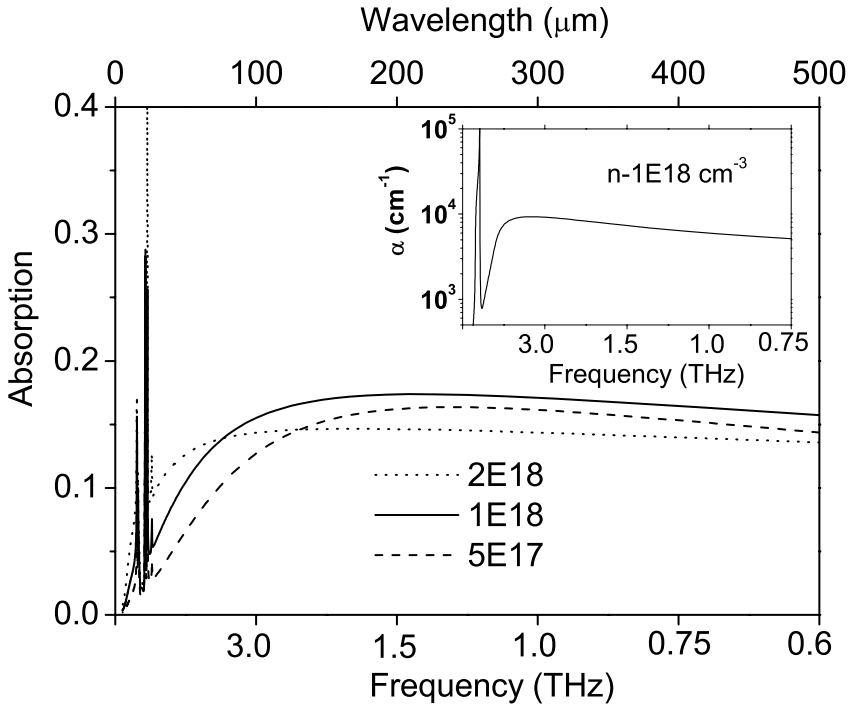

Figure 3.17: The free carrier absorption variation in a 1 μm thick InN layer grown on a sapphire substrate for 5×10^{17} cm^{-3}, 2×10^{18} cm^{-3}, and 2×10^{18} cm^{-3} n - type dopings. The inset shows the calculated absorption coefficient of InN with a doping of 1×10^{18} cm^{-3} and is comparable to GaAs. As a whole, the terahertz absorption stays constant below 3.0 THz

3.5 Conclusion

In this work, an n-type GaAs/AlGaAs HEIWIP THz detector has been successfully demonstrated. When compared with p-type HEIWIP detectors, a smaller threshold frequency can be obtained with a relatively higher Al fraction. Thereby, n-type HEIWIP devices could pass threshold frequencies reported for p-type HEIWIP detectors[12]. An Al fraction of 0.005, which is around the lowest limit for MBE, was used to obtain a 3.2 THz threshold in a p-type HEIWIP detector[12] while the same threshold frequency can be obtained with an Al fraction of 0.04 in the n-type HEIWIP detector as shown in this study. Extending the threshold frequency below 3 THz in n - type HEIWIP detectors is possible. A smaller work function can be designed with a relatively higher Al fraction compared to the case of a p-type HEIWIP detector. HEIWIP detectors based on n -type GaN could be a good candidate for terahertz detection.

Chapter 4

Terahertz Emission Using GaN and Terahertz Effect on the Nerve Cell Growth

4.1 Terahertz emitters using bulk GaN

Today high efficient terahertz sources are in demand for new terahertz technologies such as communication, spectroscopy, radar, and imaging. The popular terahertz sources [77] are the free electron laser and the quantum cascade laser, which are too expensive for most terahertz applications and experiments. The technologies used for radiation sources in the regions bordering the terahertz range, the IR region and the millimeter and microwave region, can not be adopted successfully into the terahertz region since the radiation generation efficiency decreases rapidly [78]. Therefore, new methods and ideas are being proposed for terahertz sources, and terahertz emission in bulk GaN [77] and InN [79], which is based on the

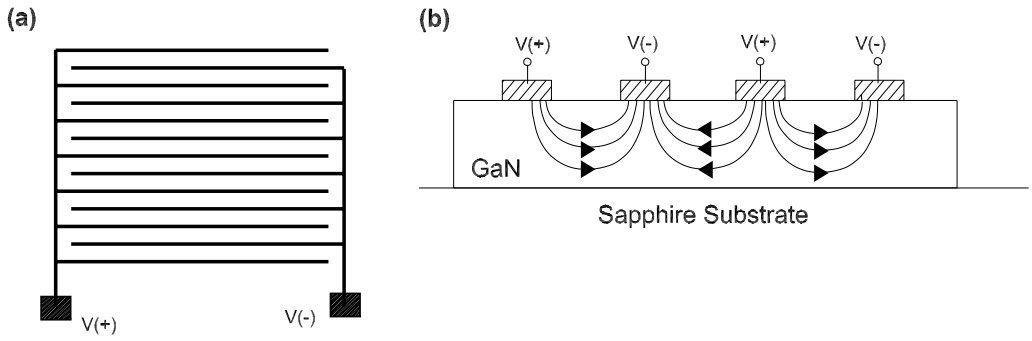

Figure 4.1: (a) The schematic diagram of an interdigitated pattern. Electric fields on the order of few kV/cm can be obtained by applying a few volts between V(+) and V(-) since the finger spacing is on the order of few micrometers. The active surface area can be increased by laying several of these patterns. (b) The the cross section of GaN with interdigitated contacts. Electric fields form inside a GaN layer from positive pole to negative pole as shown with field lines.

excitation of coherent electron plasma oscillation by optical phonon emission, and it is interesting since it is based on a simple technique. According to the theoretical studies [77, 79], bulk GaN and InN can generate terahertz radiation under an electric field of a few kV/cm. In this study, an attempt was made to test the theoretical predictions. An intrinsic 1 μm thick GaN film grown on sapphire substrate was processed and interdigitated gold metal contacts were laid on the GaN film so that the required electric filed could be achieved and a larger surface area could be covered in order to obtain the maximum radiation output power. A schematic diagram of the top view of interdigitated contacts is shown in Fig 4.1 (a). Space between contacts (finger space) could be a few tens of micrometers. Electric field formation across the inside the structure is shown in Fig. 4.1 (b). The processed GaN film is shown in Fig. 4.2 with two different inderdigitated patterns with contact separations of 20 μm. With these contact separations, electric fields on the order of a few kV/cm can be easily obtained by applying D.C. voltages of 10 - 20 V.The testing of the terahertz emission from this GaN sample under D.C. bias at room temperature was carried out using a FTIR spectrometer with TGS detector as shown in Fig. 4.3. The GaN terahertz emitter acts as the light source for the FTIR. The advantage of this setup with the FTIR is the ability to detect even weak spectra by taking average of a several hundreds of spectra. Due to the 300 K background radiation, a spectrum can be seen even under the zero electric field and is called background spectrum. First, the background spectra were collected under zero applied electric field. After that, the applied electric field was gradually increased and corresponding spectra, which are shown in Fig. 4.4, were taken under different applied electric fields.

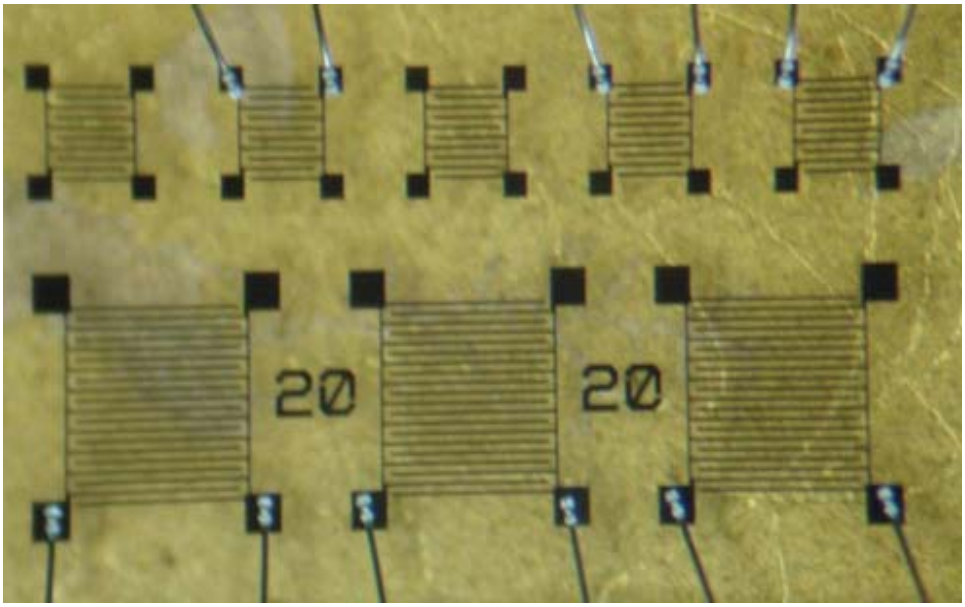

Figure 4.2: The actual photograph of the interdigitated contacts with the finger separation of 20 μm, laid on an intrinsic 1 μm thick GaN film grown on sapphire substrate. The darker horizontal lines are the metal interdigitated contacts. Maximum surface area coverage and electric fields on the order of kV/cm can be achieved using interdigitated contacts.

4.2 Discussion

Up to 5 kV/cm, there is no apparent difference between the background and the emission spectra as seen in Fig. 4.4 (a), (b), and (c). The background spectrum is a result of the 300 K background radiation and the two minima between 15 and 30 THz occur due to the FTIR beamsplitter (6 μm Mylar film). Note that the 300 K background spectra have been affected by the optical components in the FTIR. For electric fields above 5.0 kV/cm, a clear difference between the background and emission spectra can be seen from 5 to 10 THz as seen in Fig. 4.4 (d), (e), and (f). The radiation change due to any thermal heating in GaN can be ruled out since there is no difference between the background and the emission spectra in the high frequency region (>15 THz). Therefore, the difference seen between the background and the emission spectra in the range of 5 - 10 THz can be considered as the terahertz emission from GaN as predicted theoretically [77]. Furthermore, emission spectra divided by the background for 5.5, 6.0, and 6.5 kV/cm are shown in Fig. 4.5. The low input power requirement (compared to blackbody radiation sources) and smaller physical size are the advantages of this type of source. In the future studies, the optimization of the terahertz emission using optical waveguides and different GaN structure designs should be studied.

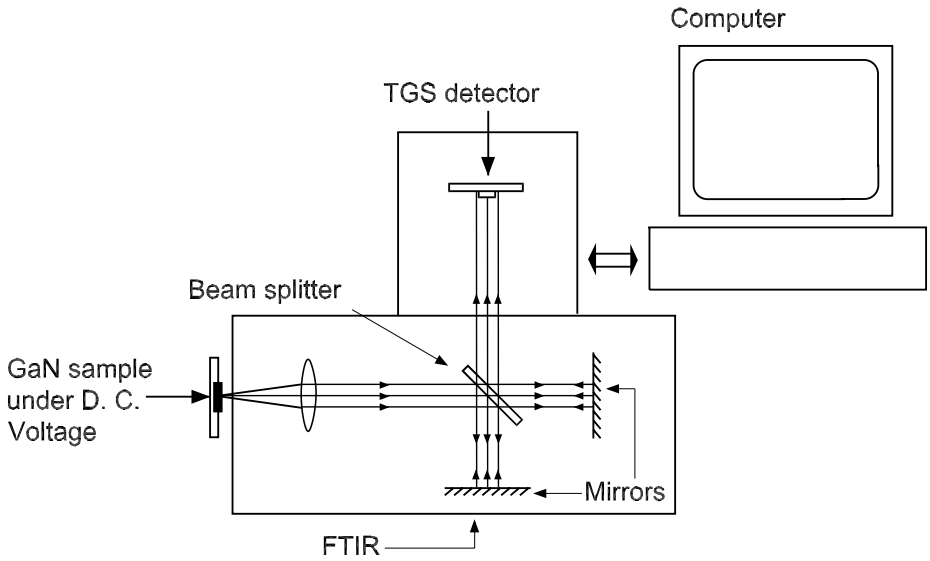

Figure 4.3: The experimental setup used to test the terahertz emission from bulk GaN under D.C. electric field. The FTIR spectrometer with a TGS detector was used. The terahertz emitter (GaN) was used as the external light source for the FTIR spectrometer.

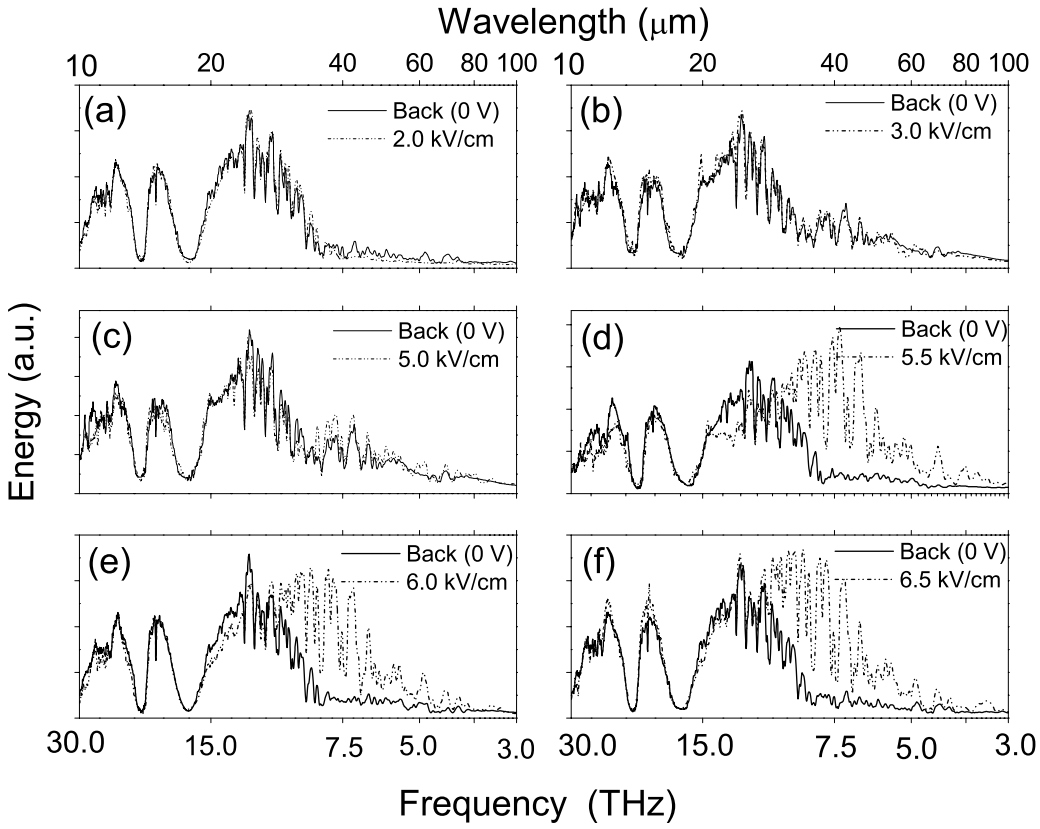

Figure 4.4: The background spectra (under zero electric field) and GaN emission spectra under different electric fields. In (a), (b), and (c), no apparent difference between the background and the emission spectra can be seen suggesting no emission under 5 kV/cm fields. For fields higher than 5 kV/cm, a difference in 5 - 10 THz between the two spectra can be seen giving evidence for terahertz emission from GaN. Radiation due to thermal heating under the constant electric field can be ruled out since there is no change in the high frequency region.

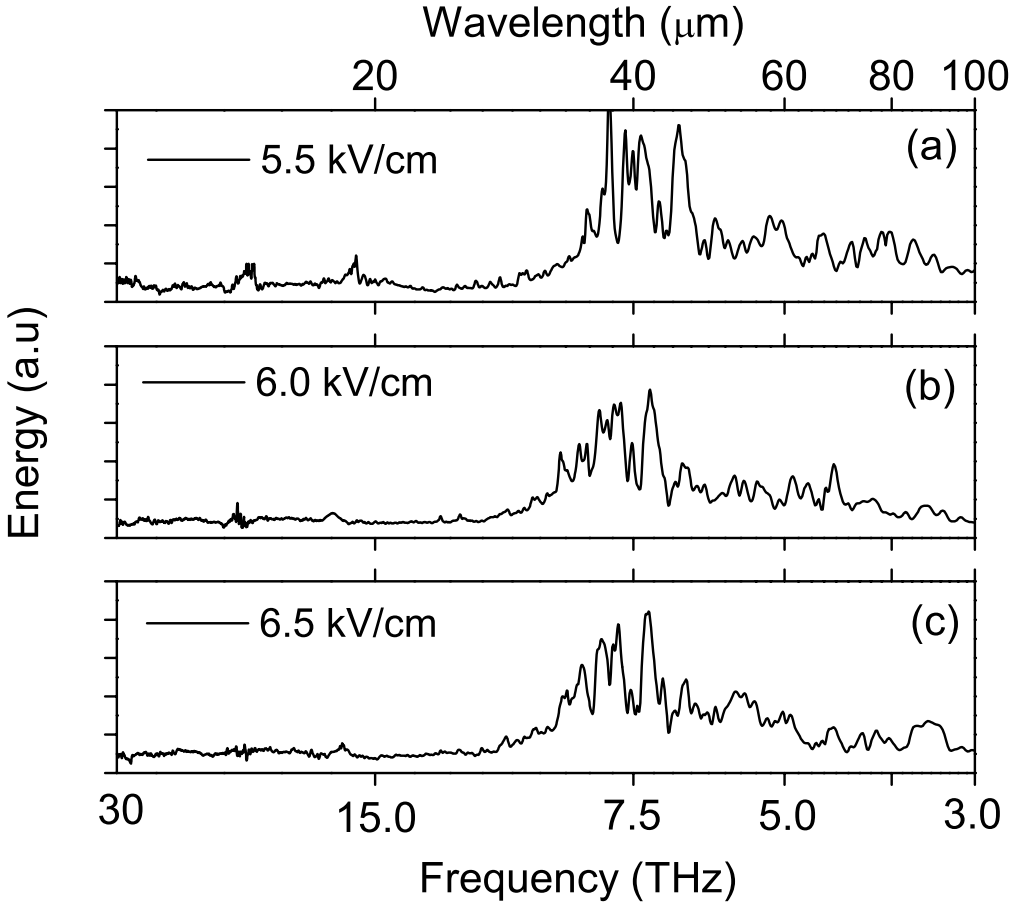

Figure 4.5: The emission spectra divided by the background spectra for (a) 5.5 kV/cm, (b) 6.0 kV/cm, and (c) 6.5 kV/cm. The terahertz emission starting from roughly 10 THz and below can be clearly seen.

4.3 An investigation of terahertz effect on DRG explants

Terahertz technology is one of the emerging technologies with a growing number of applications [7, 8, 9, 10]. A few studies have taken place to investigate the effect of terahertz radiation on biological systems. A study of the effect of terahertz radiation (0.12 - 0.14 THz) on human peripheral blood lymphocytes has concluded that no direct chromosomal damage and no alteration of cell cycle kinetics occurs [80]. The effect of terahertz radiation (1 - 3 THz) on human primary keratinocyte has been investigated [81] and no inhibition or stimulation of cell activities was observed up to the investigated incident energy of 0.45 J/cm^2. Although the photon energy of terahertz radiation is as low as a couple of meV, damage in biological systems can be still induced due to the resonance absorption. In this study the effects of teraherz radiation on the growth of nerve cells was investigated using dorsal root ganglion (DRG) explants from chick embryos as an in - vitro model system in collaboration with Dr. V. Rehder in the Department of Biology and Dr. N. Dietz in the Department of Physics and Astronomy at Georgia State University.

A globar (Model: ORIEL 6363), which has blackbody radiation characteristics, was used as the radiation source. The short wavelength radiation (< 20 μm or > 15 THz) was filtered out to avoid the sample heating by using a black polyethylene filter and a plastic multi-well plate, which was used as the sample holder. Since DRG explants should be kept between 37.0 ± 2.0 ^{0}C during the irradiation, a compartment with an automated temperature controller was built of styrofoam to achieve good thermal stability, and this is shown in Fig. 4.6. Using two mirrors, the terahertz beam was focused onto the sample holder. The radiation spectrum after the black polyethylene and the sample holder

was taken with a Si-composite bolometer and is shown in Fig. 4.7. The total radiation spectrum spans roughly from 5 - 15 THz with the maximum radiation around 11 THz. The total incident radiation power was estimated using the Si-composite bolometer. In this calibration, all the optical components used in the irradiation setup were included. In addition, a white polyethylene filter which has 70 ± 5 % transmission in the frequency range of interest was used. The Model SR 850 DSP Lock-in amplifier with a light chopper was used to measure the output voltage of the bolometer at 4.2 K. Incident power P_i can be estimated as follows,

$$P_i = \frac{V_{bol}}{S_{bol}} f_{wp} f_{area}, \tag{4.1}$$

where,

V_{bol} - voltage output of the bolometer corresponding to the incident light

S_{bol} - bolometer sensitivity

f_{wp} - correction factor for white polyethylene

f_{area} - geometrical area correction factor

The measured V_{bol} is 154.4 mV, the given S_{bol} is 3.4×10^5 V/W, f_{wp} is 10/7, and f_{area} is 7. Therefore, finally, the average incident power is 4 - 5 μW and the average light intensity is not more than 0.25 μW/cm^2.

4.4 Discussion

The DRG preparation and irradiation were carried out under supervision of Dr. V. Rehder of Department of Biology at Georgia State University. The complete experiment procedure can be found in Appendix C. In the first experiment, the short term effect of terahertz exposure on DRG was studied. The second experiment was aimed to investigate

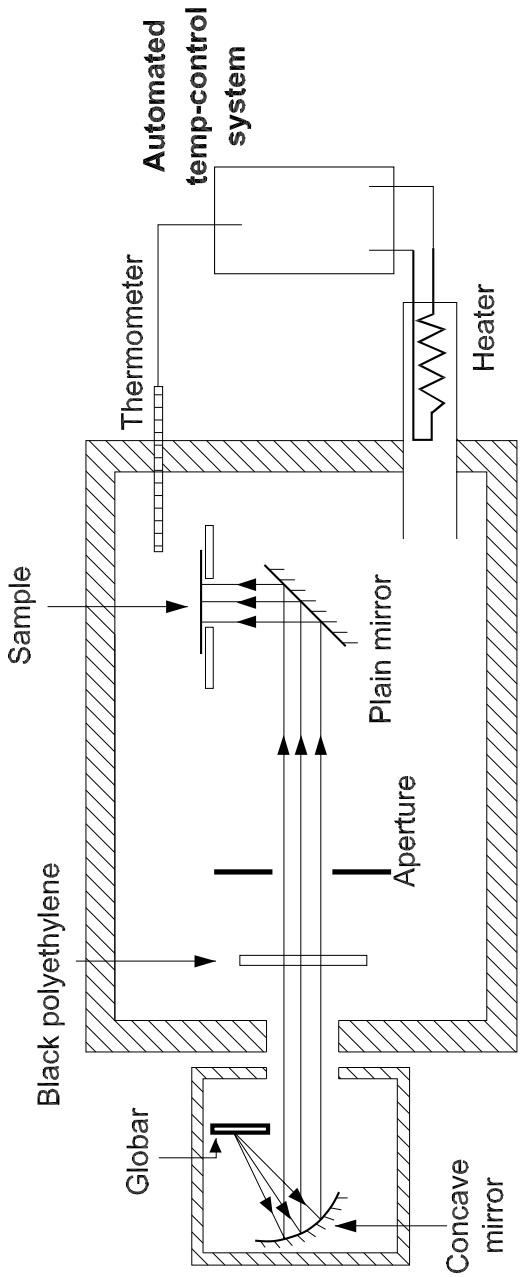

Figure 4.6: The schematic diagram of the complete arrangement for DRG irradiation setup. The terahertz radiation was filtered from the globar by using black polyethylene and the plastic multi-well plate. The radiation spectrum is shown in Fig. 4.7. Mirrors and the aperture were used for focusing. A styrofoam compartment along with an automated temperature control system provides a good thermal stability.

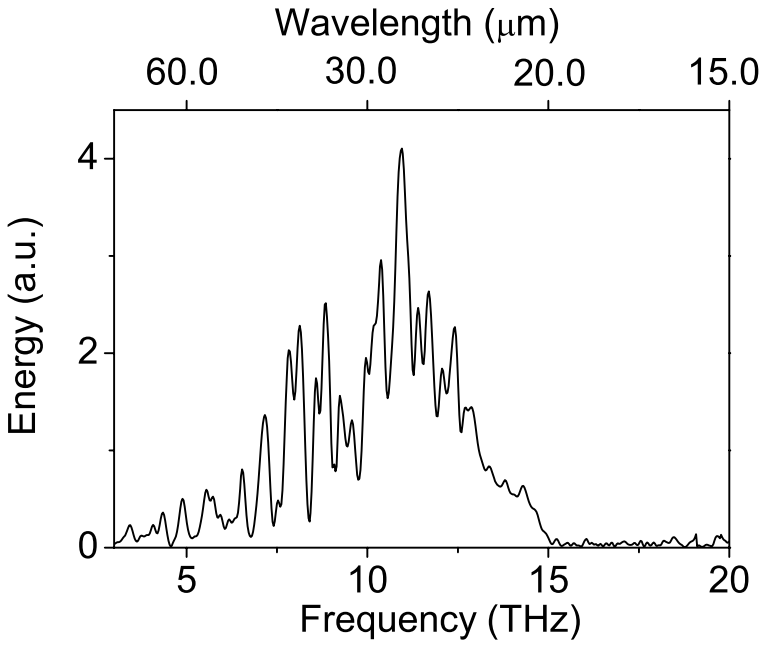

Figure 4.7: The radiation spectrum of the globar used to irradiate DRGs. The spectrum was taken with a Si-composite bolometer with the all optics used in the experiment included. The maximum power that reached the sample compartment is 4 - 5 μW. High frequency/short wavelength IR light ($>$ 15 THz) was filtered out using a black polyethylene filter.

the long term effect of terahertz exposure on DRG. In all experiments, the growth rates of control samples without terahertz radiation, but under the same conditions as the irradiated samples were monitored and recorded in order to compare the results of the irradiated samples.

According to the results (see Appendix C), terahertz radiation may have neither affected the neurite initiation nor outgrowth in the chick model system within the studied terahertz radiation range (15 - 5 THz) under total terahertz power of 4 -5 μW. In conclusion, the effects of terahertz radiation on DRG outgrowth may be negligible under a few microwatts of terahertz exposure. However, further studies will be needed to assess the complete effect of terahertz radiation on the growth rate of DRG explants. It is important to study the effect of terahertz radiation with increasing incident power. The terahertz radiation power of the source used in this experiment is low since the globar is a basic blackbody radiation source. In order to increase the output power, the blackbody radiation source must be heated to high temperatures which is not practical in this type of laboratory experiment because of high heat dissipation. Furthermore, the blackbody sources require a high input power which is not favorable for most of applications. It is essential to develop semiconductor based terahertz emitters such as the GaN emitter discussed above in order to get efficient terahertz sources. In addition, the effect of very short terahertz pulses on biological systems will be another interesting idea since rapid transient radiation fields could interact with biological cells in a different way.

Chapter 5

Behavior of Triggered Electrical Pulses in a GaAs/InGaAs Heterostructure

5.1 Introduction

Development of an artificial neuron has been a challenge for the joint efforts of biologists, physicists, and electrical engineers for a long time [15]. Designing and fabricating artificial neurons with conventional electronics such as transistors and diodes may not be promising in terms of size and power requirements. Therefore, two terminal semiconductor devices such as $p-i-n$ diodes and multilayer quantum well structures (MQW) which have been reported to exhibit SNDR current-voltage characteristics are of great interest. These types of devices can generate neuron-like electrical pulses under suitable voltage or current bias [82, 83] at low temperatures due to the bistability of the s-shaped I-V curve. This pulsing phenomenon has great potential in device physics and will be discussed in Sec. 5.2.2. In this study, the nonlinear behavior of this pulsing phenomenon is investigated.

5.2 Negative differential resistance in semiconductors

Nonlinear carrier transportation can lead to an unstable current-voltage (I-V or J-E) characteristic in certain semiconductor heterostructure devices such as $p-i-n$ diodes, multi quantum well (MQW) devices [84, 85, 86, 87], and certain bulk semiconductors (see Ref. [88]). There are generally two types of unstable I-V behaviors, namely, S-shaped and N-shaped, and these are shown in Fig. 5.1. In both cases, the differential resistance or conductance becomes negative ($\partial J/\partial E < 0$) in the unstable regions, and therefore, the S-shaped region is called the S-shaped negative differential resistance (SNDR) region and the N-shaped region is called the N-shaped negative differential resistance (NNDR) region.

NNDR has been observed in bulk materials such as GaAs or InP and it is due to the inter-valley scattering of free electrons, which leads to the Gunn oscillations [89]. At low fields, the majority of the free electrons are in the Γ - valley of the conduction band. As the applied electric field increases the number of electrons transferred to higher lying L - valley in the conduction band increases and more electrons are transferred to the L-valley from the Γ valley in the conduction band. As this happens, the current through the material decreases giving an NNDR due to the higher effective mass of electrons in the L-valley than that of electrons in the Γ valley. This phenomenon is called the Gunn effect.

In superlattice structures such as GaAs/AlGaAs or GaAs/InGaAs, the NNDR can be found due to resonant tunneling dominant carrier transportation [86]. At resonant tunneling, an excited energy state in a quantum well is aligned with another energy level in the adjacent quantum well due to the applied external field. At this point, the transmission probability of excited carriers is high, and therefore, the conductivity of the heterostructure

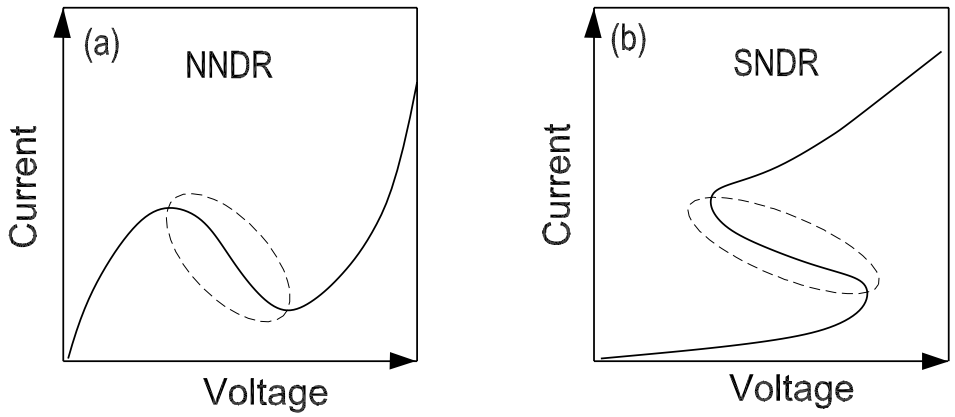

Figure 5.1: (a) The shape of a typical NNDR I-V behavior. (b) The shape of a typical SNDR I-V behavior. The regions marked by the dashed circle possess negative differential resistance.

increases giving higher current. As the applied field increases further, the energy levels start to mis-align and the conductivity and the current decreases giving NNDR characteristics.

Impact ionization involved with impurities such as donors, acceptors, and traps are believed to be a key process responsible for SNDR in bulk materials [90]. However, SNDR in bulk can be a result of the combined effects of impurity ionization, current filamentation, and space charge domain formations. The key factors for SNDR in heterostructures such as GaAs/AlGaA and GaAs/InGaAs could be space charge build up on the interface, impurity impact ionizations, carrier heating, and sudden barrier lowering [91, 92, 93].

To present a simple picture of how SNDR occurs in a heterostructure, a $p-i-n$ diode can be considered based on a process of ionization and barrier lowering. The band diagram of a $p-i-n$ at low field is shown in Fig 5.2 (a) where the tunneling current is dominant, giving a low conductance state to the device. As the bias field increases, the current through diode increases and the impurity ionization rate also increases. This ionization leads to a positive charge build up (space charge) on the upper part of the i-region and makes the i-region conduction band steeper as shown in Fig 5.2 (b). As a consequence of the steeper band formation, the current increases and, in turn, more and more space charge accumulates making the conduction band steeper and steeper. At some point, a sudden barrier lowering can occur leading to a sudden current increase and device's low conductance state switches to a higher conductance state. However, so far, there is no model that can be used to explain such devices consistently. The reason for this has several factors. This mechanism is not a single process but can be a result of several processes. Impurities are believed to be a major factor and the role of impurities is not yet fully understood.

Therefore, making such devices consistently is a challenge even though it is possible to design such devices according to the proposed models. In addition, these devices show NDR characteristics at 77 K or below which makes applications of these devices difficult.

5.2.1 Pulsing and oscillations in SNRD heterostructures

Spontaneous voltage (or current) pulsing and oscillations can be observed if a device that possesses a SNDR behavior is biased in a suitable circuit as shown in Fig. 5.3 (a). R_L, C_L, and C_i are the load resistor, the load capacitor, and the input capacitor, respectively. The requirement for current (or voltage) pulsing or oscillations in the circuit is that the load line needs to cross the SNDR region on I-V curve (see Fig. 5.3 (b)). When the device is biased, initially, the device is in the low conductance state as in Fig. 5.3 (c), and the voltage across the device increases as the input capacitor is charged. Space charge builds up in the i region of the device as the current flows across the device and the slope of the conduction band gets steeper leading to an increase in current (see Fig. 5.3 (d)). At a certain point of this process, a sudden barrier lowering on the junction can happen making the device switch from low conductance state to high conductance state and a surge of electrons will pass through the device giving a voltage (current) pulse at the output end of the device. The corresponding device band diagram will appear as in Fig. 5.3 (e). The extra electron needed for the pulsing is supplied by the input capacitor when the device switches to the high conductance state. However, as the current (or voltage) pulse occurs, the output capacitor gets charged and the voltage at the output end increases, hence, the voltage across the device decreases. The band diagram at this instance will have a shape as shown in Fig 5.3 (f). Note that the input capacitor gets discharged when the device switches

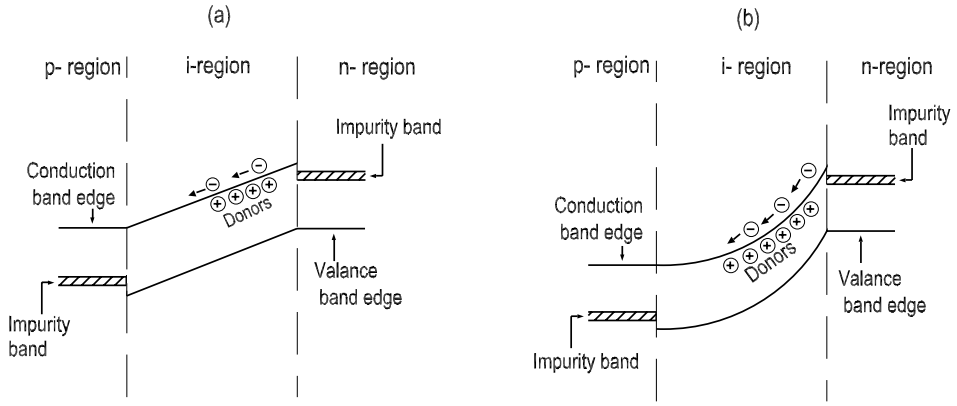

Figure 5.2: Band diagram of a $p - i - n$ diode. (a) At low field, the device is in the low conductance state and the impact ionization rate is minimum in the i-region. (b) As the applied field increases, the impact ionization rate increases leaving a space charge accumulation in the i-region. The conduction and valence bands become steeper, increasing the current. At some point, a sudden barrier lowering can occur and the device will switch to the higher conductance state from the low conductance state. This process is cyclic and goes on as long as the right conditions are met.

to high conductance state. As the voltage across device decreases, the current flow across the device decreases and the device goes back to the initial state as in Fig. 5.3 (c). Thus the device is ready for the next pulse. This process can happen as long as the conditions remain the same.

5.2.2 Characteristics and potential uses of pulsing

It has been shown that the pulsing in $p-i-n$ diodes has similarities to electric pulsing in biological neurons [83, 94, 17, 18, 95]. A simple circuit containing a $p-i-n$ diode as in Fig. 5.3 (a) has properties[83] of Hodgkin-Huxley circuit which has been used to simulate the characteristics of pulses in real biological neurons. Certain characteristics of biological neuron pulses such as period doubling, bifurcation, chaos, excitation, inhibition, summation over inputs, firing thresholds, transient sensing, and overshoot can be seen in $p-i-n$ diode pulsing [83].

This pulsing phenomenon promises a great potential in applications. Feasibility of using this pulsing phenomenon in asynchronous parallel processing for information and imaging processing [17, 18, 19], in computation [82], and in infrared detection [96, 97] has been shown. The added advantages of this type of a fundamental device are low power dissipation on the order of few nanowatts and the physical size in micrometer scale. Therefore, thousands of these devices can be integrated to make arrays for powerful applications such as asynchronous parallel processors and artificial IR retina.

However, it is still a challenge to fabricate such devices consistently due to the lack of a complete model which takes the mechanism of the s-shaped behavior into account. According to reported s-shaped device designs, doping concentrations, well widths, barrier

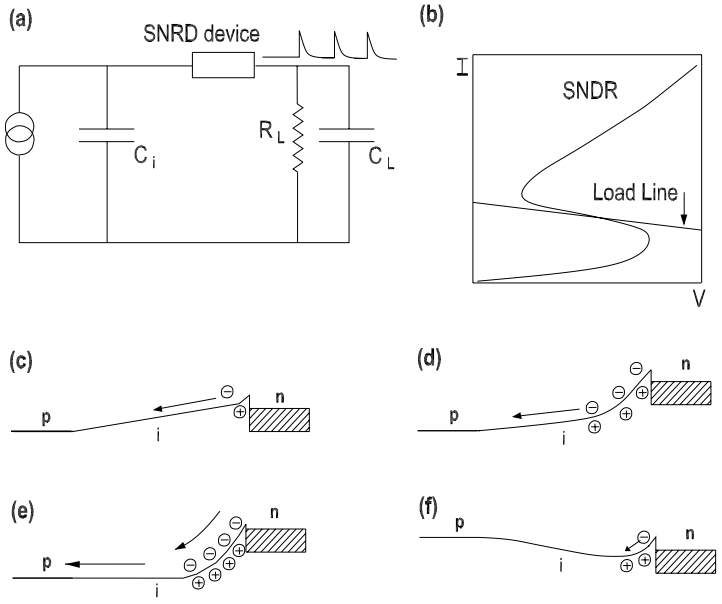

Figure 5.3: (a) A circuit that can be used for triggered pulsing. R_L, C_L, and C_i are load resistor, load capacitor, and input capacitor respectively. (b) The typical I-V curve of SNDR device and the load line of the circuit. For pulsing or oscillations,the load line should cross the NDR region. (c) The $p-i-n$ diode band diagram at low field and the device is in low conductance state. p-layer, intrinsic layer, and n-layer are indicated by p, i, and n respectively. (d) Initially the input capacitor (C_i) gets charged, and the electric field increases and the rate of impact ionization also increases. The conduction band slope of i-region gets steeper due to the space charge build up. (e) Suddenly, barrier lowering can occur giving rise to a surge of current (pulse). (f) As the pulse appears, the input capacitor gets discharged while the load capacitor (C_L) gets charged and the field across the device will be reversed. Then, the device will be pushed back to low conductance state and will be ready for the next pulse.

heights and widths, and impurities are critical for NDR region. The other important factors could be the space charge accumulation at the interfaces of semiconductor layers [98] and defects in semiconductor materials.

In this study, the nonlinear behavior of triggered pulses of a GaAs/$In_xGa_{1-x}As$ MQW heterostructure grown by molecular beam epitaxial technique (MBE) was investigated. Spontaneous pulsing in $p^+ - n - n^+$ devices has shown a rich nonlinear behavior under different operational conditions and has been studied before[98, 99]. Preliminary studies on inter pulse time intervals (IPTIs) based on power spectra and first return maps showed that the IPTIs of the MQW device possessed nonlinear behavior. Estimations for the correlation dimension and phase space dimension that could help in understanding the phenomena were also investigated.

5.3 Experimental setup

The MQW device used in this study consists of 20 periods of 338 Å GaAs barriers and 83 Å $In_{0.087}Ga_{0.913}As$ wells with highly doped GaAs top and bottom contacts and a partial band diagram as shown in Fig. 5.4 (a). The I-V characteristic of the MQW device is shown in Fig. 5.4 (b) and the device shows SNDR characteristic below 23 K. However, the SNDR region shifts upward and its SNDR shrinks with increasing temperature. Above 23 K, the SNDR region disappears. The MQW device at 10 K was operated in a simple circuit as shown in Fig. 5.3 (a) and a rectangular pulse train with pulse amplitude of 10 mV and width of 2 μs were applied in order to trigger pulses. Without triggering pulses, either the MQW device did not pulse or stayed in the oscillatory mode. The amplitude of

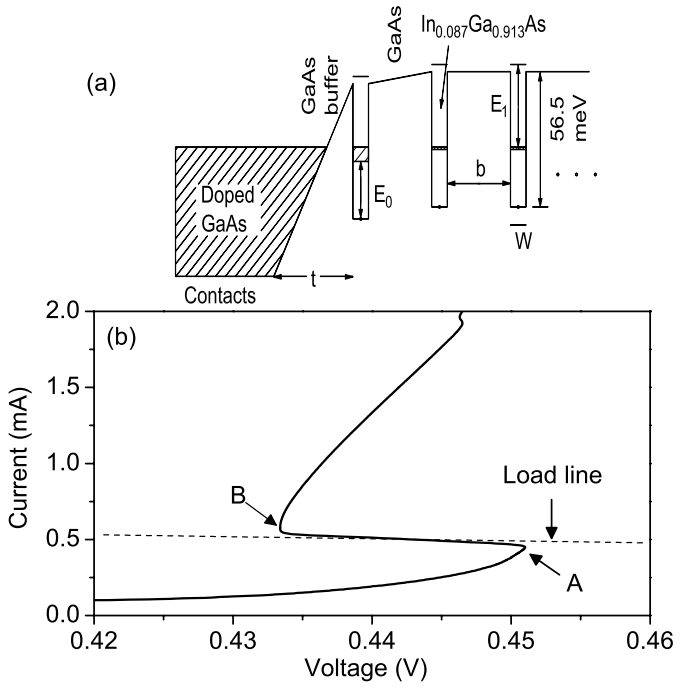

Figure 5.4: (a) The $In_{0.087}Ga_{0.93}As$/GaAs MQW device designing. GaAs contacts are highly doped. The InGaAs wells are 83 nm thick and GaAs barriers are 338 nm thick. (b) Current voltage characteristics for the pulsing MQW device at T = 10 K. The device has the s-shaped I-V characteristics below T = 23 K. The SNRD is from A to B. The dotted line represents the load.

triggered pulses is approximately 30-35 mV at 10 K ($\sim$ 40 mV at 4.2 K) and decreases with increasing temperature. The triggered pulses were amplified and fed into a Lecroy 2323 programmable dual gate Transistor Transistor Logic (TTL) output generator to produce TTL signals corresponding to the input signals. The TTL output signals were fed into a National Instrument PCI 6602 Counter/Timer board to measure the time intervals between consecutive TTL signals which were IPTI of triggered pulses. A Wavetek (Model 275) function generator was used as the triggering signal generator. IPTIs were collected under different device operating conditions such as device temperature, bias voltage or current, and triggering signal frequency. The schematic diagram of the setup is shown in Fig. 5.5.

5.4 First Return Maps

In general, first return maps, where the $(i+1)^{th}$ measurement is plotted against the i^{th} measurement in a series of a measurement, are quite useful for analyzing nonlinear processes. First return maps of IPTIs at different bias currents and voltage were used to analyze nonlinear behavior of IPTIs. The general behavior of IPTIs with decreasing bias current is shown in Fig. 5.6. The following development in the first return maps can be clearly seen. When the bias current is near the transition current (point-A) as shown in I-V curve in Fig. 5.4 (b), the device responds to each and every triggering voltage signal by producing a pulse. Therefore, each IPTI is as long as IPTI of the triggering voltage signal and hence, the first return map shows only a single point (see Fig. 5.6 (a)). As the bias current moves from the transition point A to a lower value, the ability of the device to respond to each and every triggering voltage signal decreases due to the smaller electric

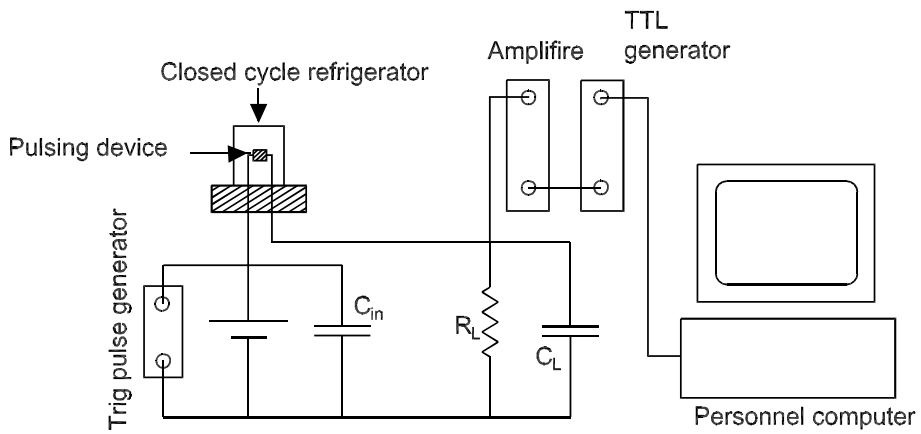

Figure 5.5: The complete measurement setup used in the experiment. The device is in the liquid He cooled closed cycle refrigerator. Pulses are triggered by using trig pulse generator and are amplified and fed into TTL generator. Finally the IPTIs are recorded by using PCI timer/counter board.

field across the device than the earlier case. Therefore, IPTIs take a range of values giving rise to a different types of first return maps. The first return map for 0.294 mA bias current shows several IPTI values as seen in Fig. 5.6 (b). However, all IPTIs are multiples of the 20 μs triggering signal period. Further decrease in the bias current leads to an intriguing development in first return maps; i.e., groupings of IPTIs form as seen in Fig. 5.6 (c) and 5.6 (d). As the bias current decreases further, more and more groups develop. Initially, the time separation among the groups (from center to center) is 0.5 - 0.6 ms as seen Fig. 5.6 (c). When it reaches a state similar to Fig. 5.6 (d), the time separation between consecutive groups is about 0.7 - 0.8 ms. When the bias current is so small that triggering signal barely can trigger pulses, a second layer of groups emerges, and these new groups are large and made up of the first layer of groups (see Fig. 5.7 (a)). If one of these larger groups is enlarged, the first layer of groups is visible as seen in Fig. 5.7 (b). Generally, 8000 - 10000 smaller groups can be found in a single larger group. The number of points in each smaller group is now less because points are distributed among thousands of smaller groups, therefore, the smaller groups are not as clear as the previous smaller groups seen in Fig. 5.6 (d). The separation between larger groups is $\sim$ 400 ms while the separation between smaller groups has increased to $\sim$ 3 ms. This shows that time interval among smaller groups has changed from roughly 0.5 ms to 3 ms when the pulsing rate decreases.

The groupings are clearly seen for triggering signal frequencies 10, 20, 25, 40, and 50 kHz and cannot be clearly detected for some other frequencies such as 11, 15, 18, and 30 kHz. However, the data point density variation in the first return maps for triggering signal frequencies 11, 15, 18, and 30 kHz revealed that groups exist but overlap with each

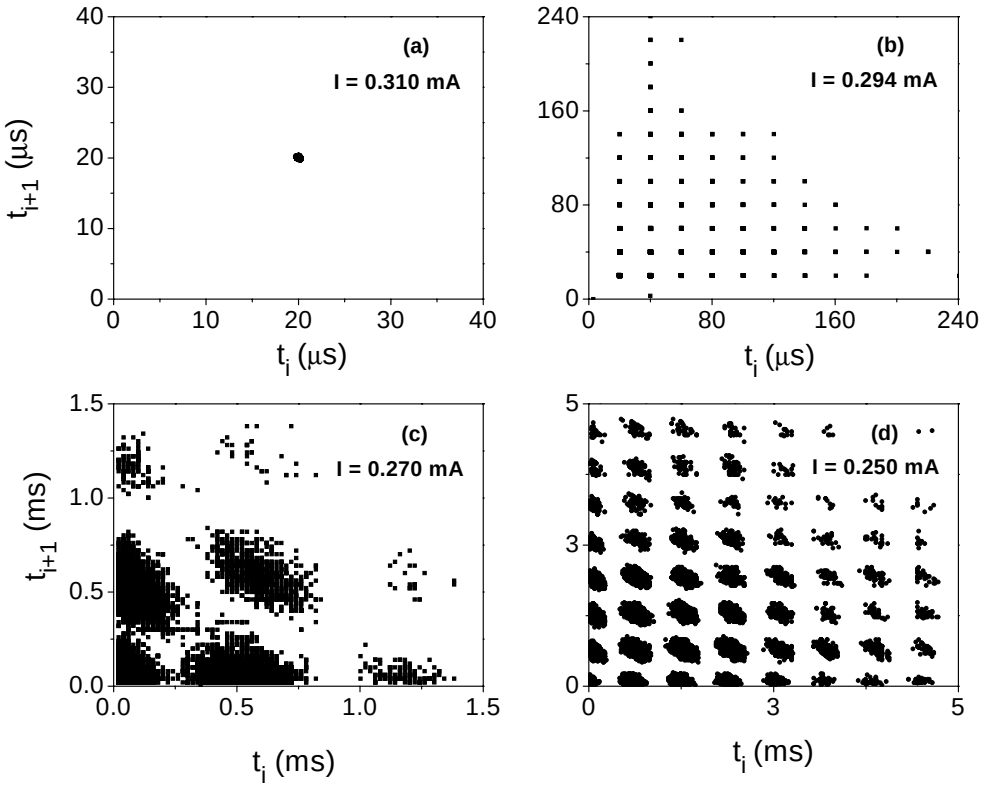

Figure 5.6: The first return maps for different bias currents (a) At I_b=0.310 mA, all IPTIs are same as the that of the triggering signal which is 20 μs. (b) at I_b=0.294 mA, IPTI has several values but all are multiple of the triggering signal period. (c) At I_b=0.270 mA, formation of the first couple of groups can be seen. The time separation among groups time interval is $\sim$ 0.5 ms (d) at I_b=0.250 mA, the pulsing rate is quite slow. There are more groups and they are clearly distinguishable. The time separation among groups is now $\sim$ 0.8 ms.

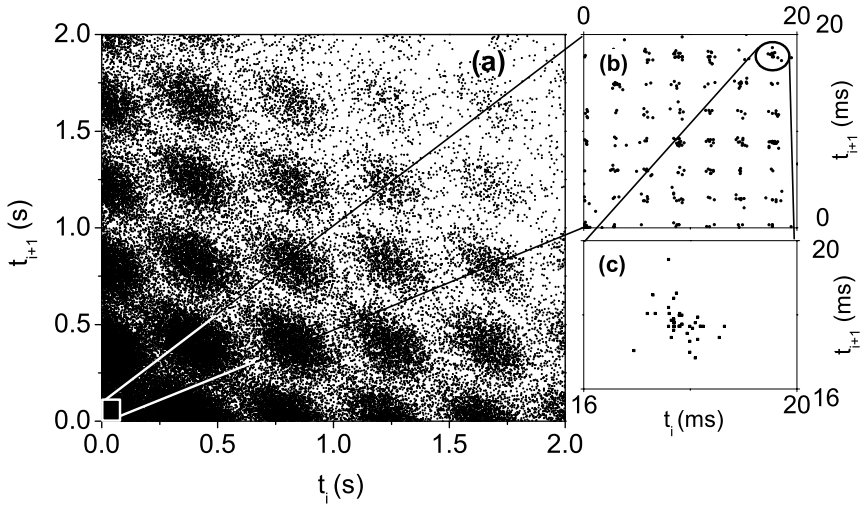

Figure 5.7: (a) Larger groups at low bias voltage. Each larger group is made of 8000 - 10000 smaller groups that are similar to the groups in fig. 5.6. The time separation (from center to center) among larger groups is roughly $\sim$ 400 ms. (b) Expanded portion of area 0 - 20 ms and the smaller groups can be clearly seen inside the larger group. Time separation among the smaller groups $\sim$ 3 ms. A single smaller group is shown in (c). However, it is less populated because same number of data points has been distributed over a very large number of groups.

other. The grouping behavior can be observed not only under current bias but also under voltage bias. Characteristics of grouping are the same for both current bias and voltage bias conditions.

This grouping can be associated with oscillations of the device threshold level. The first layer of groups can be empirically modeled by introducing a sinusoidal fluctuation, $I_0 sin(\omega_0 t)$ to the constant threshold level of the device; I_{thresh}. The first return map of the simulated IPTIs shown in Fig. 5.8 (a) clearly shows the first layer of groups. The second layer of groups can be obtained by introducing a second low frequency sinusoidal fluctuation to the device threshold giving total threshold $I_{thresh} + I_0 \sin(\omega_0 t) + I_1 \sin(\omega_1 t)$. The corresponding first return map is shown in Fig. 5.8 (b) and the second layer of groups can be seen. There are three larger groups and each larger group consists of smaller groups. Arbitrary dimensionless frequencies were used for the simplicity. Introducing white noise to the system can spread the groups over wide areas similar to the experimental ones. Space charge fluctuation in the device and small temperature fluctuations can lead to noise. The threshold oscillation frequency can be obtained from first return maps. According to the first return maps of the experimental data (Fig. 5.6 (c,d)), the first layer of groups corresponds to high frequency oscillations which vary roughly from 0.35 to 2 kHz with decreasing applied bias current and the second layer of grouping is corresponding to low frequency oscillation which is about 2 Hz according to the first return map (Fig. 5.7). Both bulk GaAs and GaAs superlattice structures are known for propagating charge domains [100, 101, 102]. These moving charge domains can produce current oscillations in the MQW device. Therefore, the pulsing threshold level of the MQW device can fluctuate accordingly.

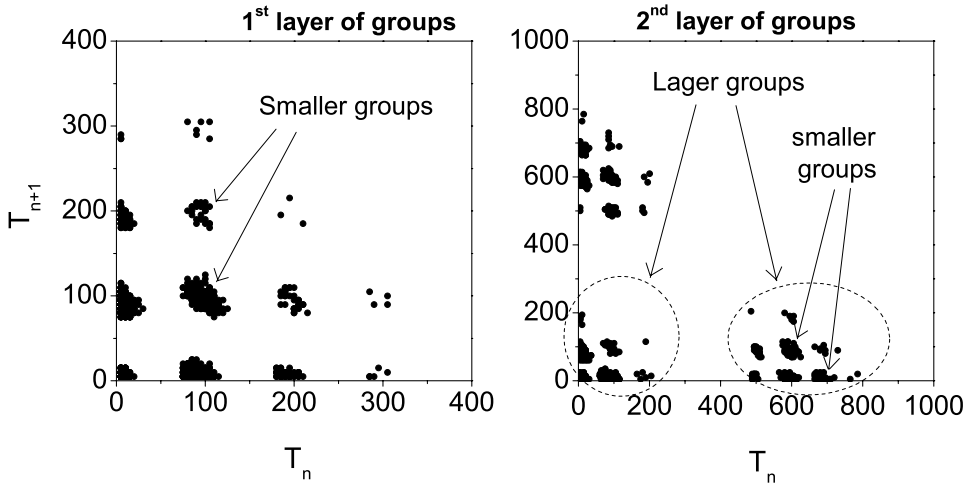

Figure 5.8: Illustrates how the grouping occurs when the device threshold level fluctuates.(a) IPTIs pattern after introducing $I_0\sin(\frac{2\pi t}{T_0})$ to the threshold with a period of $T_0 = 100$. Smaller groups can be clearly seen and it resembles the first layer of groups. (b) First return maps of IPTIs after introducing $I_0\sin(\frac{2\pi t}{T_0}) + I_1\sin(\frac{2\pi t}{T_1})$. The periods T_0 =100 and T_1 =1000. This resembles the second layer of groups. There are three larger groups which are made of smaller groups (the first layer of groups). Arbitrary dimensionless frequencies were selected for the simplicity and white noise was introduced to make the first return map similar to experimental return maps.

The meaning of groupings is that there are allowed and forbidden time bands for IPTIs. The development of the IPTI bands is shown in Fig. 5.9 at four different bias currents; I_{bias} = 0.290, 0.270, 0.260, and 0.250 mA. At the bias current, I_{bias} = 0.290 mA, there is only one band which is about 0.4 ms in width. When the bias current decreases to I_{bias} = 0.270 mA, the second band develops which is separated by roughly 0.2 ms gap. IPTIs develop into four and eight bands at I_{bias} = 0.260 mA and I_{bias} = 0.250 mA, respectively. With decreasing bias current, more and more IPTI bands can be seen. As more bands develop, the width of bands decreases slightly and separation between bands increases slightly. The IPTI band development is somewhat similar to bifurcations found in chaotic systems in nature.

Although the first return maps show a clear pattern of IPTIs, according to power spectra, there is no visible temporal pattern in IPTIs when groups develop. The evolution of the power spectra with decreasing bias current is depicted in Fig. 5.10. At a bias current of I_{bias} = 0.294 mA [see Fig. 5.10 (a)], two very long periodic patterns can be seen: at frequencies of roughly $\frac{1}{25}$ and $\frac{1}{16}$ and the first harmonic of $\frac{1}{16}$. At a bias current of I = 0.292 mA, the peaks in the power spectrum as seen in Fig. 5.10 (b) are not as sharp as those in Fig. 5.10 (a) but are slightly broader. However, grouping has not yet started at these bias currents. As the bias current decreases, grouping starts slowly, the main peak gets broader and broader and the frequency gets larger and larger as seen in Fig. 5.10 (c,d). Further decrease in bias current leads to complex and broader spectra as in Fig. 5.10 (e,f) and well developed groups can be seen in first return maps as in Fig. 5.6 (d). There is no clear temporal pattern in IPTIs according to power spectra. The change of the power spectra

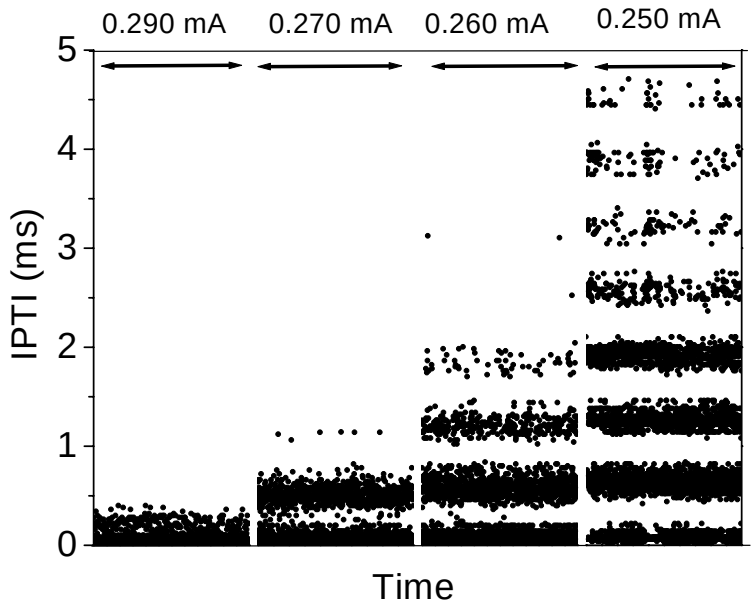

Figure 5.9: IPTI band formation with decreasing device bias current. At I = 0.290 mA, only one band of IPTIs is possible; IPTI is roughly below 0.4 ms. When bias current reaches 0.270 mA, IPTIs show splitting and give two types of IPTI bands. When the bias current reaches 0.265 mA, The IPTIs undergoes one more splitting giving three bands of IPTIs. As the bias current keeps decreasing, more and more IPTI bands develop.

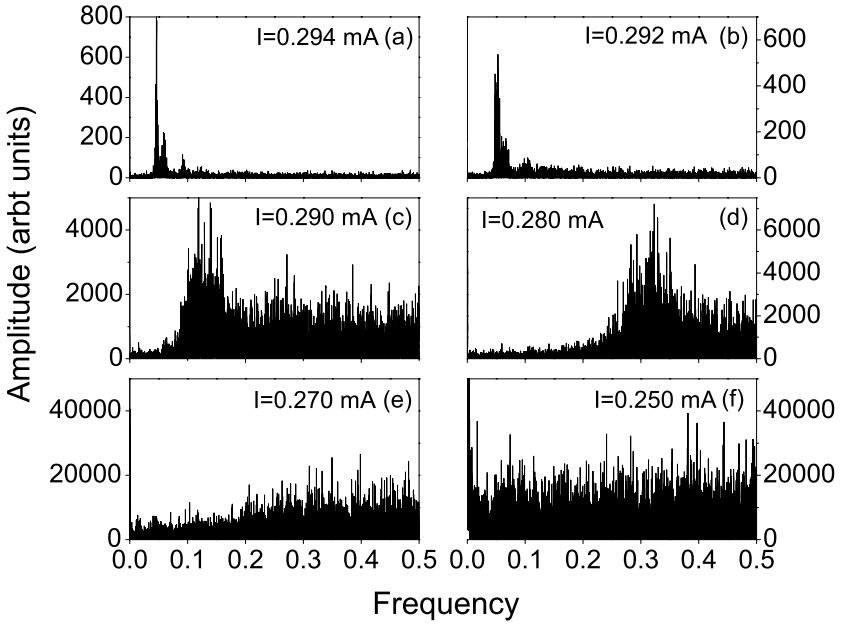

Figure 5.10: Power spectrum development in IPTS's as bias current decreases. (a) At I_b = 0.294 mA, peaks of $\frac{1}{25}$,$\frac{1}{16}$ and its first harmonic can be seen. (b) At I_b = 0.292 mA, frequencies of the peaks have increased by a small amount and become broader. (c) and (d) Further decrease in bias current leads to a single broader peak. Formation of groups starts at this level. (d) and (e) At very low bias current, the power spectra become much broader and complex. Well developed groups can be seen in the corresponding first return maps [see Fig. 5.7].

from a long periodical line spectrum to a broad spectrum with the decreasing bias current suggests nonlinear behavior.

5.5 Estimation of Correlation Dimension

Knowledge of the dimensionality of the system helps us understand the system operation and parameters which are responsible for NDR region, including space charge build up inside the device. Furthermore, it could help develop a model that can predict the pulse pattern. The correlation dimension, D_2 can give a good understanding of dimensionality of a non-linear system. Grassburger and Procaccia presented a convenient method[103] to calculate the correlation dimension D_2 from a single time series. They have shown that correlation integral, $C(R)$ can be calculated as follows

$$C(R) = \frac{1}{N^2} \sum_{i=1}^{N} \sum_{j=1}^{N} \Theta[R - (\overrightarrow{X_i} - \overrightarrow{X_j})] \tag{5.1}$$

where $\overrightarrow{X_i}$, $\overrightarrow{X_j}$ are i^{th} and j^{th} m-dimensional embedded vectors made of discrete measurements of the time series, R is scaling region, N is number of data and

$$\Theta[R - (\overrightarrow{X_i} - \overrightarrow{X_j})] = 0 \qquad if \quad R \leq (\overrightarrow{X_i} - \overrightarrow{X_j}) \tag{5.2}$$

$$\Theta[R - (\overrightarrow{X_i} - \overrightarrow{X_j})] = 1 \qquad if \quad R > (\overrightarrow{X_i} - \overrightarrow{X_j}) \tag{5.3}$$

Furthermore, they have shown that correlation integral, $C(R)$ behaves as a power ν of R for small R .

$$C(R) \propto R^{\nu} \tag{5.4}$$

and correlation dimension, D_2

$$D_2 \approx \nu \tag{5.5}$$

where $C(R)$ is the correlation integral and given by Eq. 5.1, and R is called the Scaling Region. Correlation dimension, D_2 can be found by calculating the slope of ln(C(R)) vs ln(R) in the linear scaling region. The scaling region, R should be carefully picked so that the slopes of ln(C(R)) vs ln(R) for different embedded dimensions should remain constant after a certain embedded dimensions. Generally, this method is popular because of its accuracy and speed. Sauer [104] has shown that the above method can be used for point processes such as time interval measurements between events. IPTI measurements in this experiment are also a point process and Eq. 5.1 can be used to investigate the correlation dimensions.

Using Eq. 5.1, the correlation integrals, $C(R)$ for different sets of IPTIs were calculated for different scaling regions R and for different embedded dimensions m and then $ln(C(R))$ vs. $ln(R)$ were plotted and slopes in the best linear regions were found for different embedded dimensions, m. Finally those slopes were graphed against embedded dimension, m, as shown in Fig. 5.11. If the slopes reached a plateau after a certain embedded dimension, m, then the average value of the plateau was taken as an estimation of the correlation dimension, D_2. Table 5.1 gives the estimated correlation dimensions, D_2 for four data sets that showed converging slopes with increasing embedded dimension, m.

The calculated D_2 vs. m for the above four data sets is shown in Fig. 5.11. The correlation dimension, D_2 for SET-1 converges to a value of 8.5 after embedded dimension, m reaches ~ 20 as seen in Fig. 5.11 (a). In general, if D_2 converges, then it starts converging when $m \geq D_2$[105]. In the worst case, it can happen when $m \sim 2D_2$[106]. Here, in this case, the plateau starts around $m \sim 20$, and it is roughly equal to $2D_2$. The bias current in this

Table 5.1: Four data sets that showed converging correlation dimension, D_2. The data were collected under different operational conditions such as voltage bias or current bias, temperature, triggering signal frequency, f_{trig} .

Data set	Bias	Temp (K)	f_{trig} (kHz)	Number of Data	D_2
SET-1	V = 3.84 V	4.2	50	200000	8.5
SET-2	I = 0.315 mA	12	20	200000	10
SET-3	I = 0.300 mA	10	10	150000	8
SET-4	I = 0.300 mA	10	15	150000	8

situation is close to the transition current [see Fig. 5.4 (b)], therefore, the IPTIs are only a couple of times the triggering signal period and there is no grouping in the first return map. The power spectrum of SET-1 has two long periodic patterns, one with frequency roughly about $\frac{1}{160}$ and its first harmonic, the second one with frequency roughly about $\frac{1}{55}$. The calculated autocorrelation (See Appendix C) for SET-1 is very small and less than $|0.2|$. Therefore, there is neither a strong correlation nor a random behavior.

Correlation dimensions, D_2 against embedded dimension, m for SET-2 are shown in Fig. 5.11 (b). The device temperature, bias current and the triggering signal frequency are 12 K, 0.315 mA, and 20 kHz, respectively. The correlation dimension, D_2 converges to $\simeq 10$. The corresponding first return map of SET-2 is shown in Fig. 5.7 with well developed groups in it. All those larger groups are formed by the smaller groups as explained in Section 5.4. The corresponding power spectrum has a broad spectrum suggesting that there is no simple temporal pattern associated with the IPTIs. The calculated autocorrelation function for SET-2 does not show a strong autocorrelation in IPTIs. It starts from approximately 0.06 and drops to zero after a time lag of 14000.

The variation of correlation dimension, D_2 with embedded dimension, m for SET-3 and SET-4 collected under the same operational conditions given in Table 5.1 except the triggering signal frequency are shown in Fig. 5.11 (c,d). Both sets converge towards correlation dimension, D_2 of 8.0 when the embedded dimension, m is greater than 20. The corresponding first return maps for both sets have no grouping because $I_{bias} = 0.30$ mA is fairly close to the transition current at the operating temperature T = 10 K, and IPTIs are only a few times the triggering signal period.

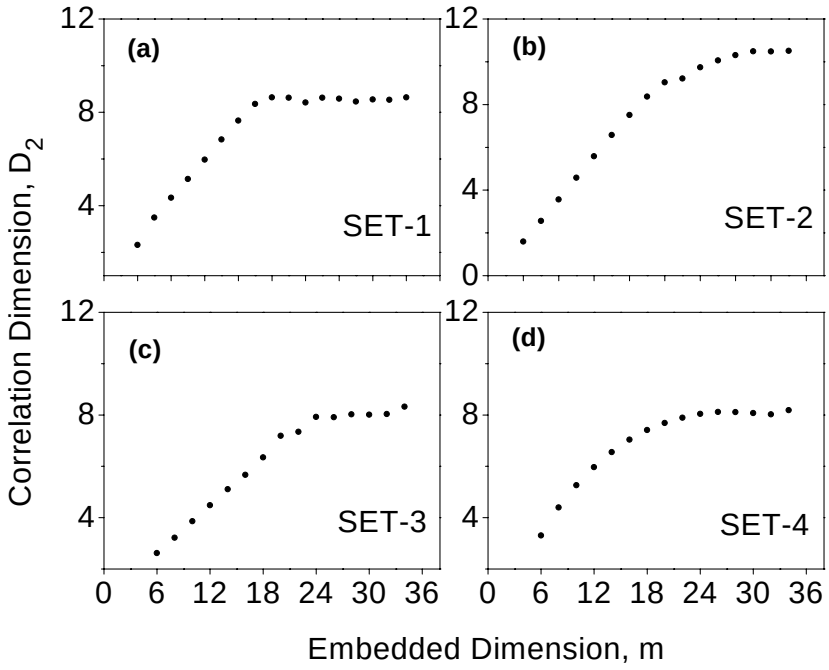

Figure 5.11: The correlation dimension, D_2 vs. embedded dimension, m. The converging of the correlation dimension, D_2 starts roughly m = 20. (a) For SET-1, $D_2 \sim 8.5$ (b) For SET-2, $D_2 \sim 10.0$ (c) For SET-3, $D_2 \sim 8.0$ (d) For SET-4, $D_2 \sim 8.0$.

The convergence of D_2 in the above data sets is reasonably good. The corresponding power spectra and autocorrelations suggest that the data sets have neither strong correlation nor a randomness in IPTIs which can give spurious correlation dimension, D_2. Furthermore, a surrogate data study was carried out to confirm the nonlinearity of IPTIs and validity of the calculated correlation dimension, D_2. In general, surrogate data are generated using the original time series so that surrogate data has the same statistical and power spectrum characteristics as the original time series has, but, it has no deterministic properties. Therefore, the correlation dimension, D_2 for surrogate data keeps increasing with increasing embedded dimension, m. For this study, surrogate data were generated according to the Amplitude Adjusted Fourier Transformation (AAFT) algorithm [107] (see Appendix D) for each data set in Table 5.1 and, thereafter, correlation dimensions, D_2 were calculated for generated surrogate data sets. The correlation dimensions, D_2 of both original data sets and surrogate data sets were compared. They clearly show that while correlation dimensions, D_2 of the original data converge, the correlation dimensions, D_2 of corresponding surrogate data do not converge and keep increasing as shown in Fig 5.12. If the correlation dimension, D_2 of the original data keeps increasing with increasing embedded dimension, m, the data are not deterministic. If the correlation dimension, D_2 of surrogate data converges to some value with increasing embedded dimension, m, both original data and surrogate data would produce spurious correlation dimension, D_2. In this test, the correlation dimension, D_2 of surrogate data does not converges. Thus, the surrogate data studies and the original data studies confirmed the deterministic nature of IPTIs obtained from experiments.

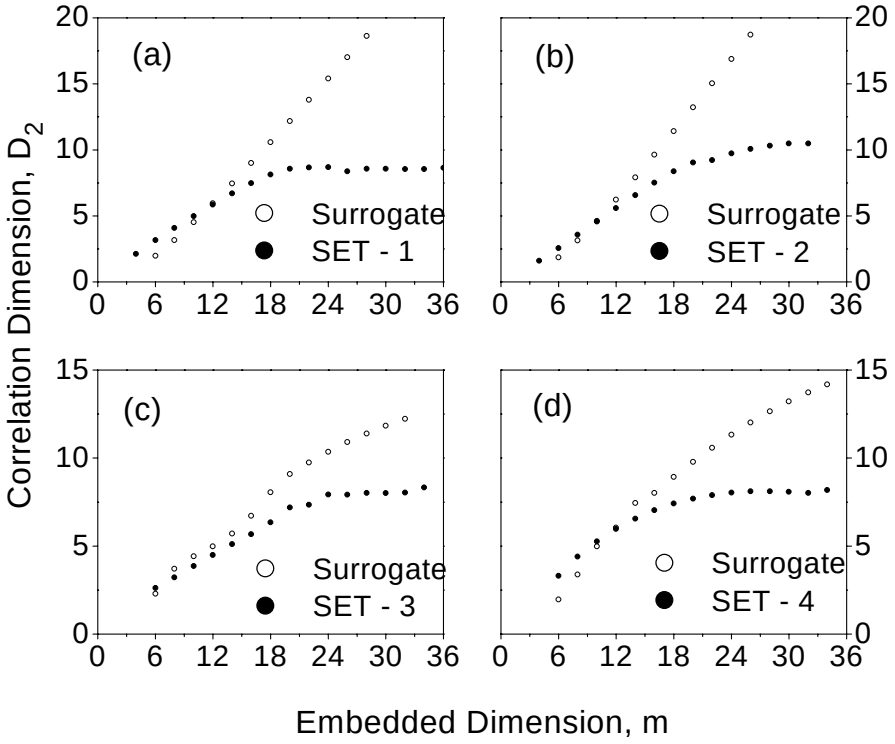

Figure 5.12: The correlation dimension, D_2 vs. embedded dimension, m for the surrogate data (open circles) and the original data. Correlation dimension, D_2 of surrogate data (solid dots) does not converge while the original data does indicating the determinism associated with the original data.

5.6 Discussion

First return maps show an interesting feature, the grouping of IPTIs. Grouping starts to appear on first return maps when the pulse rate is slower. This grouping is clearly seen when the triggering signal frequency is 10, 20, 25, 40, and 50 kHz, but it is not quite visible for frequencies such as 11, 15, 18, and, 30 kHz and the groups are smeared out. Oscillation of the threshold level of the MQW device can lead to this grouping behavior as shown in Section 5.4. The threshold oscillation frequency changes roughly from 0.3 to 2 kHz with decreasing bias current. Therefore, the oscillation frequency depends on the bias current. The resonance frequency in the circuit output branch is about 4.5 Hz, i.e., the period of it is roughly about 200 ms whereas the high frequency oscillations of the threshold vary roughly from 350 to 2000 Hz, which gives the first layer of groups. Time separations among the second layer of groups (larger groups) are about 400 - 500 ms which is roughly 2 Hz. Therefore, there is no apparent circuit resonance frequency influencing the grouping formation. The characteristics of grouping did not change significantly with changes of load resistor R_L and C_L.

A similar type of behavior in IPTIs from cold receptor neurons of cats with changing temperature was reported and IPTI bands formation similar to Fig. 5.9 was presented [108]. Roughly six IPTI bands can be seen at temperature of 35^0 Celsius. If first return map of IPTIs is plotted, it will make several groups similar to that was seen in this study. Furthermore, this type of behavior in IPTIs of rat facial cold receptor neurons has also been reported[109]. They have seen that IPTIs from the rat facial cold receptor neuron split (bifurcate) into two different bands of IPTIs with temperature. In the first return map IPTIs,

three groups can be clearly seen. This MQW device demonstrates a similar phenomenon with decreasing bias current. Even with increasing temperature, grouping behavior IPTIs would be seen. If the bias current and triggering signal frequency are constant, while increasing the operational temperature slowly, in the beginning, the device would start responding with a faster pulse rate and would slow down as temperature increases. Because the NDR region shifts upward with the increasing temperature making the bias current a little further away from the transition current of the I-V curve. In other words, this situation is similar to the situation where bias current is gradually reduced as discussed in Section 5.4. Therefore, groupings IPTIs with increasing temperature can be seen. Both the device and the cold receptor neuron show a similar pattern in IPTI behavior.

The behavior of the driven pulse pattern under voltage bias does not show a significant difference from that of under current bias. Generally, the temporal pattern of IPTIs in $p^+ - n - n^+$ under constant current bias[110, 98] is different from constant voltage bias[111, 96]. The MQW device can produce the same IPTI pattern irrespective of whether it is biased under constant current or constant voltage, provided that the biasing is large enough so that total current is close to the transition current, point-A [see Fig. 5.4 (b)]. It shows grouping of IPTIs under smaller constant current bias as well as under smaller constant voltage bias.

Even though groups in first return maps are in good arrangement, there is no simple periodic pattern in power spectra of corresponding IPTIs. There is a relationship among IPTIs since t_i and t_{i+1} are allowed to visit only selected regions in first return maps. Identifying that relationship would help develop an algorithm which can predict IPTIs.

According to the calculations, the correlation dimension, D_2 is quite large and varies from 8 to 10. This means the dimension of the phase space can be between 8 and 10. In this study, several data sets were collected under different biases, temperatures, and triggering signal frequencies. Correlation dimensions, D_2 were calculated for all data sets. However, only data sets shown in Table 5.1, demonstrated converging correlation dimension, D_2 with increasing embedded dimension, m. Other data sets did not show convergence. Correlation dimensions of the data sets which were collected under the same operational parameters as for SET-1, SET-2, SET-3, and SET-4 except for one variable were carefully examined and did not show a trend with changing parameter. Surrogate tests were carried out to confirm the reliability of the calculated correlation dimensions, D_2 and, in addition, calculated autocorrelation of IPTIs reveals a weak correlation among IPTIs. As a whole, the correlation dimension, D_2 converges to fairly high values providing evidence of the high dimensionality. This can be another situation where high correlation dimensions are reported [112, 113]. Unfortunately, due to practical reasons, we are unable to come to a conclusion about the exact correlation dimension within a reasonable error.

Appendix A

Levenberg-Marquardt Nonlinear Fitting Algorithm

Levenberg-Marquardt algorithm [25] is a powerful nonlinear fitting method. A brief introduction will be given in this Appendix. For a detailed description, please see Ref. [25]. First of all, lets define the model to be fitted as follows,

$$y = y(x; \mathbf{a}) \tag{A.1}$$

χ^2 can be calculated using,

$$\chi = \sum_{i-1}^{N} \frac{[y_i - y(x_i; \mathbf{a})]}{\sigma_i}, \tag{A.2}$$

where y_i is the i^{th} experimental measurement and N is the total number of measurements. Now, when $k = l$, lets define

$$\alpha_{ll}^{'} = \alpha_{ll}(1 + \lambda), \tag{A.3}$$

and, when $k \neq l$

$$\alpha_{kl}^{'} = \alpha_{kl}, \tag{A.4}$$

where λ is a nondimensional constant. α_{kl} is given by

$$\alpha_{kl} = \sum_{i-1}^{N} \frac{1}{\sigma_i^2}[\frac{\partial y(x_i;\mathbf{a})}{\partial a_k}\frac{\partial y(x_i;\mathbf{a})}{\partial a_l}], \tag{A.5}$$

The best fit parameters for the function $y = y(x;\mathbf{a})$ can be obtained as follows,

1. compute $\chi^2(\mathbf{a})$ with an initial guess for the set of parameters $\mathbf{a}$.

2. pick a value for λ (λ=0.001)

3. obtained values for $\delta\mathbf{a}$ using Eq. A.3 and Eq. A.4, and evaluate $\chi^2(\mathbf{a}+\delta\mathbf{a})$

4. if $\chi^2(\mathbf{a}+\delta\mathbf{a}) \geq \chi^{\mathbf{2}}(\mathbf{a})$, multiply λ by 10 (or any other factor) and repeat step (3)

5. if $\chi^2(\mathbf{a}+\delta\mathbf{a}) < \chi^{\mathbf{2}}(\mathbf{a})$, divide λ by 10 (or any other factor) and repeat step (3), and update $\mathbf{a} \leftarrow (\mathbf{a}+\delta\mathbf{a})$

The above iteration process can be carried out until $\chi^2(\mathbf{a})$ becomes satisfactorily small.

The following program is a part of the main IR reflection fitting program originally written by Zhigao Hu and modified by A. Weerasekara. It gives the fitting procedure and calculate the Least square values, initialize the linear derivative equation, and minimization. Parameters used in the programs are given below

DataPointFit - number of experimental data,

Expdata - experimental data,

FixorFitP[] - tells if the parameter is fixed or free ,

ParameterNumber - number of fitting parameters used,

OscillatorNumber - number of oscillators used,

***ModelSelection** - selects the dielectric function,

```
/* A part of the main IR reflection fitting program originally written by Zhigao Hu and modified
by A. Weerasekara. to calculate the least square values and initialize the linear derivative equation.
*/

 void Mrqcof (double wavenumbers[], int DataPointFit, double *Expdata, int FixorFitP[],
                    double Parameter[], int  ParameterNumber, double **alpha, double  beta[],
                   double *chisq, double *sig, int *OscillatorNumber, int *ModelSelection,
                   double (*spectra) (double, double *,int *,int *))
 {
          int i, j, k, l, m, ParameterFitNumber = 0;
          double wt,*dRda, Freedom, Sig2;
          double *RelCal, Diff=0.0;
          dRda = dvector(1,ParameterNumber);
          RelCal = dvector(1,DataPointFit);

          for (j=1; j<=ParameterNumber; j++)          /* Fix or Change the Parameter Values */
          if (FixorFitP[j])  ParameterFitNumber++;   /* The Final Fitting Parameter Numbers */
          for (j=1;j<=ParameterFitNumber;j++)
          {
                    for (k=1;k<=j;k++) alpha[j][k]=0.0;
                    beta[j]=0.0;
          }
          Freedom=1.0/double (DataPointFit-ParameterFitNumber);   /* the fitting parameter
                                                                                    freedom*/
          *chisq=0.0;                                 /* The Pointer to the Least Square Value */
          for (i=1;i<=DataPointFit;i++)         /* Calculated the Summation of all Fitting Data  */
          {
                    /* Calcuate the chisq and error is 1,  the final change  the  error! */
                    *(RelCal+i-1) = spectra (*(wavenumbers+i-1), Parameter, OscillatorNumber,
                                        ModelSelection);
                    Diff=((*(Expdata+i-1))-(*(RelCal+i-1)))/(*sig);
                    Sig2=1.0/(pow((*sig),2));

                    for (j=0,l=1;l<=ParameterNumber;l++)
                    {
                              /*calculate the first Derivative for  the fitting parameter */
                              if (FixorFitP[l])
                                        {
                                                  dRda[l]=Derivative(*(wavenumbers+i-1),l,Parameter,
                                                            OscillatorNumber, ModelSelection, spectra);
                                                  wt = dRda[l]*Sig2;
```

```
for (j++,k=0,m=1;m<=l;m++)
                                {
                                        if (FixorFitP[m]) alpha[j][++k]+=wt*dRda[m];
                                }
                                        beta[j]+=Diff*wt;
                                }
                }
                *chisq+=Diff*Diff*Freedom;          /* return the Least Square Value*/

        }

        for (j=2;j<=ParameterFitNumber;j++)
        for (k=1;k<j;k++) alpha[k][j]=alpha[j][k];
        free_dvector(RelCal,1,DataPointFit);
        free_dvector(dRda,1,ParameterNumber);
}




/* Levenberg_Marquardt fitting method */

void Levenberg_Marquardt (double wavenumbers[], int DataPointFit, double *Expdata,
                          double Parameter[], double ParameterMin[], int ParameterNumber, int
                         FixorFitP[], double **covar, double **alpha,double *alamda,
                         double *chisq, double *sig,int *OscillatorNumber, int *ModelSelection,
                          double (*spectra)(double, double *,int *,int *))
{
        int j,k,l;
        static int ParameterFitNumber;
        static double ochisq,*atry,*da,*beta,**oneda, temp;

        if (*alamda <0.0)                       /*Initialize the program*/
        {
                atry=dvector(1,ParameterNumber);
                beta=dvector(1,ParameterNumber);
                da=dvector(1,ParameterNumber);
                for (ParameterFitNumber=0,j=1;j<=ParameterNumber;j++)
                {
                        if (FixorFitP[j]) ParameterFitNumber++;
                }
                oneda=matrix(1,ParameterFitNumber,1,1);
                *alamda=0.001;                  /*Give alamda a initial value 0.001*/
                Mrqcof (wavenumbers, DataPointFit, Expdata,FixorFitP, Parameter,
                        ParameterNumber, alpha, beta, chisq, sig, OscillatorNumber,
                        ModelSelection,spectra);
```

```
                ochisq=(*chisq);                    /* the initial least square value is saved */
                for (j=1;j<=ParameterNumber;j++) atry[j]=Parameter[j];  /*Parameter
                                                                        Initialization */
        }

        for (j=1;j<=ParameterFitNumber;j++)     /* Calculate the fitting Parameter values*/
        {
                for (k=1;k<=ParameterFitNumber;k++) covar[j][k]=alpha[j][k];
                covar[j][j]=alpha[j][j]*(1.0+(*alamda));
                oneda[j][1]=beta[j];
        }

        if (*alamda!=0.0)                       /* Fitting calculation*/
        {
                Gauss_Jordan_Matrix(covar, ParameterFitNumber, oneda,1);  /*Matrix Solution*/
                for (j=1;j<=ParameterFitNumber;j++) da[j]=oneda[j][1];    /* save the solution
                                                                        results */
        }

        if (*alamda==0.0)       /* Once converged or calculation stopped, evaluate covariance
                                                                        matrix  */
        {
                Mrqcof (wavenumbers, DataPointFit, Expdata, FixorFitP, Parameter,
                        ParameterNumber, covar, da, chisq, sig, OscillatorNumber,
                        ModelSelection, spectra);

                Gauss_Jordan_Matrix (covar, ParameterFitNumber, oneda, 1);   /* calculate
                                                                        [C]=[a]-1*/
                covsrt(covar, ParameterNumber, FixorFitP, ParameterFitNumber);
                covsrt(alpha, ParameterNumber, FixorFitP, ParameterFitNumber);
                free_matrix(oneda,1,ParameterFitNumber,1,1);
                free_dvector(da,1,ParameterNumber);
                free_dvector(beta,1,ParameterNumber);
                free_dvector(atry,1,ParameterNumber);
return;
}

for (l=1;l<=ParameterNumber;l++)
{
        cout<<ParameterMin[l]<<" "<<Parameter[l]<<endl;
}


        /* the next step */
        for (j=0,l=1;l<=ParameterNumber;l++)
                if (FixorFitP[l])
                {
                        temp=atry[l];
```

```
                        atry[l]=Parameter[l]+da[++j];
                        if (atry[l] > (Parameter[l]+ParameterMin[l]))
                        {
                                cout<<atry[l]<<" "<<ParameterMin[l]<<endl;
                                //atry[l] = Parameter[l]+ParameterMin[l];
                                atry[l] =temp;
                        }

                        if (atry[l] < (Parameter[l]-ParameterMin[l]))
                        {
                                cout<<atry[l]<<" "<<ParameterMin[l]<<endl;
                                //atry[l] = Parameter[l]-ParameterMin[l];
                                atry[l] =temp;
                        }
                }
        Mrqcof (wavenumbers, DataPointFit, Expdata, FixorFitP,atry, ParameterNumber, covar,
                da,chisq, sig, OscillatorNumber, ModelSelection,spectra);

        /* calculate the Least square velue of (P+dataP) */
        if (*chisq<ochisq)    /* the chisq is decreased, update the fitting parameter */
        {
                *alamda*=0.1;
                ochisq=(*chisq);
                for (j=1;j<=ParameterFitNumber;j++)
                {
                        for (k=1;k<=ParameterFitNumber;k++) alpha[j][k]=covar[j][k];
                        beta[j]=da[j];
                }
                for (l=1;l<=ParameterNumber;l++) Parameter[l]=atry[l];
        }
        else                            /*increase alamda*/
        {
                *alamda*=10.0;
                *chisq=ochisq;
        }
}
```

```
/* Levenberg_Marquardt iteration calculation*/
void Levenberg_Marquardt_Fitting (double wavenumbers[], int DataPointFit, double *Expdata,
                                  int *Iteration,char *DisplayIteration, double Parameter[], double
                                  ParameterMin[], int ParameterNumber, int FixorFitP[],double
                                  **covar, double **alpha, double *alamda,double *chisq,double
                                  *sig, int *OscillatorNumber, int *ModelSelection,  double
                                  *(spectra) (double, double *,int *,int *))
{
        int k=1,IterationStop=0;
        double ochisq;
        bool Stop=true;

       Levenberg_Marquardt (wavenumbers, DataPointFit, Expdata, Parameter, ParameterMin,
                            ParameterNumber, FixorFitP, covar, alpha, alamda, chisq, sig,
                            OscillatorNumber, ModelSelection, spectra);


        /*judge the calculation continue*/
        cout<<"The initial Chi-Square Value: ";
        cout<<(*chisq)<<endl;

        do                      /* the main calculation loop*/
        {
                ochisq=(*chisq);
                Levenberg_Marquardt (wavenumbers, DataPointFit, Expdata,Parameter,
                                     ParameterMin, ParameterNumber, FixorFitP, covar,
                                     alpha, alamda, chisq, sig, OscillatorNumber,
                                     ModelSelection, spectra);

                if (((*DisplayIteration)=='y')||((*DisplayIteration)=='Y'))
                {
                        cout<<"\n"<<endl;
                        cout<<"! the "<<k<<"th iteration: "<<endl;
                        cout<<"Chi-Square Value: ";
                        cout<<*chisq<<endl;
                }
                        if (fabs((*chisq)-ochisq)<=1e-8) IterationStop++;
                        else   IterationStop=0;
                        if ((IterationStop==5)||(k==(*Iteration)))
                {
                        Stop=false;
                        (*Iteration)=k;
                }
                k++;

        } while (Stop);             /* the main loop is over*/
```

```
        ochisq=(*chisq);            /* save the best chisq value */
        *sig=pow((*chisq),0.5);     /* calculate the parameter standard error*/
        *alamda=0.0;
        Levenberg_Marquardt (wavenumbers,  DataPointFit, Expdata,Parameter, ParameterMin,
                             ParameterNumber, FixorFitP, covar, alpha, alamda, chisq, sig,
                             OscillatorNumber, ModelSelection, spectra);
                             *sig=(*chisq);             /* return the chi-square value (should be 1) */
                             (*chisq)=ochisq;           /* return the best chisq value */
}
```

Appendix B

Photoluminescence (PL) Setup

Photoluminescence (PL) is a contactless and non-destructive material characterization method. PL can be used to probe various electronic properties of semiconductor materials systems. Fundamental band gaps, impurities and defects, band offsets in heterostructures, and inter and intra sub band energy levels in quantum well structures can be studied using PL. In PL, carriers are exited to higher energy levels by a high energy light beam (usually a laser light source). Photoexited carriers will re-combine with holes, impurities, or defects by releasing energy in the form of light which is equal to the energy difference between the two energy levels involved in the re-combination process. By analyzing the emitted light spectrum, important characteristics of material's electronic properties can be studied. In general, laser light is used as the exitation light source. Figure B.1 shows the schematic diagram of the PL setup used in the Opto electronic lab. Ar-Lalser is used as the light source and Perkin-Elmer System 2000 FTIR is used as the spectrometer. The light emitted by the sample is collected by the off-axis concave mirror and directed into the spectrometer light path as shown in Fig. B.1. In this case, emitted light by the sample

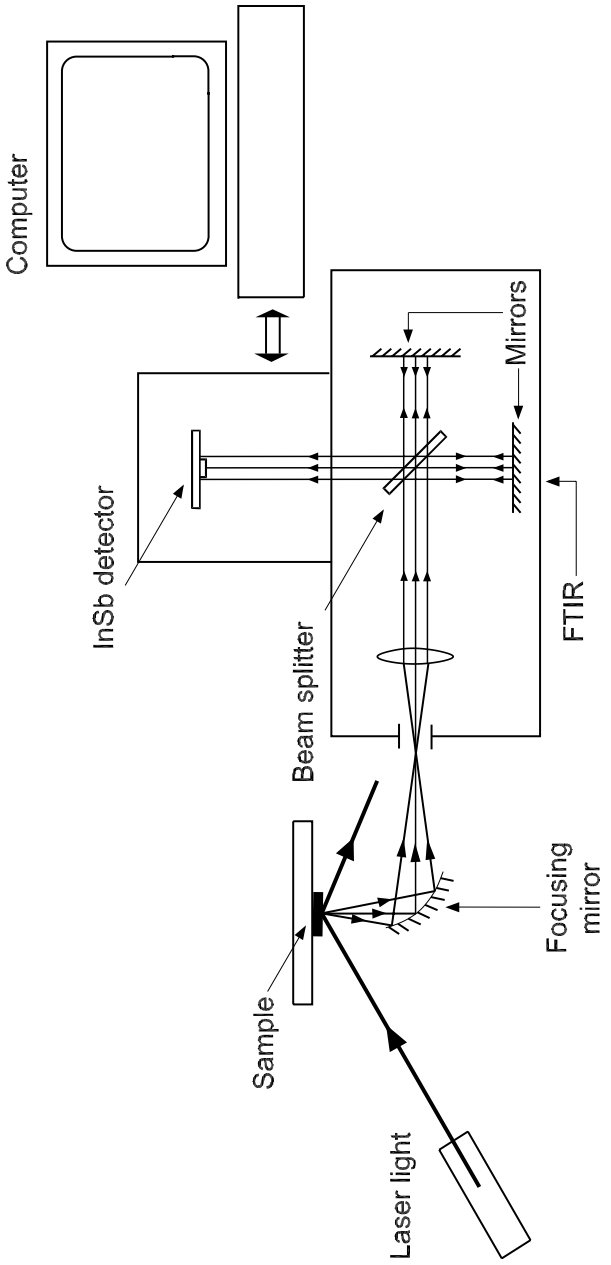

Figure B.1: Schematic diagram of the photoluminescence setup with the FTIR

acts as an external source for the spectrometer. InSb IR photo detector (0.8 - 4 μm) is used as the detector. As a case study, photoluminescence spectrum obtained at 77 K for n-GaAs/$A_{0.04}Ga_{0.96}As$ heterostructure is shown in Fig B.2. Here n is 1×10^{18} cm^{-3}. Wavelength of the exitation laser is 488 nm. The broad peak is due to the n-GaAs layer and the narrow peak is due to the $A_{0.04}Ga_{0.96}As$ layer. In general, transition energies (band gap in this case) can be estimated from peak positions. The n-type GaAs peak position is at 1.51 meV while $A_{0.04}Ga_{0.96}As$ peak position is at 1.55 meV. The advantage of using an FTIR instead of a monochromator as the spectrometer, is the speed. Since FTIR can perform averaging over a couple of hundred spectra, this method is better for noisy background situations.

Before the using the system, a fine focusing should be achieved. For this purpose, the following procedure is advised.

- perform the aligning procedure with the FTIR internal light source and the InSb detector according to the instruction given in the FTIR software.
- switch the FTIR light source to the external source (read the FTIR manual for more information)
- place the off-axis concave mirror about 5 cm from the the FTIR external source window as shown in Fig. B.1.
- place the sample holder about 3 - 5 cm away from the concave mirror as shown in Fig. B.1.
- place a piece of white paper (1 cm$\times$1 cm) at the place where the sample is going to

be placed. The piece of paper should face the concave mirror.

- bring a white light source and aim it at the white paper. Disperse light off the paper will be directed into the FTIR by the concave mirror.
- align the concave mirror and sample holder position (white paper) so that the spectrum of the disperse light is maximum.
- once the disperse light spectrum is manually aligned to the optimum level, perform the aligning procedure of the FTIR. (Now your light source is the disperse light from the paper)
- replace the white paper with your sample and remove the white light source.
- aim the laser light to the sample at an angle and the system is ready for PL experiment.

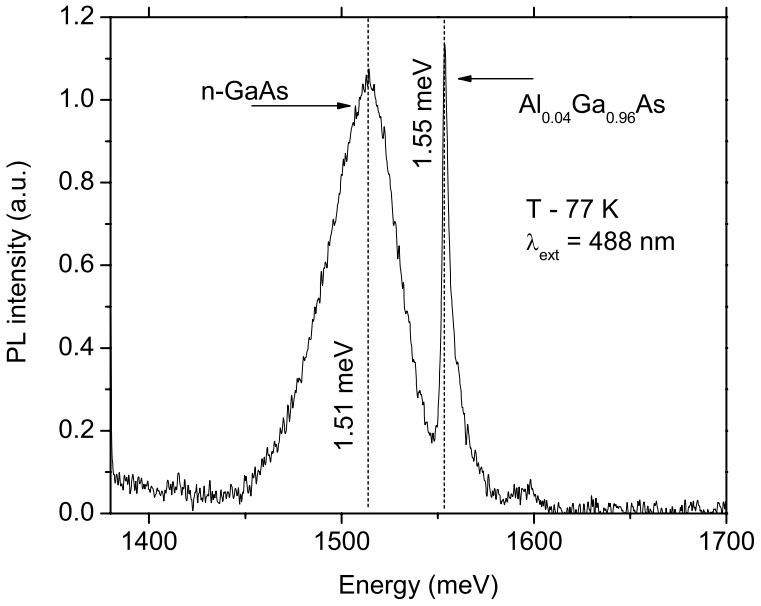

Figure B.2: The PL spectrum of n-GaAs/$A_{0.04}Ga_{0.96}As$ heterostructure at 77 K. The wavelength of exitation light (Argon Laser) is 488 nm. Both peaks corresponding to n-GaAs and undoped $A_{0.04}Ga_{0.96}As$ layers are visible at 1.51 meV and 1.55 meV.

Appendix C

Terahertz Effect on DRG Explants in Chick Model

Under this study, the effects of teraherz radiation on the growth of nervous system was investigated by using dorsal root ganglion (DRG) explants as an in vitro model system in collaboration with Dr. V. Rehder in the Department Biology and Dr. N. Dietz in the Department of Physics at Georgia State University. The sample preparations and irradiation were carried out by Amanda L. Jacob. and the following context was taken from the report prepared by Amanda L. Jacob.

(a) DRG Explant Cultures

DRG explants were taken from chicken embryos and were pasted in a plastic multi-well plate with a laminin concentration of 10 μg/cm^2 and kept in a CO_2 incubator. After a minimum of two hour period, a nerve growth factor (NGF) of 1 g/mL concentration was added to each DRG explant. The explants were placed in a minimum essential medium (MEM) after removal from the CO_2 incubator. During the experiments, the temperature

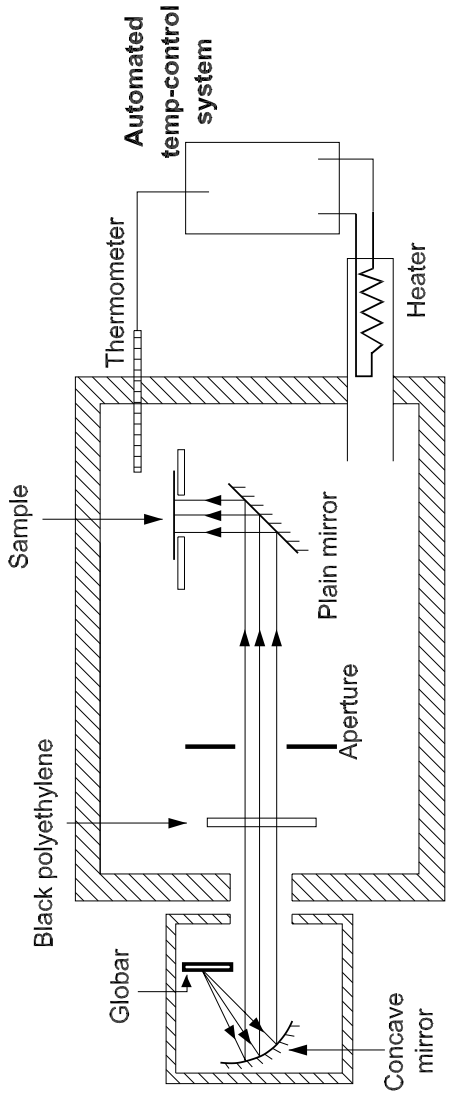

Figure C.1: The schematic diagram of the complete arrangement for DRG irradiation setup. The terahertz radiation was filtered from the globar by using black polyethylene and the plastic multi-well plate and is shown in Fig. C.2. Mirrors and the aperture were used for focusing. Styrofoam compartment along with an automated temperature control system provides a good thermal stability.

was kept at 37.0 ± 2.0 ^{0}C, and a CO_2 incubator and/or pH maintaining medium was used to control the pH. Irradiation of DRGs with terahertz radiation was carried out inside a temperature-controlled system and a schematic diagram of the setup is shown in Fig. C.1. The compartment built of styrofoam was used to achieve a better thermal stability since the temperature of DRG explants should be maintained between 37.0 ± 2.0 C during the radiation experiments. An automatic temperature controller along with a heater was used to control the temperature inside the Styrofoam compartment. The globar which was used as the radiation source, was placed adjacent to the Styrofoam compartment, and the radiation beam was guided into the compartment and to the DRG explants using optical mirrors as shown in Fig. C.1. The heating effects on DRGs due to the IR radiation were avoided by using a black polyethylene filter. The Black polyethylene plus the plastic sample holder filtered out high frequency radiation (> 15 THz or IR radiation) and the radiation spectrum used for the irradiation is shown in Fig. C.2 which was taken with a Si-composite bolometer.

Pictures of the explants were recorded using a microscope at a magnification of 20× under both baseline conditions and radiation treatment. Adobe PhotoShop 7 was used to record the area covered by the DRG explants.

The DRG explant irradiation was carried out inside the setup described above (see Fig. C.1). A group of DRGs (irradiated) was illuminated and another group of DRGs (control) was also kept in the compartment but was not illuminated with terahertz radiation. Temperature of both the control and irradiated DRG explants were monitored through out the experiment to ensure that the inside temperature was stable. The temperature was found to be consistent between 36.5 - 35.5 ^{0}C. This procedure ensured that the control

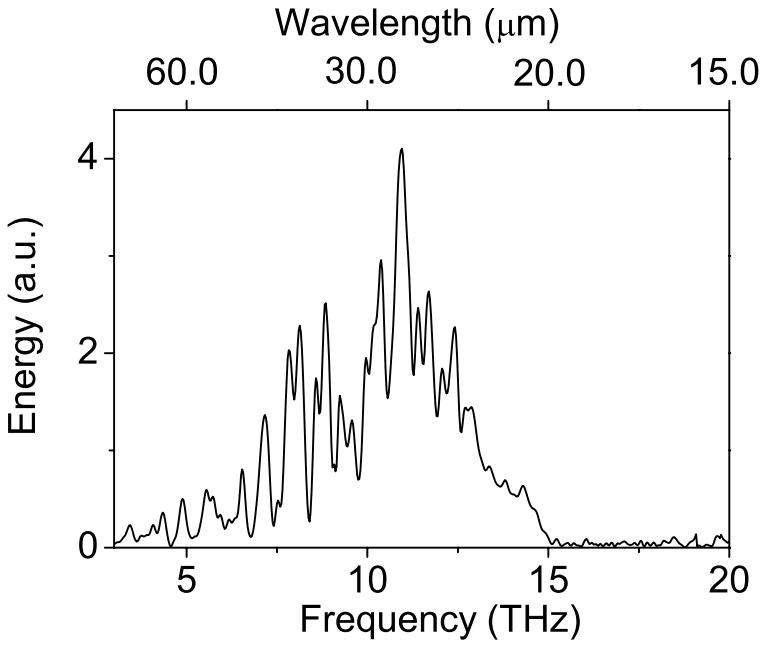

Figure C.2: The radiation spectrum of the globar used to irradiate DRGs. The spectrum was taken with Si-composite bolometer with the all optics used in the experiment included. The the maximum power that reached the sample compartment is 4 - 5 μW. High frequency (short wavelength) light (15 THz) was filtered out using a black polyethylene filter plus the plastic sample holder.

and irradiated samples were under the same conditions except the terahertz radiation. The length of radiation exposure time was varied during the DRG's neurite development.

(b) Analysis

In the first attempt, after the introduction of NGF on the DRGs, DRGs were allowed to grow without radiation for 16 to 18 hours, after that, DRGs were irradiated for 6 hours. During the irradiation process, the growth was monitored and recorded. The percentage of area changes over the six hour period are shown in Fig C.3 (a) for both irradiated and the control samples. According to the results, no considerable growth rate difference was observed between two samples. The number of irradiated samples is 17 while the number of control samples is 19.

To study the effects of the terahertz radiation on neurite initiation, the DRGs were irradiated with terahertz radiation for 16 to 18 hours soon after the NGF was added on to the DRGs. After that, the growth rate of both irradiated and the control samples were monitored for six hours and the percentage of area change is shown in Fig. C.3 (b). The growth rates between the irradiated group and its control were not significantly different. The surface area change in DRGs between irradiated and control is within the statistical error. Twenty one irradiated samples and twenty control samples were used in the experiment.

To test the possible long term effects, two different irradiation experiments were carried out. In the first experiment, before initial exposure to the radiation was begun, a 17 hour initiation period occurred after the introduction of NGF, and DRGs were continuously irradiated with terahertz radiation for a total of 28 hours. This study also did not result in a difference in the DRG growth rate of the explants and results are shown in Fig. C.4 (a).

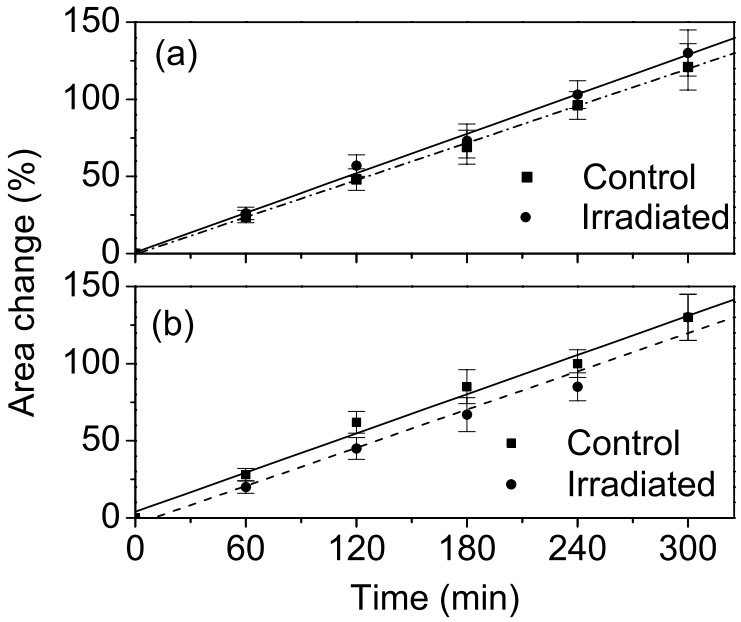

Figure C.3: (a) Area change of DRGs for both the irradiated samples and the control samples. Irradiation started after an initial growth of 16 - 18 hour period without radiation. N (irradiated) = 17 and N (control) = 19. (b) Irradiation started right after the introduction of NGF on the DRGs for 16 -18 hours. Growth rates were monitored after the initial irradiation. Area change in both samples are within the error. N (irradiated) = 21 and N (control) = 20.[data from Amanda L. Jacob from Dr. V. Rehder's lab, Dept of Biology,GSU]

Six irradiated and Six control samples were used in this part of the experiment.

The second experiment was carried out as follows. The DRG explants were exposed to the terahertz radiation soon after the introduction of NGF and the explant area was monitored for 2 days with a total of 40 hours of irradiation period. It was found to be no statistical change in the area change during over the 2 days as seen in Fig. C.4 (b). Six irradiated samples and five control samples were used under this experiment. According to the study, the exposure to the terahertz radiation seems to have no long term effect on neurite outgrowth and initiation.

This study has provided evidence that terahertz radiation has no effect on the neuronal outgrowth in the chick model system within the studied terahertz radiation range (15 - 5 THz) under total energy of 4 - 5 μW. It gives evidence that effects of terahertz radiation on DRG outgrowth can be negligible under a few micro watts of terahertz exposure.

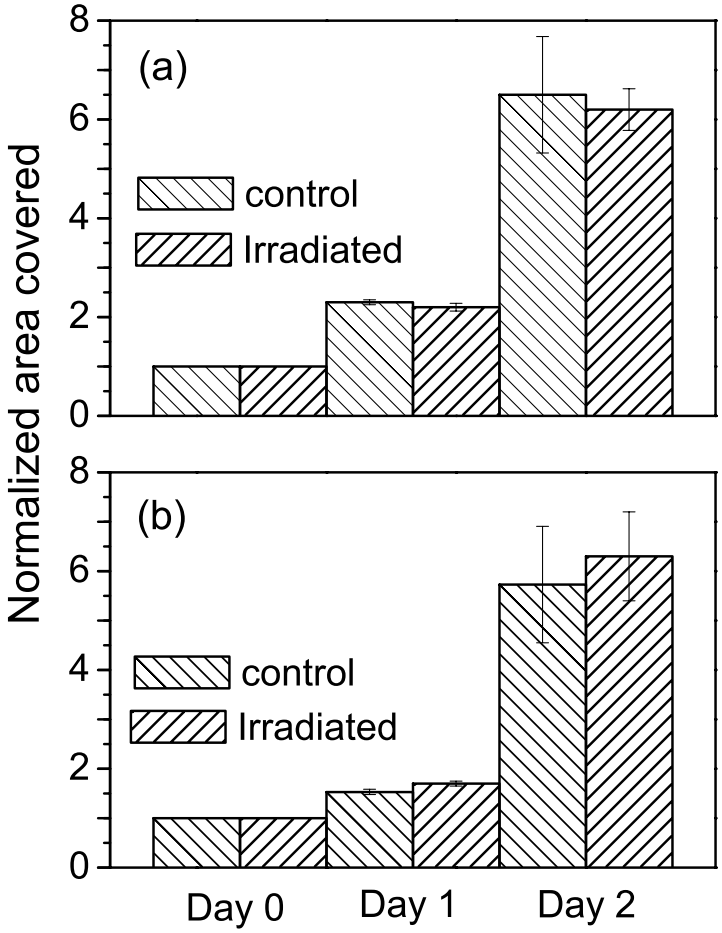

Figure C.4: The normalized area for the irradiated and control samples. The first measurement was taken on Day - 0 before irradiation. Then two measurements were taken in the following two days. (a) Area recorded during a 28 hours irradiation period preceded by a 17 hour growth initiation without radiation. N (irradiated) = 6 and N (control) = 6. (b) Irradiation started right after the introduction of NGF on the DRGs. The measurements were carried out over two days (40 hours). N (irradiated) = 6 and N (control) = 5. [data from Amanda L. Jacob from Dr. V. Rehder's lab, Dept of Biology,GSU]

Appendix D

Amplitude Adjusted Fourier Transform Algorithm

Surrogate data generated by Amplitude Adjusted Fourier Transform (AAFT) Algorithm [107] can be used to test the validity of the calculated correlation dimension. In some cases, the original data can produce a spurious correlation dimension. This spurious correlation dimension can be due to the nature of the original data. Therefore, the calculated correlation dimension must be tested against a surrogate data set generated from the original time series, but it does not carry any deterministic properties. The following procedure describes the AAFT algorithm to generate a surrogate data set. Surrogate data generated by AAFT has same variance and mean as the original data but it doest posses any deterministic properties.

AFFT Algorithm

1. denote the original time series, x[t], t = 0, 1,....., N-1

2. Generate a time series by using a Gaussian pseudorandom number generator, y[t], t=0, 1,....., N-1

3. Reorder the generated time series, y[t] so that the nth smallest one of y[t] series is at the same position as the nth smallest of the x[t] series.

4. Take the Fourier transform (FT) of the reordered time series.

5. Randomize phase of FT output; multiply the output of the FT (complex amplitudes) by $e^{i\phi}$, where ϕ is randomly selected phase in [0 - 2π].

6. Take the inverse FT of the time series after phase randomization.

Appendix E

Correlation Dimension Calculation

```
/* calculates the correlation dimension ,  Scaling region and the embedding dimension loop are
inside the main loop. Output file consist of scaling region, embedding dimension, and correlation
integral */

#include<iostream.h>
#include<stdlib.h>
#include<iomanip.h>
#include<string.h>
#include <dos.h>
#include<fstream.h>
#include <math.h>
#include <conio.h>
#include <stdio.h>
double  dist, R, c, IR, FR, SR, dd, frac;
double  x[450000], y, *v1, *v2, xx;
int i, d, N, j, k, l, p, count, h, fd, sd, incd, temp, size, ii, g, t, kk, Fk, yy, Rsize,ssd;
double  dist1, dist2, cnt[40][40];
char sampleID[30], FileName[30];

ifstream fp;
ofstream fo;
```

```
void main()
{

        fp.open("ExpData.dat",ios::in);
        printf("improved one \n");
        printf("enter the number of data, N=");
        cin>>N;
        printf("enter the starting dimension= ");
        cin>>sd;
        printf("enter the final dimension=");
        cin>>fd;
        printf("enter the increment dimension=");
        cin>>incd;
        printf("enter the starting R =");
        cin>>SR;
        printf("enter the final  FR =");
        cin>>FR;
        printf("enter the Increment R =");
        cin>>IR;
        R=SR; /* scaling region */
        ///* initialize the array */
        printf("Enter the out put name \n");
        cin>>sampleID;

        for (i=0;i<=N+d-1;i++)   x[i]=0;

/* reads the input file  into the array*/
        for( i=0;i<=N+fd-1;i++)
        {
                fp>>xx>>y;
                x[i]=xx;
        }
        printf("%d,%f",i,xx);

        temp=1;
        fp.close();
        Rsize=0;

        for (R=SR;R<=FR;)  /*initialize the scaling region/*
        {
                Rsize++;
                R=R+IR;
        }
        printf("R=%d \n",Rsize);
        sprintf(FileName,"%s%d.dat",sampleID,temp);
        printf(" filename= %s \n",FileName);
        h=0; /* index for the vector*/
        printf("SR=%f,FR=%f\n",SR,FR);
```

```
for (g=0;g<=40;g++)
{
        for (t=0;t<=size;t++)
        {
                cnt[g][t]=0;
        }
}

v1 = (double *) malloc((fd)*sizeof(double));
if ((v1== NULL))
{
        printf("Not enough memory to allocate buffer\n");
        exit(1);
}
for (i=0;i<=fd-1;i++)
{
  v1[i]=0;/* the first vector*/
}
v2 = (double *) malloc((fd)*sizeof(double));
if ((v2== NULL))
{
        printf("Not enough memory to allocate buffer\n");
        exit(1);
}
for (i=0;i<=fd-1;i++)
{
        v2[i]=0; /* the second vector*/
}
//printf("SR=%f,FR=%f\n",SR,FR);
count=0;
for(i=0;i<=N-1;i++)
{
        k=0;
        /* reads the numbers in to the first vector*/
        for (j=i;j<=i+fd-1;j++)
        {
                v1[k]=x[k+i];
                k++;
        }
        j=0;
        l=i;
        k=0;

/*reads the numbers in to the second vector */
        for (j=l;j<=l+fd-1;j++)
        {
                v2[k]=x[j];
                k++;
```

```
        }
        do
        {
                dist=0;
                dist1=0;
                ssd=sd;
                if(l!=i)
                {
                        p=0;
                        kk=0;
                        for (p=0;p<=fd-1;p++)
                        {
                                kk++;
                                dist1=dist1+(v1[p]-v2[p])*(v1[p]-v2[p]);
                                if(ssd==kk)
                                {
                                        R=SR;
                                        ii=0;
                                        for (R=SR;R<=FR;)
                                        {
                                                ii++;
                                                if((R*R>dist1)&&(l!=i))
                                                {
                                                        cnt[kk][ii]=cnt[kk][ii]+2;
                                                }
                                                R=R+IR;
                                        }
                                        ssd=ssd+incd;
                                }
                        }
                }
                l=l+1;
                v2[0]=v2[1];
                h=1;
                do
                {
                        v2[h]=v2[h+1];
                        h=h+1;
                }
                while(h<=fd-2);
                v2[fd-1]=x[l+fd-1];

        }
        while(l<N);
}
Fk=kk;
```

```
        for (kk=sd;kk<=fd;)
        {
                R=SR;
                sprintf(FileName,"%s%d.dat",sampleID,temp);
                fo.open(FileName,ios::trunc);
                fo<<FileName<<"\n";
                fo<<"Number of data="<<N<<"\n";
                fo<<"R"<<"      "<<"Dimn"<<"  "<<"C(R)"<<"\n";
                for (ii=1;ii<=Rsize;)
                {
                        c=cnt[kk][ii]/(N*(N-1.0));
                        printf("R=%f,C(%d)=%20.18f\n",R,kk,c);
                        fo<<R<<" "<<kk<<" "<<c <<" "<<cnt[kk][ii]<<"\n";
                        R=R+IR;
                        ii++;
                }
                fo.close();
                printf("\n");
                kk=kk+incd;
                temp=temp+1;
        }

free(v1);
free(v2);
printf("finished!!!");
}
```

Bibliography

[1] K. Miwa and A. Fukumoto, Phys. Rev. B **48**, 7897 (1993).

[2] Hiroshi Harima, J. Phys.: Condens. Matter **14**, R967 (2002).

[3] M. H. Kane, A. Asghar, C. R. Vestal, M. Strassburg, J. Senawiratne, Z. J. Zhang, N. Dietz, C. J. Summers, and I. T. Ferguson, Semicond.Sci. Technol. **20**, L5 (2005).

[4] A. Rogalski, Infrared Phys. **43**, 187 (2002).

[5] M. B. M. Rinzan, A. G. U. Perera, S. G. Matsik, H. C. Liu, Z. R. Wasilewski, and M. Buchanan, Appl. Phys. Lett. **86**, 071112 (2005).

[6] S. A. Wolf, D. D. Awschalom, R. A. Buhrman, J. M. Daughton, S. von Molnar, M. L. Roukes, A. Y. Chtchelkanova, and D. M. Treger, Science **294**, 1488 (2001).

[7] P. H. Siegel, IEEE Trans on Microwave Theory and Techniques **50**, 910-928 (2002).

[8] E. Pickwell, B. E. Cole, A. J. Fitzgerald, M. Pepper, and V. P. Wallace, Phys. Med. Bio. **49**, 1595 (2004).

[9] S. W. Smye, J. M. Chamberlain, A. J. Fitzgerald, and E. Berry, Phys. Med. Bio. **46**, R101 (2001).

[10] John F. Federici, Brian Schulkin, Feng Huang, Dale Gary, Robert Barat, Filip Oliveira, and David Zimdars, Semicon. Sci. Technol. **20**, s266 (2005).

[11] A. G. U. Perera, S. G. Matsik, B. Yaldiz, H. C. Liu, A. Shen, M. Gao, Z. R. Wasilewski, and M. Buchanan, Appl. Phys. Lett **78**, 2241 (2001).

[12] S. G. Matsik, M. B. M. Rinzan, A. G. U. Perera, H. C. Liu, Z. R. Wasilewski, and M. Buchanan, Appl. Phys. Lett. **82**, 139 (2003).

[13] S. G. Matsik, M. B. M. Rinzan, D. G. Esaev, A. G. U. Perera, G. von Winckel, A. Stintz, S. Krishna, H. C. Liu, M. D. Byloos, T. Oogarah, G. I. Sproule, K. Liu, and M. Buchanan, IEEE Trans. Elec. Dev. **52**, 413 (2005).

[14] D. G. Esaev, M. B. M. Rinzan, S. G. Matsik, and A. G. U. Perera, J. Appl. Phys. **96**, 4588 (2004).

[15] M. Mahowald and R. J. Douglas, Nature **354**, 515 (1991).

[16] D. D. Coon and A. G. U. Perera, in *Visual Communications and Image Processing'90 - SPIE Volume 1360* (1990).

[17] D. D. Coon and A. G. U. Perera, Int. J. IR and Millimeter Waves **8**, 1037 (1987).

[18] A. G. U. Perera, S. G. Matsik and S. R. Betarbet, in *Visual Information Processing IV - SPIE Volume 2448* (1995).

[19] D. D. Coon and A. G. U. Perera, Int. J. Electronics **63**, 61 (1987).

[20] Mark Fox, *Optical Properties of Solids* in (Oxford University Press, Oxford, NY, 2001).

[21] C. Kittel, *Introduction to Solid State Physics* in (John Wiley and Sons, New York, 1976).

[22] Sidney Perkowitz, *Optical Characterization of Semiconductors: Infrared, Raman, and Photoluminescence Spectroscopy* in (Academic Press, NY, 1993).

[23] M. V. Klein, T. E. Furtac, *Optics* in (Wiley, New York, 1986).

[24] C. C. Katsidis and D. I. Siapkas, Appl. Optics **41**, 3978 (2002).

[25] W. H. Press, S. A. Teukolsky, W. T. Vetterling, and B. P. Flannery, *Numerical Recipes in C: The Art of Scientific Computing* in (Cambridge University Press, Cambrdge, MA, 1992).

[26] S. J. Pearton, C. R. Abernathy, D. P. Norton, A. F. Hebard, Y. D. Park, L. A. Boatner, J. D. Budai, Materials Science and Engineering **R 40**, 137 (2003).

[27] T. Dietl, H. Ohno, F. Matsukura, J. Cibert, and D. Ferrand, Science **287**, 1019 (2000).

[28] W. Limmer, M. Glunk, S. Mascheck, A. Koeder, D. Klarer, W. Schoch, K. Thonke, R. Sauer, and A. Waag, Phys. Rev. B **66**, 205209 (2002).

[29] Z. S. Popovic, S. Satpathy, and W. C. Mitchel, Phys. Rev. B **70**, 161308 (2004).

[30] G. Thaler, R. Frazier, B. Gila, J. Stapleton, M. Davidson, C. R. Abernathy, and C. Segre, Appl. Phys. Lett. **84**, 1314 (2004).

[31] O. Gelhausen, E. Malguth, and M. R. Phillips, E. M. Goldys, M. Strassburg, A. Hoffmann, T. Graf, M. Gjukic, and M. Stutzmann, Appl. Phys. Lett. **84**, 4514 (2004).

[32] B. Han, R. Y. Korotkov, B. W. Wessels, and M. P. Ulmer, Appl. Phys. Lett **84**, 5320 (2004).

[33] C. Wetzel, E. E. Haller, H. Amano, and I. Akasaki, Appl. Phys. Lett **68**, 2547 (1996).

[34] M. Holtz, T. Prokofyeva, M. Seon, K. Copeland, J. Vanbuskirk, S. Williams, S. A. Nikishin, V. Tretyakov, and H. Temkin, J. Appl. Phys. **89**, 7977 (2001).

[35] W. Fenwick, A. Asghar, S. Gupta, H. Kang, M. Strassburg, N. Dietz,S. Graham, M. H. Kane, and I. T. Ferguson, Vac. Sci. Technol. A **24**, 1640 (2006).

[36] A. Kasic, M. Schubert, S. Einfeldt, and D. Hommel, Phys. Rev. B **62**, 7365 (2000).

[37] M. Schubert, T. E. Tiwald, and C. M. Herzinger, Phys. Rev. B **61**, 8187 (2000).

[38] R. Aguado, M. P. López-Sancho, J. Sinova, and L. Brey, Phys. Rev. B **70**, 195201 (2004).

[39] W. Gebicki, J. Strzeszewski, G. Kamler, T. Szyszko, and S. Podsiadło, Appl. Phys. Lett. **76**, 3870 (2000).

[40] D. Brunner, H. Angerer, E. Bustarret, F. Freudenberg, R. Dimitrov, O. Ambacher, and M. Stutzmann, J. Appl. Phys. **82**, 5090 (1997).

[41] T. Kozawa, T. Kachi, H. Kano, Y. Taga, M. Hashimoto, N. Koide, and K. Manabe, J. Appl. Phys. **75(2)**, 1098 (1994).

[42] Z. G. Hu, M. Strassburg, A. Weerasekara, N. Dietz, A. G. U. Perera, M. H. Kane, A. Asghar, and I. T. Ferguson, Appl. Phys. Lett. **88**, 061914 (2005).

[43] T. L. Tansley and C. P. Foley, J. Appl. Phys.Lett. **59**, 3241 (1986).

[44] Ashraful Ghani Bhuiyan, Kenichi Sugita, Ken Kasashima, Akihiro Hashimoto, Akio Yamamoto, and Valery Yu Davydov, Appl. Phys. Lett. **83**, 4788 (2003).

[45] J. Wu, W. Walukiewicz, K. M. Yu, J. W. Ager III, E. E. Haller, Hai Lu, and J. Schaff, Phys. Stat. Sol. (b) **240**, 412 (2003).

[46] Hai Lu, William J. Schaff, Geonghyun Hwang, Hong Wu, and Goutam Koley, App. Phys. Lett. **79**, 1489 (2001).

[47] Chad S. Gallinat, Gregor Koblmuller, Jay S. Brown, Sarah Bernardis, James S Speck, Grace D. Chern, Eric D. Readinger, Hongen shen, and Michael Wraback, App. Phys. Lett. **89**, 032109 (2006).

[48] T. Inushima, M. Higashiwaki, and T. Matsui, Phys. Rev. B **68**, 235204 (2003).

[49] M. C. Johnson, S. L. Konsek, A. Zettl, E. D. and Bourret-Courchesne, Appl. Phys. Lett. **81**, 1248 (2002).

[50] Takashi Matsuoka, Hiroshi Okamoto, Masashi Nakao, Hiroshi Harima, and Eiji Kurimoto, App. Phys. Lett. **81**, 1246 (2002).

[51] M. Alevli, G. Durkaya, W. Fenwick, A. Weerasekara, V. Woods, I. Ferguson, A.G.U. Perera and N. Dietz, Appl. Phys. Lett. **89**, 112119 (2006).

[52] N. Dietz, M. Alevli, V. Woods, M. Strassburg, H. Kang, and I. T. Ferguson, phys. stat. sol. (b). **242(15)**, 2985 (2005).

[53] V. Woods, H. Born, M. Strassburg and N. Dietz, J. Vac. Sci. Technol. A. **22(4)**, 1596 (2004).

[54] V. Woods and N. Dietz, Mater. Sci. & Eng. B **127(2-3)**, 239 (2006).

[55] V. A. Tyagai, A. M. Evstigneev, A. N. Krasiko, A. F. Andreeva, V. Ya Malakhov, Sov. Phys. Semicond. **11**, 1257 (1977).

[56] V. W. L. Chin, T. L. Tansley, T Osotchan, J. Appl. Phys. **75**, 7365 (1994).

[57] J. S. Thakur, G. W. Auner, D. B. Haddad, R. Naik, and V. M. Naik, J. Appl. Phys. **95**, 4795 (2004).

[58] T. Inushima, T. Shiraishi, V. Yu Davydov, Solid State Communications **110**, 491 (1990).

[59] T. L. Tansley, in properties of group iii nitrides, INSPEC (2005).

[60] Antoni Rogalski, Progress in Quantum Electronics **27**, 59-210 (2003).

[61] A. G. U. Perera, W. Z. Shen, S. G. Matsik, H. C. Liu, et. al., Appl. Phys. Lett. **72**, 1596 (1998).

[62] A. G. U. Perera, S. G. Matsik, H. C. Liu, et. al., Appl. Phys. Lett **77**, 741 (2000).

[63] H.C. Liu, C.Y. Song, A.J. Spring Thorpe, and J.C. Cao, Appl. Phys. Lett. **84**, 4068 (2004).

[64] A. G. U. Perera, S. G. Matsik, M. B. M. Rinzan, A. Weerasekara, M. Alevli, H. C. Liu, M. Buchanan, B. Zvonkov, and V. Gavrilenko, Infrared Phys. Technol. **44**, 347 (2003).

[65] D. G. Esaev, M. B. M. Rinzan, S. G. Matsik, A. G. U. Perera, H. C. Liu, B. N. Zhonkov, V. I. Gavrilenko, and A. A. Belyanin, J. Appl. Phys. **95**, 512 (2004).

[66] D. G. Esaev, S. G. Matsik, M. B. M. Rinzan, A. G. U. Perera, H. C. Liu, and M. Buchanan, J. Appl. Phys. **93**, 1879 (2003).

[67] J. M. Mooney and J. Silverman, IEEE Trans. Electron Devices **32**, 33 (1985).

[68] A. G. U. Perera, H. X. Yuan, and M. H. Francombe, J. Appl. Phys. **77**, 915 (1995).

[69] S. Nudelman, Applied Optics **1**, 627 (1962).

[70] M. Ershov and H. C. Liu, J. Appl. Phys. **86**, 6580 (1999).

[71] M. B. M. Rinzan, A. G. U. Perera, S. G. Matsik, H. C. Liu, M. Buchanan, G. von Winckel, A. Stintz, and S. Krishna, Infrared Phys. and Technol. **47**, 188 (2005).

[72] Huade Yao and A. Compaan, Appl. Phys.Lett **57**, 147 (1990).

[73] S. C. Jain and D. J. Roulston, Solid-St. Electron. **34**, 453 (1991).

[74] Federico Capasso, Alfred Y. Cho, Khalid Mohammed, and Philip W. Foy, Appl. Phys. Lett. **46**, 664 (1985).

[75] G. Ariyawansa, A. G. U. Perera, V. M. Apalkov, N. Dietz, and S. G. Matsik, in *March Meetings*, APS, (2007).

[76] G. Martin, A. Botchkarev, A. Rockett, and H. Morkoc, App. Phys. Lett. **68**, 2541 (1996).

[77] P. C. M. Planken, C. E. W. M. van Rijmenam, and R. N. Schouten, Semicond. Sci. Technol. **20**, S121 (2005).

[78] E. Starikov, P. Shiktorov, V. Gruzinskis, L. Reggiani, L. Varani, J. C. Vaissiere, and Jian H. Zhao, J. Appl. Phys. **89**, 1161 (2001).

[79] V. Gruzinskis, P. Shiktorov, E. Starikov, L. Reggiani, L. Varani, and J. C. Vaissiere, Semicond. Sci. Technol. **19**, S173 (2004).

[80] M.R. Scarf, M. Romano, R. Di pietro, O. zeni, A. doria, G. P. Gallerano, E. Giovenale, G. Messina, A. lai, G. Campurra, D. Coniglio, and M. Darienzo, J. Biol. Phys. **29**, 171 (2003).

[81] R. H. Clothier and N. Bourne, J. Biol. Phys. **29**, 179 (2003).

[82] D. D. Coon and A. G. U. Perera, Solid State Electronics **31**, 851 (1986).

[83] D. D. Coon and A. G. U. Perera, Neural Networks **2**, 143 (1989).

[84] D. D. Coon and S. D. Gunapala, J. Appl. Phys **57**, 5525-5528 (1985).

[85] T. K. Higman, L. M. Miller, M. E. Favaro, M. A. Emanuel, K. Hess, and J. J. Coleman, Appl. Phys. Lett. **53**, 1623 (1988).

[86] K. K Choi, B. F. Levine, R. J. Walker, and C. G. Bethea, Phys. Rev. B **35**, 4172 (1987).

[87] A. G. U. Perera, S. G. Matsik, V. Y. Letov, H. C. Liu, M. Gao, M. Buchanan, W. J. Schaff, Solid State Elec. **45**, 1121 (2001).

[88] E. Scholl, Phys. Rev. B **34**, 1395 (1986).

[89] J. B. Gunn, Solid State Comm. **1**, 88 (1963).

[90] E.Schöll, *Nonequilibrium Phase Transitions in Semiconductors* in (Springer-Verlag, Berlin, 1987).

[91] A. G. U. Perera and S. G. Matsik, Appl. Phys. Lett **67**, 962 (1995).

[92] Zh. I. Alferov, O. A. Mexrin, M. A. Sinitsyn, S. I. Troshkov and B. S. Yavich, Sov. Phys. Semicond. **21**, 304 (1987).

[93] A. Reklaitis, A. Krotkus, A. Geiztis, and M. Asche, Semicond.Sci.Technol. **14**, 341 (1998).

[94] D. D. Coon, S. N. Ma and A. G. U. Perera, Phys. Rev. Lett. **58**, 1139 (1987).

[95] A. B. Weerasekara, S. G. Matsik, G. S. Cymbalyuk, and A. G. U. Perera, Physica D **215**, 159-165 (2006).

[96] D. D. Coon and A. G. U. Perera, Appl. Phys. Lett. **51**, 1711 (1987).

[97] D. D. Coon and A. G. U. Perera, Solid-State Electronics **29**, 929 (1986).

[98] A. G. U. Perera and S. G. Matsik, Physica D **84**, 615 (1995).

[99] D. D. Coon and A. G. U. Perera, Appl. Phys. Lett. **51**, 1086 (1987).

[100] L. Esaki and L. L. Chang, Phys. Rev. Lett. **495-498**, 495-498 (1974).

[101] B. Williing and J. C. Maan, Phys. Rev. B. **49**, 13995 (1994).

[102] J. Kastrup, F. Prengel, H. T. Grahn, K. Ploog and E. Scholl, Phys. Rev. B. **53**, 1502 (1996).

[103] P. Grassberger and I. Procaccia, Phys. Rev. Lett. **50**, 346 (1983).

[104] Tim Sauer, Phys. Rev. Lett. **72**, 3811 (1994).

[105] M. Ding, C. Grebogi, E. Ott, T. Sauer, and J. A. Yorke, Phys. Rev. Lett. **70**, 3872 (1993).

[106] F. Takens, in *Lecture Notes in Mathematice Vol.898, Berlin, Germany* (1981).

[107] James Theiler, Stephen Eubank, Andre Longtin, Bryan Galdrikian, and J. Doyne Farmer, Physica. D **58**, 77 (1992).

[108] W. Braun, B. Eckhardt, H. A. Braun, M. Huber, Phys. Rev. E **62**, 6352-6360 (2000).

[109] F. Moss, L. Wilkens, X. Pei, K. Dolan, H. A. Braun, M. D. Lad, K. Schafer, and K. Voigt, in *Proceedings of the 4th Experimental Chaos Conference, 06-08 August, 1997, Florida, USA* (1997).

[110] D. D. Coon and A. G. U. Perera, Appl. Phys. Lett. **55**, 478 (1989).

[111] K. M. S. V. Bandara, D.D. Coon and R. P. G. Karunasiri, Appl. Phys. Lett. **51**, 961 (1987).

[112] J. H. Chae, J. Jeong, B. S. Peterson, D. J. Kim, W. M. Bahk, T. Y. Jun, S. Y. Kim, and K. S. Kim, Psychiatry Research: Neuroimaging **131**, 79 (2004).

[113] J. Lamberts, P. L. C. Van Den Broek, L. Berner, J. Van Egmond, R. Dirksen, and A. M. L. Coenen, Neuropsychobiology **41**, 149 (2000).

Acronyms

BLIP Background Limited Infrared Performance

D* Specific Detectivity

DMS Dilute Magnetic Semiconductor

FIR Far Infrared

HEIWIP Heterojunction Interfacial Workfunction Internal Photoemission

HIWIP Homojunction Interfacial Workfunction Internal Photoemission

IPTI Inter Pulse Time Intervals

IR infrared

MBE Molecular Beam Epitaxy

MCT Mercury Cadmium Telluride

MOCVD Metalorganic Chemical Vapor Deposition

MQW Multi Quantum Well

η_p Peak Quantum Efficiency

NEP Noise Equivalent Power

NNDR n-shaped negative differential resistance

PL Photoluminescence

QWIP Quantum Well Infrared photodetector

R_p Peak Photo Responsivity

SIMS Secondary Ion Mass Spectrometry.

SNDR s-shaped negative differential resistance

TGS Triglycine Sulfate

THz Terahertz

TTL Transistor Transistor Logic

UV Ultraviolet